

Master Thesis

**Spatially resolved excitation study  
of CO molecules in active galactic  
nuclei**

**Georgios-Filippos D. Paraschos**



School of Science, Physics Department  
National and Kapodistrian University of Athens  
Greece  
June 2019

Supervisors: Prof. K. Dasyra  
Prof. D. Hatzidimitriou

# Abstract

Jet activity and interactions with the ISM, like jet-cloud collisions, as well as energy deposition of the jet into the ambient ISM can be studied using spatially resolved observations of the CO excitation. In this thesis we aim to study this interaction between jets, originating from black holes, and the ambient, molecular gas and ISM. To do this we study three radio galaxies: OQ 208, 4C 12.50 and IC 5063, using observations from ALMA, SMA and the Plateau de Bure.

We create maps of the kinetic and excitation temperatures, number density, column density, pressure and optical depth by comparing the fluxes of each individual pixel to the theoretical fluxes calculated by the RADEX code.

Our first target, galaxy OQ 208, exhibits a temperature gradient of 10K between the nucleus and the rest of the gas. This result is typical for a spiral galaxy but not particularly indicative of jet activity.

Our second target is galaxy 4C 12.50 for which a CO wind has been observed. We aimed to translate the high excitation of the circumnuclear gas, that coincides with a wind location, into a temperature.

Our last target is galaxy IC 5063, a primary example for which analytical calculations have been carried out in a spatially resolved manner and have shown that the jet impacted regions reach a kinetic temperature of  $\sim 200$  K. We confirm this result, whether the gas is presumed to be in LTE or not.

Overall we find that jets can indeed impact the ambient ISM, causing the temperature to rise as high as a whole order of magnitude. This difference in temperature can have an impact in the detectability of winds but also in their mass content, as it can affect the  $\alpha_{\text{CO}}$  CO to H<sub>2</sub> conversion factor.

# Acknowledgement

I would like to thank my thesis advisor Prof. Kalliopi Dasyra for her guidance and help throughout my research. I would also like to thank Prof. Despina Hatzidimitriou for the comments provided.

# Contents

<b>1</b>	<b>Introduction</b>	<b>6</b>
1.1	Astrophysical Jets: Why are they important? . . . . .	6
1.2	Selection of radio galaxies . . . . .	8
1.2.1	OQ 208 . . . . .	8
1.2.2	4C 12.50 . . . . .	9
1.2.3	IC 5063 . . . . .	12
1.3	How to observe jets: Single dish vs. Interferometry . . . . .	13
1.4	Radio telescopes / Interferometers . . . . .	18
1.4.1	ALMA . . . . .	18
1.4.2	NOEMA . . . . .	19
1.4.3	SMA . . . . .	20
<b>2</b>	<b>Data</b>	<b>21</b>
2.1	Sub-mm interferometry for galaxy OQ 208 . . . . .	21
2.2	ALMA data of galaxy 4C 12.50 . . . . .	21
2.3	ALMA data of galaxy IC 5063 . . . . .	22
<b>3</b>	<b>Method of data processing</b>	<b>23</b>
3.1	Grid creation of physical parameters using RADEX . . . . .	23
3.2	Creation of collapsed images from 3D cubes . . . . .	25
3.3	Assumptions, boundary conditions and trials . . . . .	26
3.4	Parameter selection . . . . .	31
<b>4</b>	<b>Results</b>	<b>34</b>
4.1	OQ 208 . . . . .	34
4.1.1	Image creation / Code input . . . . .	34
4.1.2	Physical parameter maps . . . . .	34
4.2	4C 12.50 . . . . .	38
4.2.1	Image creation / Code input . . . . .	38
4.2.2	Physical parameter maps . . . . .	39
4.3	IC 5063 . . . . .	46
4.3.1	Image creation / Code input . . . . .	46
4.3.2	Physical parameter maps . . . . .	46
4.3.3	Residuals . . . . .	49
4.4	Combined excitation study using SLEDs . . . . .	55
<b>5</b>	<b>Discussion</b>	<b>57</b>

---

<b>6</b>	<b>Conclusions</b>	<b>61</b>
	<b>Bibliography</b>	<b>63</b>
<b>A</b>	<b>Python code</b>	<b>66</b>
A.1	Grid . . . . .	66
A.2	Maps . . . . .	69

# Chapter 1

## Introduction

### 1.1 Astrophysical Jets: Why are they important?

This work mainly focuses on AGN known to harbour jets. The reason we are interested in jets is that they deposit energy so quickly into the ISM -if they are relativistic- [Tetarenko et al., 2017] that the gas engulfed in its cocoon reaches instantly (and for most of the time) an adiabatic expansion mode. This means that jets are much more efficient in pushing gas than, for example, radiation pressure, which leads to adiabatic expansion for only part of the time.

But what are jets? Jets are collimated beams of plasma traveling usually at high velocities and dissipating their energy over large distances and thus disturbing the interstellar medium (ISM) and the intergalactic medium (IGM) [Fendt, 2006]. An example of such a disturbance of the IGM is called Minkowski's object [van Breugel et al., 1985] and is pictured in fig. 1.1. Out of the central BH of this radio galaxy, a huge and powerful jet is emanating and interacting with a gas cloud shown in blue. The hypothesis is that this causes the gas to collapse and stars to form. This is still debatable.



Figure 1.1: Minkowski's object, adapted from [van Breugel et al., 1985].

What has been proven is that jets, as well as other mechanisms, can produce galactic outflows as they accelerate gas to high velocities. Such jet outflows have been observed over the years through spectroscopy either in absorption or emission

in all gas phases; be it atomic or molecular. For example, shown in fig. 1.2 in the upper half of the top graph is the absorption of the neutral H atom (inverted). The outflow is clearly visible in the blue-shifted side of the galaxy. Below is the emission of the [O III] atom for the same galaxy. In the lower graph one can see the emission of the CO molecules for galaxy Mrk 231, with the outflow being clearly visible as the broad component under the CO line. Recently, it has been found that this molecular phase carries most of the mass [Dasyra and Combes, 2012]. In some cases, the mass of the molecular outflow can even reach 10% of the total gas reservoir. It is therefore of major importance for the galactic evolution, in particular if this gas gets lost from the reservoir that can form new stars. This can happen, for example, if the gas gets ejected outside galaxies or if it gets dissipated to the halo. In both cases, the time for the gas to return to a disk would be extremely high compared to a dynamical timescale.

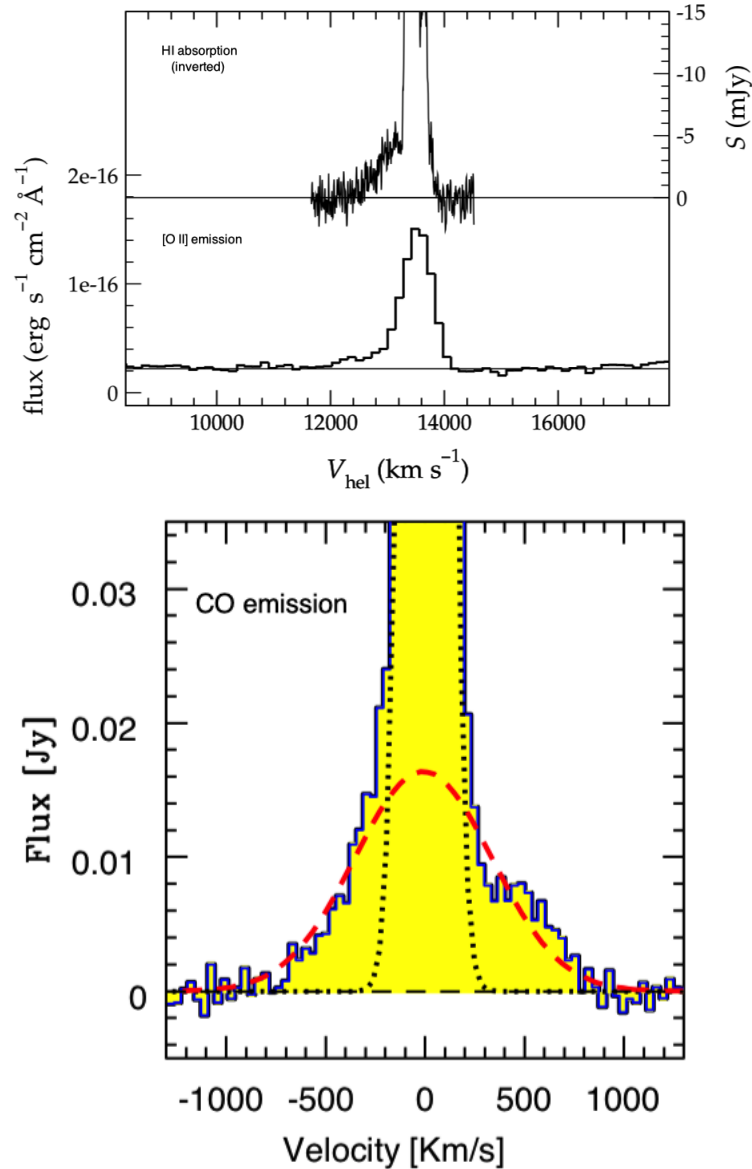


Figure 1.2: *Top*: Outflow in galaxy 3C 293 [Emonts et al., 2005]. *Bottom*: Outflow in galaxy Mrk 231 [Feruglio et al., 2010].

## 1.2 Selection of radio galaxies

Based on the aforementioned description of jet activity in galaxies, we aimed to study their effects in galaxies. We thus chose galaxies known to harbour outflows, indicating jet activity. They are presented below.

### 1.2.1 OQ 208

The first galaxy in our sample is OQ 208 or Mrk 0668. Its redshift is  $z = 0.07658 \pm 0.00013$ , which corresponds to a luminosity distance of  $\sim 340$  Mpc [Véron-Cetty and Véron, 1993]. It is classified as a QSO in the optical wavelengths [Lü, 1972] and as a blazar [Massaro et al., 2009] in the radio frequencies. OQ 208 is characterised by a



high emission in the IR, compared to other radio galaxies [Lanz et al., 2016]. In the optical wavelengths, the galaxy is visible in fig. 1.3, where the cross corresponds to its centre. Accordingly, in fig. 1.4, OQ 208 is depicted in much more detail in radio frequencies, since interferometry permits us to zoom in (more on that in sec. 1.3) and observe distant galaxies in minute spatial scales. Furthermore, fig. 1.5 portrays the spectral energy distribution (SED) of OQ 208.

We can detect two power laws. The one for the lower frequencies corresponds to synchrotron radiation and can be modeled as a function of the form  $f(\nu) \propto \nu^\alpha$ . For the higher frequencies ( $10^3$  GHz and above), Compton scattering prevails, which is described by another power law. In the regions between the two power laws, we can observe the spectrum of older stars on the low end and of younger stars on the high end of this frequency range. Another contributor is the accretion disk of the central black hole, as well as dust emission, found between the jet spectrum and the stellar spectrum, which in turn can be modeled as a modified black body (mbb).

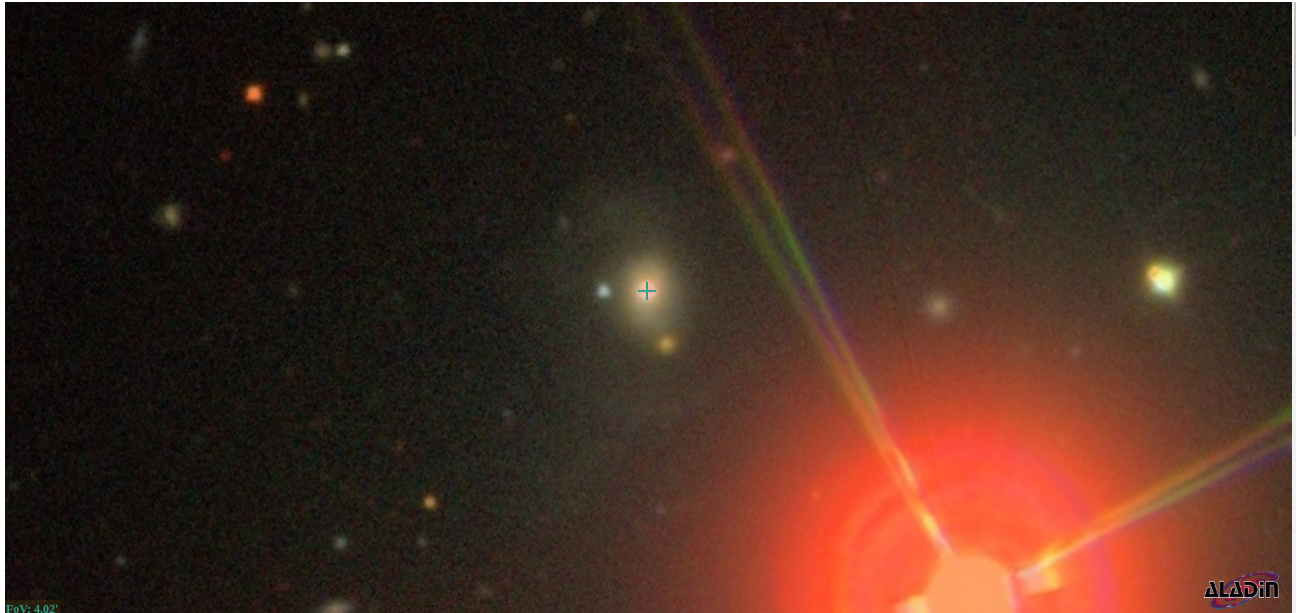


Figure 1.3: Composite image of three optical wavelengths (SDSS)

### 1.2.2 4C 12.50

Our next target was 4C 12.50 (fig: 1.6), for which a CO wind has been observed in absorption. This is a nearby radio galaxy ( $z = 0.12174 \pm 0.00002$ ), which is also an Ultraluminous Infrared galaxy, therefore again, very gas rich. It is a double system with a distance of 4 kpc between them. The merger is nearly complete, but structures out of equilibrium can still be seen. Such an example is the ridge that is seen north of the main nucleus in fig. 1.7, which is an HST image that probes mainly the [OIII] emission. It is noteworthy that this ridge has little stellar emission. Between the nucleus and the ridge there are filaments, along which the ionised gas has a high velocity dispersion [Holt et al., 2009].

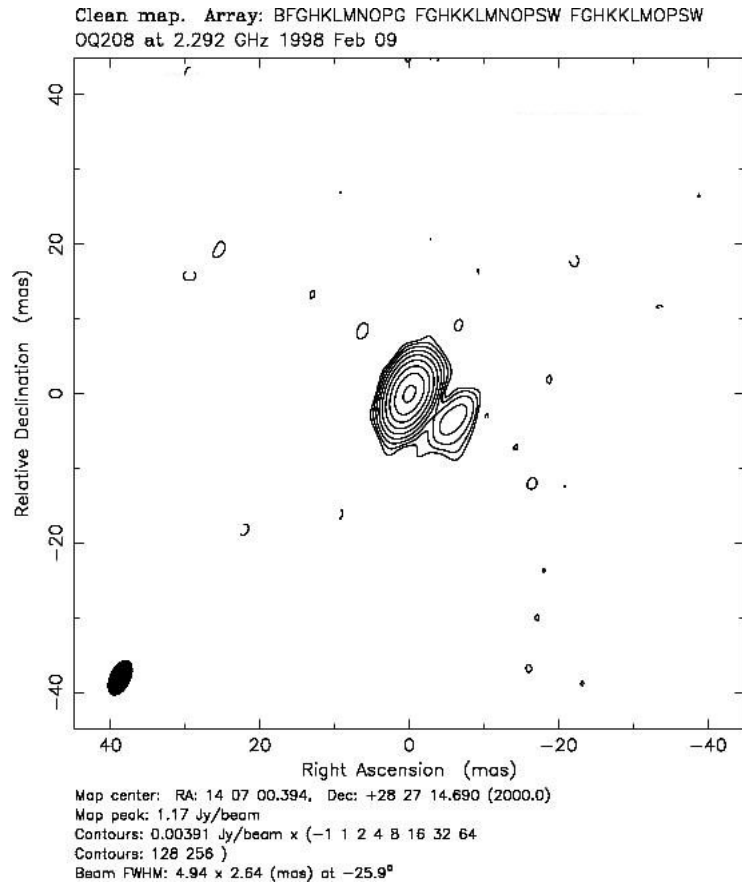


Figure 1.4: OQ 208's radio jets (VLBA, U.S. Naval Observatory)  
Ref. code: 2002RRFID.C...0000F

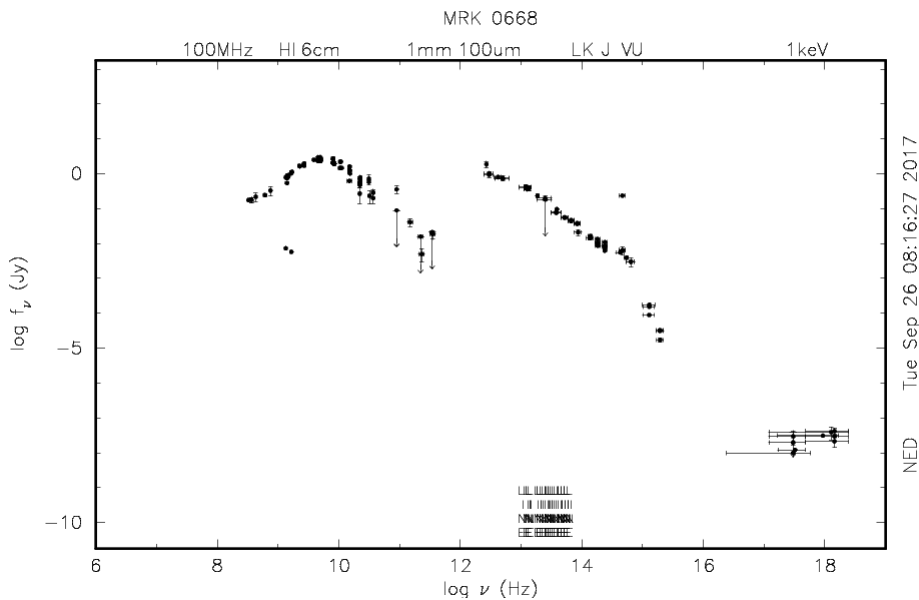


Figure 1.5: SED of OQ 208 (NED)

The NASA/IPAC Extragalactic Database (NED) is operated by the Jet Propulsion Laboratory, California Institute of Technology, under contract with the National Aeronautics and Space Administration.

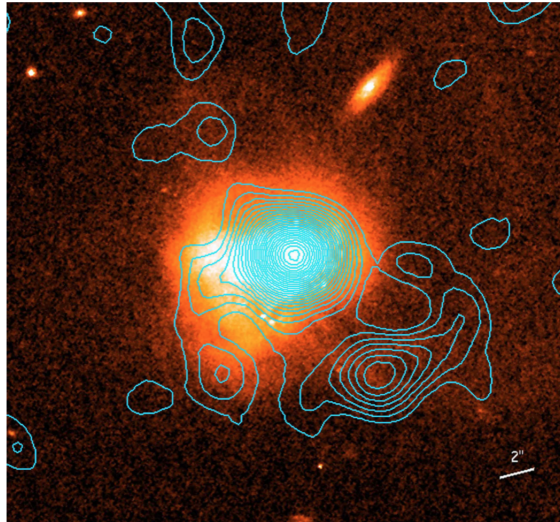


Figure 1.6: Contours of the CO ( $1 \rightarrow 0$ ) emission of 4C 12.50 [Dasyra et al., 2014]

In a work recently submitted by a member of our group [Fotopoulou et al., 2018], further wind signatures were detected in ALMA data, which we depict via the colourful contours (fig. 1.7). Each colour corresponds to a different outflow speed. More specifically, in the nucleus there was very broad emission (of  $\sim 2000$  km/s) with a signal-to-noise ratio of 6. In the filaments to the north, there is a smaller collection of outflowing clouds, at different velocity ranges (700, 1100, 1350 and 2100) km s $^{-1}$  with a signal-to-noise ratio again near 5.

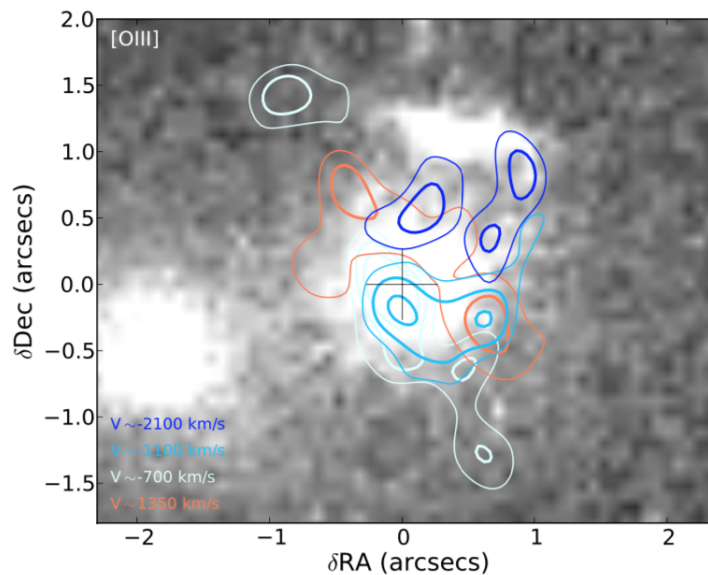


Figure 1.7: HST image of [OIII] [Fotopoulou et al., 2018]. Displayed are the loci of detections of high-velocity molecular clouds compared to the stellar and warm, ionized gas emission.

### 1.2.3 IC 5063

IC 5063 (fig. 1.8) is a Seyfert 2 object hosted by an early-type galaxy with a prominent dust lane which is seen edge on, at a redshift of  $z = 0.01135 \pm 0.00002$ . It is one of the most radio bright Seyfert objects with a power<sup>1</sup> of  $P_{1.4\text{GHz}} = 3 \times 10^{23} \text{ W Hz}^{-1}$  [Tadhunter et al., 2014]. In the radio continuum, IC 5063 shows a triple structure of about 4 arcsec in size (about 0.93 kpc, [Morganti et al., 1998]) aligned with the dust lane. HI emission ( $8.4 \times 10^9 M_{\odot}$ ) is traced in a regularly rotating warped disk with a radius  $\sim 2$  arcmin (about 28 kpc) and which is associated with the system of dust lanes [Morganti et al., 2015].

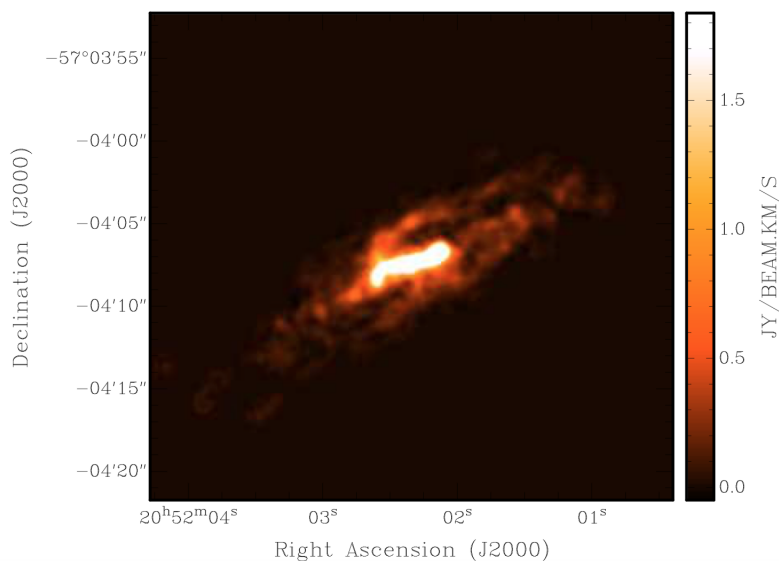


Figure 1.8: Total intensity image representing the distribution of the CO ( $2 \rightarrow 1$ ) in IC 5063 [Morganti et al., 2015]

IC 5063 was the first object where a fast, AGN driven massive outflow of HI was detected [Morganti et al., 1998]. This outflow was found to be located against the brightest radio hotspot, about 0.5 kpc from the radio core [Oosterloo et al., 2000] and this has been interpreted as evidence that the outflow is driven by the interaction of the radio jet with the surrounding ISM where the jet is moving in the plane of the large-scale gas disk of IC 5063 [Morganti et al., 2015].

Furthermore, IC 5063 is an unambiguous example of a jet initiating a galactic wind. Shown in fig. 1.9, adapted from [Dasyra et al., 2015] are winds starting in at least 4 regions along the jet trail. On the left we can clearly see the 4 starting points shown as contours over an HST image of ionised gas. We know that this also corresponds to the jet's trail, as the radio contour on the left are over the exact same region as the ionised gas.

Since the authors found this extended wind, they requested ALMA observations for 2 CO lines to study the cold, molecular gas. They found that in this system the gas exhibits indeed different conditions to the ones of the ambient ISM. Specifically,

<sup>1</sup>Assuming a Hubble constant  $H_0 = 70 \text{ km s}^{-1} \text{ Mpc}^{-1}$  and  $\Omega_{\Lambda} = 0.7$  and  $\Omega_M = 0.3$ , an angular scale distance to IC 5063 of 47.9 Mpc is used, implying a scale of 1 arcsec = 232 pc.

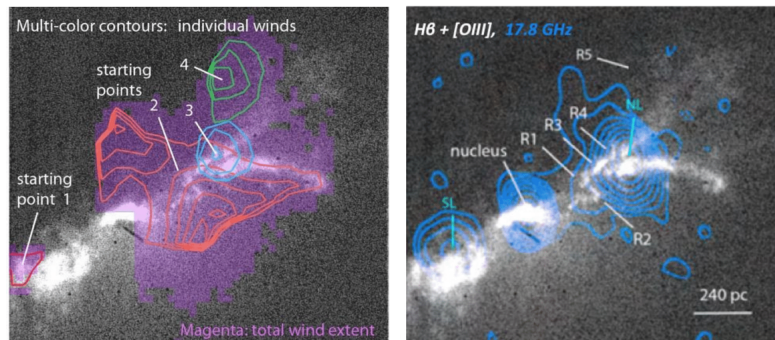


Figure 1.9: *Left*: Multicolour contours of the individual winds and total wind extension (magenta). *Right*: HST image of  $H\beta$  and  $[O\ III]$  with radio contours in blue from [Morganti et al., 2007].

they created a flux density ratio graph of the  $CO(4 \rightarrow 3)$  and  $CO(2 \rightarrow 1)$  lines (fig. 1.10) and found that in the jet impacted regions this ratio is well above 4, which is the upper limit for an optically thick medium and around 16 which is the upper limit for optically thin media. Therefore they assumed that the medium is optically thin and in LTE and created a temperature graph (fig. 1.10). As is clearly visible, the temperature reaches 200 K in the impacted regions, which is a whole order of magnitude higher than the one in the ambient ISM, where the temperature is around 20 K.

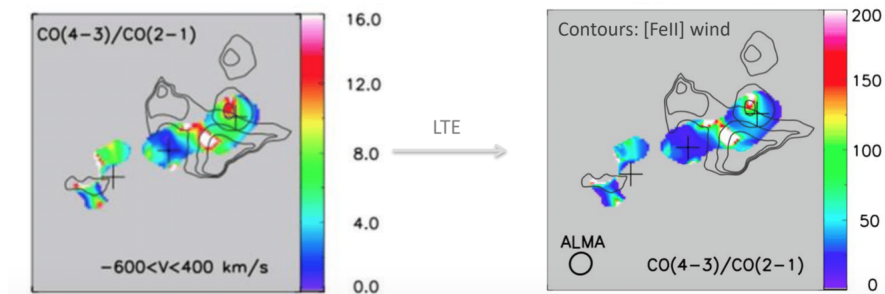


Figure 1.10: *Left*: Flux density ratio of  $CO(4 \rightarrow 3)$  over  $CO(2 \rightarrow 1)$  line transitions [Dasyra et al., 2015]. *Right*: Temperature graph depicting the jet impacted region compared to the ambient ISM, inferred from the inversion of eq. 3.20.

### 1.3 How to observe jets: Single dish vs. Interferometry

To study the aforementioned jets and their interactions with the ambient ISM we utilise telescope measurements. The telescopes suitable for this operate in the radio and sub-mm wavelengths. Radiation in the radio frequencies pierces through the most dense regions of galaxies. Extreme states of matter can be observed directly in emission, such as neutron stars and accretion disks around black holes. Since  $E_\gamma = h\nu$ , many low energy photons are observable. Furthermore, the highest resolution

can be achieved observing with the help of radio telescopes. The reason for this is that the angular resolution<sup>2</sup> rises as the beam size falls off. The relation between the diameter of the telescope used and the angular resolution that can be achieved is shown in eq. 1.1:

$$\theta = 1.22 \frac{\lambda}{D}, \quad (1.1)$$

where  $\theta$  is the angular resolution we are aiming for and  $\lambda$  the wavelength of the transition line we are studying (e.g. for the HI transition  $\lambda = 21$  cm).  $D$  is the diameter of the telescope.

These telescopes, known as single dish do have some restrictions. For example, standing waves are produced, which interfere with the measurement, mainly in the mm wavelengths. Another caveat illustrated in eq. 1.1 is that in order to achieve satisfactory spatial resolution, the diameter of the telescope must be enormous. A resolution of 1 arcsec for the HI line would require a telescope with a diameter of over 50 km, which is physically impossible. The largest, single dish telescope to date is the FAST telescope in China (fig. 1.12), with a diameter of 500 m, while the largest, steerable single dish telescope is the Green Bank Telescope in Virginia (fig. 1.11), which is 100 by 110 metres (ellipsoidally shaped).



Figure 1.11: The Green Bank Telescope (GBT) located in Virginia, USA, is the largest fully steerable, single dish radio telescope. Its surface is an ellipsoid, measuring 100 by 110 metres, with a collecting surface of  $9.3 \times 10^3$  m<sup>2</sup>. (Image credit: Wikipedia Commons)

These two examples illustrate the fact that single dish telescopes are restricted in their size. Fully steerable telescopes in particular are restricted by gravity, as they cannot be mounted to structures without collapsing after a certain mass and size threshold. So how do we improve them?

The next step is to use multiple antennas and utilise interferometry. Here the antennas are not used individually, but as part of an array, in order to improve the

---

<sup>2</sup>The angular resolution is the solid angle of the cone that passes through the points where the responsiveness of the antenna halves; also known as the beam.



Figure 1.12: The Five hundred meter Aperture Spherical Telescope (FAST) located in China is the largest single dish telescope. Its diameter is 500 m, resulting in a collecting surface of  $196 \times 10^3 \text{ m}^2$ . (Image credit: VCG/VCG via Getty Images)

achievable resolution. An interferometer can be made up of a different number of antennas but regardless of facility, the antennas always work in pairs of two. The reason behind this, is that interferometry is based on Young's double slit experiment, shown in fig. 1.13. The resulting radiation measured is due to reinforced interference. In astrophysics, the distance between to consecutive fringes, for a small angle approximation  $\sin(\theta) \approx \theta$  is given by eq. 1.2:

$$\theta = \frac{\lambda}{B}. \quad (1.2)$$

Eq. 1.2 is the same as 1.1, but instead of the diameter  $D$  of the telescope, we now are using the maximum distance between 2 telescopes  $B$ , known as the baseline. The further away we place the antennas (or in other words, the larger the baseline), the better our maximum resolution.

Fig. 1.14 illustrates the difference between a single dish telescope and the synthesised beam of an interferometer like ALMA (more on ALMA in sec. 1.4).

Our measurements of the source in the sky are transformed into the  $u$ - $v$  plane. The coordinates  $u$  and  $v$  simply describe the vectorial separation between each pair of interferometer elements measured in wavelengths, as seen from the source

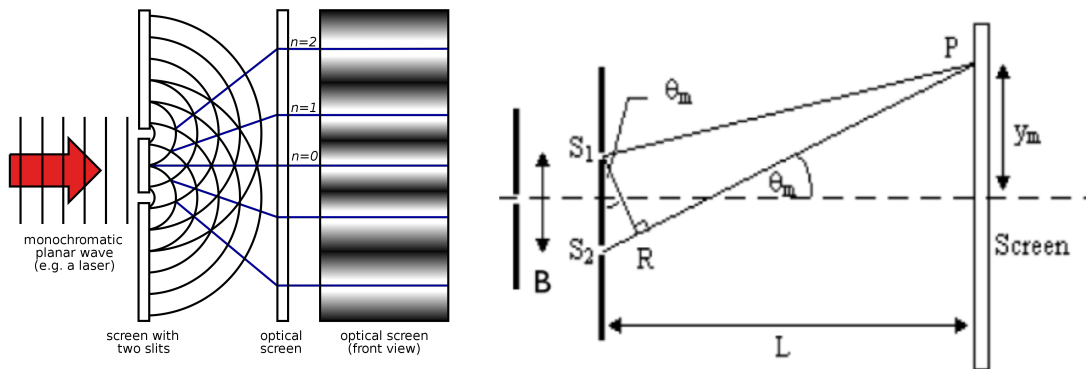


Figure 1.13: Young's double slit experiment. (Image credit: Wikipedia Commons)

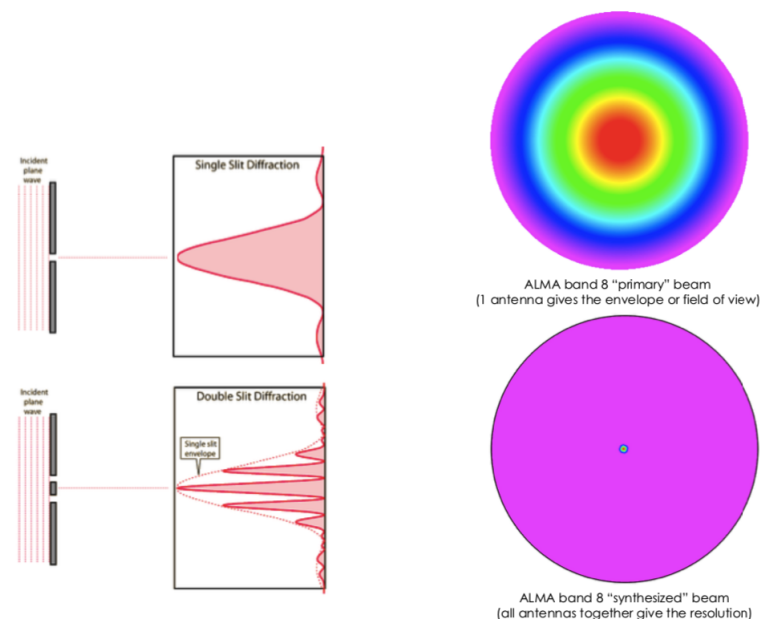


Figure 1.14: Single dish vs. Interferometric beam.

(projection). Hence, if an observer was looking towards the array from the source's point of view, he would see the baseline. Since the baseline is a projection, it is entirely visible only if it is vertical to the line of observation.

The units of the  $u$ - $v$  plane are usually meters, whereas the the flux is shown relative to the extent of the source in the sky in arcsec. Thus we need a 2 dimensional Fourier transformation, to get to the so called image plane. The reason we can use the Fourier transform is that according to eq. 1.1 the two quantities are inversely proportional. The transform is written as follows:

$$T(x, y) = \iint \mathcal{V}(u, v) e^{-2\pi i(u x + v y)} du dv. \quad (1.3)$$

The reverse Fourier transform must also be performed due to the way the data is obtained. Specifically the signal (both the amplitude and the phase) are correlated per 2 antennas and are therefore already in Fourier space, having been obtained



using:

$$\mathcal{V}(u, v) = \int_{-\infty}^{\infty} \int_{-\infty}^{\infty} \mathcal{A}(l, m) I(l, m) e^{-2\pi i(u l + v m)} dl dm, \quad (1.4)$$

where  $\mathcal{A}$  is antenna reception pattern, corresponding to the primary beam. The correlated data are called visibilities and  $\mathcal{V}(u, v)$  is the visibility function, measured as a function of position in the u-v plane.

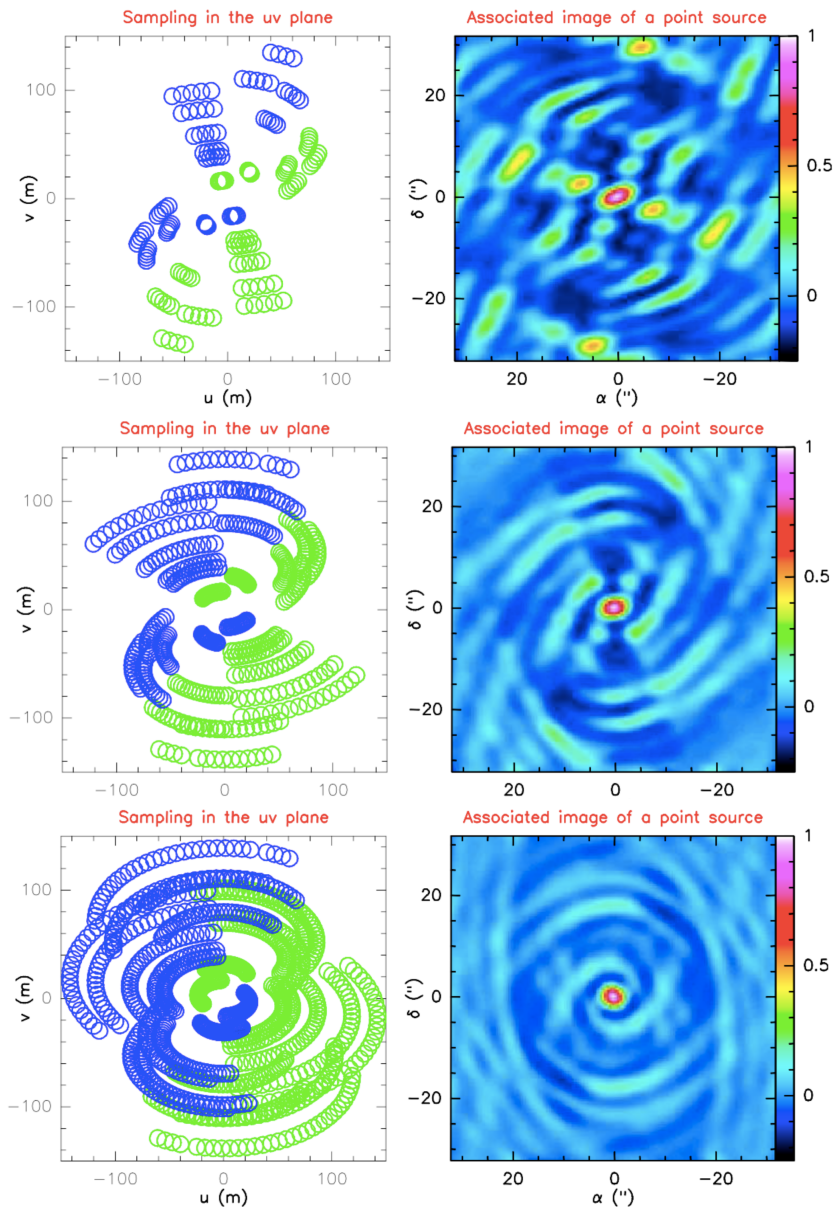


Figure 1.15: Shown in these three graphs is the u-v plane initially and how the rotation of the Earth fills out the u-v plane.

As stated in the title of this project, we aim to study spatially resolved jets. We therefore can only utilise interferometric data to achieve the desired resolution, as was laid out in the aforementioned analysis. The telescopes we used to obtain our data are presented below.

## 1.4 Radio telescopes / Interferometers

### 1.4.1 ALMA

The Atacama Large Millimeter Array (ALMA) consists of a giant array of 12 m antennas, with at least 50 antennas available (the 12-m array), with baselines up to 16 km, and an additional compact array of  $12 \times 7$  m and  $4 \times 12$  m antennas to greatly enhance ALMA's ability to image extended targets, located on the Chajnantor plateau at 5000 m altitude. The antennas can be placed in different locations on the plateau in order to form arrays with different distributions of baselines. More extended arrays will provide higher spatial resolution, more compact arrays provide better sensitivity for extended sources. Additionally, there is the Atacama Compact Array (ACA), which mostly stays in a fixed configuration and is used to image large scale structures that are not well sampled the by antennas in the remaining/extended configurations. ALMA delivers data cubes, of which the third axis is frequency.

The frequency range available to ALMA is divided into different receiver bands. Data can only be taken in one band at a time. These bands range from band 3, starting at 84 GHz, to band 10, ending at  $\sim 950$  GHz. For comparison, a frequency of 300 GHz translates to a wavelength of approximately 1 mm. For example, band 3 was used during the testing and commissioning of the antennas, because its low frequency minimises the effects of atmospheric variations. During science operations, band 3 is routinely used to perform phase calibration of observations taken at both band 3 and higher frequencies. Additionally, it can be used to image molecules in nearby galaxies at high resolution, to probe the cold interstellar medium of galaxies, and to peer into dust-obscured galaxies to observe star formation. Band 9 on the other hand is one of the highest frequency bands in the baseline ALMA project, and offers some of the telescope's highest spatial resolution. The observations made possible by the band 9 receivers allow astronomers to study molecular clouds - the dense regions of gas and dust where new stars are being born - at higher temperatures and densities, and with higher angular resolution, thus complementing the longer wavelength bands. An example of the pattern received from a cartridge (receiver unit) of band 9 is shown in [1.16](#).

The field of view of an interferometer is determined by the size of the individual antennas and the observing frequency. It is independent of the array configuration. The field of view is expressed in terms of the primary beam, which describes the antenna response (sensitivity) as function of the angle away from the main axis. The main lobe of the primary beam can be approximated by a Gaussian function. Sidelobes appear as well, although outside of it. The angular diameter of the primary beam, at the 20% level of the peak of the Gaussian function. The full-width-at-half-maximum (FWHM) of the ALMA primary beam is  $21''$  at 300 GHz for a 12 m antenna and a  $3''$  for a 7 m antenna, and scales linearly with wavelength (diffraction limit of a single antenna, as opposed to that of the whole array). To achieve uniform sensitivity over a field larger than about a few arcsec, or to image larger regions than the primary beam, mosaicking is required, which is a standard observing mode for ALMA.

In the most compact 12 m array configurations ( $\sim 160$  m), resolutions range from  $0.5''$  at 950 GHz to  $4.8''$  at 110 GHz. In the most extended 12 m array configuration

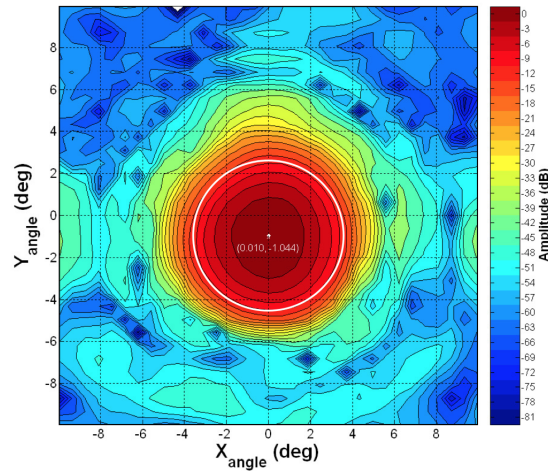


Figure 1.16: Typical co-polar beam pattern in a Band 9 cartridge, with the angular extent of the secondary telescope mirror indicated (white circle). This pattern corresponds to polarization 0 in cartridge #63 [Baryshev et al., 2015].

( $\sim 16$  km), the resolutions range from 20 mas at 230 GHz to 43 mas at 110 GHz. These numbers refer to the FWHM of the synthesized beam (point spread function), which is the inverse Fourier transform of a (weighted)  $u$ - $v$  sampling distribution. The resolution in arcsec can be approximated as:  $\text{FWHM (")} = 76 / \text{maximum baseline (km)} / \text{frequency (GHz)}$ .

## 1.4.2 NOEMA

The NOEMA Interferometer, situated on the Plateau de Bure at 2550 m altitude in the French Alps, is currently the most advanced millimeter array in the Northern Hemisphere.

During its history, the observatory at the Plateau de Bure underwent several track extensions, received additional antennas (all of 15 m diameter and similar construction as the first ones) and technical upgrades. From a three antenna interferometer with a maximum baseline of 288 m in 1988, it has evolved to a ten-antenna array with baselines up to 760 m. A new generation of powerful dual-polarisation receivers for the 3 mm and 1 mm observing bands was installed in 2006, and extended to the 2 mm observing band in late 2007, and to the 0.8 mm band at the end of 2010. With the inauguration of the seventh antenna in September 2014, the observatory has started its transformation into NOEMA (Northern Extended Millimeter Array).

The antennas of the NOEMA interferometer can move on rail tracks up to a maximum separation of currently 760 m in the E-W direction and 368 m in the N-S direction, corresponding to a resolution of 0.5 arcsecs at an observing wavelength of 1.3 mm (230 GHz).

### 1.4.3 SMA

The Submillimeter Array (SMA) consists of  $8 \times 6$  m radio telescopes arranged as an interferometer for sub-mm wavelength observations. It is the first purpose-built sub-mm interferometer, constructed after successful interferometry experiments using the pre-existing 15-meter James Clerk Maxwell Telescope and 10.4 meter Caltech Submillimeter Observatory as an interferometer. All three of these observatories are located at Mauna Kea Observatory on Mauna Kea, Hawaii, and can be operated together as a ten element interferometer in the 230 and 345 GHz bands. The baseline lengths presently in use range from 16 to 508 m. The radio frequencies accessible to this telescope range from 180 to 418 GHz which includes rotational transitions of dozens of molecular species as well as continuum emission from interstellar dust grains. Although the array is capable of operating both day and night, most of the observations take place at nighttime when the atmospheric phase stability is best.

# Chapter 2

## Data

### 2.1 Sub-mm interferometry for galaxy OQ 208

For the galaxy OQ 208 there were the first three CO transition lines available to us. The CO ( $1 \rightarrow 0$ ) and CO ( $2 \rightarrow 1$ ) lines were carried out with the Plateau de Bure (PdB) Interferometer of the Institut de Radioastronomie Millimétrique (IRAM) as part of the program W086 (PI Dasyra) in 2012. MWC349 was used as the flux calibrator and the data reduction was performed using the GILDAS MAPPING environment, developed by IRAM for the reduction of such data.

The observations of CO ( $3 \rightarrow 2$ ) in OQ 208 were carried out with the Sub-Millimeter Array (SMA) of the Smithsonian Astrophysical Observatory and the Academia Sinica Institute of Astronomy and Astrophysics as part of the program 2012B-S013 (PI Dasyra) in 2013. Callisto and Titan were used as flux calibrators. Manual clipping of bad channels prior to processing the data was performed, in a manner similar to that applied for the PdB data. Further information on the above procedure can be found in my Bachelor Thesis.

### 2.2 ALMA data of galaxy 4C 12.50

ALMA observed 4C 12.50 in May (band 7) and July (band 3) 2015, when the array had 37 operational antennas. The observations, which were part of the cycle 2 program 2013.1.00180.S (PI Dasyra), were performed in bands 3, 7, and 8. In all bands, four spectral windows of 1.875 GHz bandwidth were employed. In band 3, one spectral window to cover the velocity range  $-3300 \text{ km s}^{-1}$  to  $2100 \text{ km s}^{-1}$  around the CO ( $1 \rightarrow 0$ ) line was used, and one spectral window to cover the velocity range  $-3800 \text{ km s}^{-1}$  to  $1100 \text{ km s}^{-1}$  around the HCS+ ( $3 \rightarrow 2$ ) line. The other two spectral windows targeted the continuum at rest frame  $2.641 (\pm 0.026) \text{ mm}$  and  $2.364 (\pm 0.021) \text{ mm}$ . In band 7, two partially overlapping spectral windows were used, to cover the velocity range  $-2600 \text{ km s}^{-1}$  to  $900 \text{ km s}^{-1}$  around the CO ( $3 \rightarrow 2$ ) line, and two spectral windows to obtain the restframe  $896 (\pm 3) \mu\text{m}$  and  $902 (\pm 3) \mu\text{m}$  continuum. In band 8, two spectral windows were used, to cover the velocity range  $-1350 \text{ km s}^{-1}$  to  $840 \text{ km s}^{-1}$  around the CO ( $4 \rightarrow 3$ ) line, one spectral window to target the HCO+ ( $5 \rightarrow 4$ ) line, and one spectral window to obtain the continuum at restframe  $668.4 (\pm 1.7) \mu\text{m}$ . For the line observations, a velocity bin

of  $5 (\pm 1) \text{ km s}^{-1}$  was typically chosen, which is well suited for the detection of lines originating from small cloud ensembles (either in emission or in absorption in front of a background continuum). For the continuum observations, a coarser velocity bin of  $\sim 20$  up to  $\sim 90 \text{ km s}^{-1}$  was chosen. For further details see [Fotopoulou et al., 2018].

## 2.3 ALMA data of galaxy IC 5063

To study the gas excitation, we used ALMA archival data for the CO ( $1 \rightarrow 0$ ) and CO ( $3 \rightarrow 2$ ) line transitions, from the programs 2015.1.00420.S (PI Combes) and 2015.1.00467.S (PI Morganti). The observations for the CO ( $1 \rightarrow 0$ ) line transitions were taken on April 17 and August 14 of 2015 and July 25 of 2017 respectively. For the CO ( $3 \rightarrow 2$ ) line transition the observation dates were April 15 of 2016 and March 22 of 2016.

We also used CO ( $2 \rightarrow 1$ ) data from the program 2012.1.00435.S ([Morganti et al., 2015]). Thirty one antennas observed IC 5063 in band 6 for 30 minutes on source. J2056-4714 was used as bandpass and phase calibrator, Neptune as flux calibrator. Four 1.875 GHz bandwidth spectral windows were employed, with one of them covering the  $\pm 1000 \text{ km s}^{-1}$  range around CO ( $2 \rightarrow 1$ ). The flux calibration was performed in CASA 4.2.2. Imaging was carried out in CASA 4.6.0 (because of continuum subtraction improvements). The cube was created at a  $\pm 25 \text{ km s}^{-1}$  spectral bin and at a 0.1 arcsec pixel scale. The synthesized beam was  $0.56 \times 0.53$  arcsec. For further information, refer to [Dasyra et al., 2016].

New, band 8 data of IC 5063 were also taken with ALMA on May 18 2016 for the program 2015.1.00420.S (PI Combes). Forty two antennas observed the galaxy for 39 minutes on source. Three 1.875 GHz bandwidth spectral windows were employed. Two of the spectral windows were partly overlapping to cover the  $\pm 1000 \text{ km s}^{-1}$  range around CO ( $4 \rightarrow 3$ ). The third spectral window was used for duplication purposes in the  $\pm 300 \text{ km s}^{-1}$  range: its role was to ensure that no significant continuum offset exists between the former windows due to flux and bandpass calibration uncertainties. The data were reduced within the Common Astronomy Software Applications (CASA) environment, version 4.6.0. The calibration script was executed as delivered by ESO. Pallas, J1924-2914, and J2056-4714 were respectively used as flux, bandpass, and phase calibrators. The flux calibration accuracy was better than 5%, as cross-checked with J1924-2914, which is not variable as J2056-4714 is. To construct images from visibilities, we chose a  $25 \text{ km s}^{-1}$  spectral bin and a 0.06 arcsec pixel scale. The synthesized beam size was  $0.4 \times 0.4$  arcsec.

# Chapter 3

## Method of data processing

### 3.1 Grid creation of physical parameters using RADEX

In order to create the maps of the physical quantities of interest, we needed to model our data. We used a well known, publicly available fitting code. It is called RADEX [van der Tak et al., 2007]. RADEX calculates the intensities of atomic and molecular lines in a uniform medium based on a statistical equilibrium involving collisional and radiative processes and including background radiation. A brief explanation of its formalism follows.

In order to calculate the intensities, one must first describe the transfer of radiation. This is done using the radiative transfer equation

$$\frac{dI_\nu}{ds} = j_\nu - \alpha_\nu I_\nu, \quad (3.1)$$

where  $j_\nu$  and  $\alpha_\nu$  are the local emission and extinction coefficients, respectively. It is convention to define a source function  $S_\nu \equiv \frac{j_\nu}{\alpha_\nu}$  and thus eq. 3.1 yields the solution

$$I_\nu = I_\nu(0)e^{-\tau_\nu} + \int_0^{\tau_\nu} S_\nu(\tau'_\nu) e^{-(\tau_\nu - \tau'_\nu)} d\tau'_\nu, \quad (3.2)$$

where  $I_\nu$  is the radiation emerging from the medium and  $I_\nu(0)$  is the "background" radiation entering the medium. RADEX concerns itself with bound bound transitions in an N-level molecule.  $A_{ul}$  is the spontaneous downward rate,  $B_{ul}$  and  $B_{lu}$  the Einstein coefficients for stimulated transitions, and  $C_{ul}$  and  $C_{lu}$  collisional rates between upper levels  $u$  and lower levels  $l$ . The rate of collision is equal to

$$C_{ul} = n_{\text{col}}\gamma_{ul}, \quad (3.3)$$

where  $n_{\text{col}}$  is the number density of the collision partner (in  $\text{cm}^{-3}$ ) and  $\gamma_{ul}$  is the downward collisional rate coefficient (in  $\text{cm}^3 \text{s}^{-1}$ ). The next step is to express the emission and absorption coefficients as a function of the the Einstein coefficients.

The local emission in transition  $u \rightarrow l$  with laboratory frequency  $\nu_{ul}$ , can be expressed as

$$j_\nu = \frac{h\nu_{ul}}{4\pi} n_{ul} A_{ul} \phi_\nu \quad (3.4)$$

where  $n_u$  is the number density of molecules in level  $u$  and  $\phi_\nu$  is the frequency-dependent line emission profile, which is approximated as Gaussian line profile. The absorption coefficient on the other hand reads

$$\alpha_\nu = \frac{h\nu_{ul}}{4\pi} (n_l B_{lu} - n_u B_{ul}) \phi_\nu. \quad (3.5)$$

The source function is then

$$S_{\nu_{ul}} = \frac{n_u A_{ul}}{n_l B_{lu} - n_u B_{ul}} = \frac{2h\nu_{ul}^3}{c^2} \left( \frac{g_u n_l}{g_l n_u} - 1 \right)^{-1} \quad (3.6)$$

and we can also define the excitation temperature  $T_{\text{ex}}$  through the Boltzmann equation:

$$\frac{n_u}{n_l} = \frac{g_u}{g_l} \exp[-(E_u - E_l)/kT_{\text{ex}}], \quad (3.7)$$

such that  $S_{\nu_{ul}} = B_\nu(T_{\text{ex}})$  is the specific intensity of a blackbody radiating at  $T_{\text{ex}}$ .

If the level populations  $n_i$  are known, the radiative transfer equation can be solved exactly. The difficulty in solving radiative transfer problems is the interdependence of the molecular level populations and the local radiation field, requiring iterative solution methods. In particular, for inhomogeneous or geometrically complex objects, extensive calculations with many grid points are required. However, if only the global properties of an interstellar cloud are of interest, the calculation can be greatly simplified through the introduction of a geometrically averaged escape probability  $\beta$ , the probability that a photon will escape the medium from where it was created. This probability depends only on the optical depth  $\tau$  and is related to the intensity within the medium, ignoring background radiation and any local continuum, through  $\bar{J}_{\nu_{ul}} = S_{\nu_{ul}}(1 - \beta)$ , where is the specific intensity  $I_\nu$  integrated over the solid angle  $d\Omega$  and the frequencies times the profile  $\phi_\nu$ . In the case of a static, spherically symmetric and homogeneous medium the escape probability is [Osterbrock and Ferland, 2006]

$$\beta_{\text{sphere}} = \frac{1.5}{\tau} \left[ 1 - \frac{2}{\tau^2} + \left( \frac{2}{\tau} + \frac{2}{\tau^2} \right) e^{-\tau} \right]. \quad (3.8)$$

But now the optical depth at the line centre can be written explicitly, by combining the relation for the source function with eqs. 3.4, 3.6 and using the fact that  $\phi_\nu$  is approximated by a Gaussian line profile, as follows:

$$\tau = \frac{c^3}{8\pi\nu_{ul}^3} \frac{A_{ul} N_{\text{mol}}}{1.064\Delta V} \left[ x_l \frac{g_u}{g_l} - x_u \right], \quad (3.9)$$

for a homogeneous medium with no global velocity field. Here  $N_{\text{mol}}$  is the total column density,  $\Delta V$  the full width at half-maximum of the line profile in velocity



units, and  $\chi_i$  the fractional population of level  $i$ . Therefore, the program can now iteratively solve the statistical equilibrium equations starting from optically thin statistical equilibrium for the initial level populations, with the main collisional partner in dense molecular clouds being  $\text{H}_2$ .

Having the aforementioned formalism in mind, we now focus on the code itself. Its input is the kinetic temperature ( $T_{\text{kin}}$ ), number density of the  $\text{H}_2$  molecule ( $n_{\text{H}_2}$ ), and column density of the CO molecule ( $N_{\text{CO}}$ ) for a given line width. A beam filling factor needs to also be provided, to model the theoretical fluxes to the observed ones<sup>1</sup>. Its output is the background subtracted radiation temperature<sup>2</sup> ( $T_{\text{R}}$ ), which we turn into a line intensity in the Rayleigh-Jeans (RJ) limit. We produced numerous such outputs for a grid of input parameters and used a  $\chi^2$  minimisation (see sec. 3.3) to find the best parameter set of the  $T_{\text{kin}}$ , excitation temperature ( $T_{\text{ex}}$ ),  $n_{\text{H}_2}$ ,  $N_{\text{CO}}$  and optical depth ( $\tau$ ). Then, as an output, we create maps of these parameters, as well as of the pressure.

The starting point for this project was based on the work of Mr. Skretas, who is another member of our group, in his BSc. thesis. He studied galaxy IC 5063 with the aforementioned procedure. Specifically he created output grids and produced his results by constraining the limits of the grid used each time. Thus he found the best fit for each pixel for a given grid. Given this approach's limitation, we implemented assumptions and constraints on RADEX's output values. Furthermore, we generalised and optimised the scripts used to run the maps, shown in A.2. The script now runs for the first 10 line transition for the CO molecule. Additional molecules can easily be added in the future. The added assumptions and constraints are explored in sec. 3.3.

## 3.2 Creation of collapsed images from 3D cubes

The starting point for a map of a physical quantity is a two dimensional image of the galaxy, where each pixel is characterised by the corresponding flux measured. Below we describe the procedure followed to end up with such an image, starting from a data cube.

Firstly, one must determine between which velocity ranges or channels the emission line is located. This can be achieved by using a data cube processing software; here, in particular, we use the functionalities of GILDAS MAPPING. After having determined the velocity range, we "collapse" the cube into those channels, meaning that we integrate the flux from all frequencies, corresponding to each pixel. Thus, the output is a two dimensional image. For the further collapse of a 2D-image into a 1D integrated flux, it is necessary to convert the units of the pixels into units of flux (Jy), if the value of the pixels is in Jy per beam.

Since we deal with different beam sizes, we also need to convolve the images into a common resolution. This is achieved by using the image tool provided in the Common Astronomy Software Applications (CASA) package. The major and minor

<sup>1</sup>The code assumes that the molecular clouds cover the entirety of the beam. Since that is not the case, the beam filling factor, which is a percentage of the area of the beam that is covered by molecular clouds, must be factored into the equations.

<sup>2</sup>Antenna temperature.

axis of the large beam needs to be provided, as well as the position angle. If the images are of different spatial size, they are also regridded, again using the image tool of CASA.

As the goal is to study as many CO line transitions as possible combined, we apply a common mask to the two dimensional images. Specifically, a mask is created for each individual image, by keeping pixels with a signal of  $5\sigma$  or more above the noise<sup>3</sup> and then all masks are combined into a single one, keeping only those pixels that satisfy the aforementioned condition for all images. The final product is a set of two dimensional images for all available line transitions depicting the common pixels above the threshold of  $5\sigma$ .

### 3.3 Assumptions, boundary conditions and trials

Having both a grid and two dimensional images, we wrote a python script to loop over the grid and find the best fit by using a  $\chi^2$  minimisation. Specifically we aimed to minimise the difference between the measured flux and the theoretical RJ flux, put out by RADEX. The initial grid we used was comprised of  $T_{\text{kin}} \in [5, 200]$  K, with a step of 1 K (196 temperature points),  $n_{\text{H}_2} \in [10^3, 10^7]$   $\text{cm}^{-3}$ , with 80 logarithmic number density points and  $N_{\text{CO}} \in [10^{13}, 10^{19}]$   $\text{cm}^{-2}$ , with 140 logarithmic column density points. These upper and lower boundaries are based on previous work by Mr. Skretas. He set out to replicate the diagnostic graphs by [Oosterloo et al., 2017] and [van der Tak et al., 2007], by logarithmically plotting the  $T_{\text{kin}}$  and  $n_{\text{H}_2}$  for given  $N_{\text{CO}}$ s, where the ratio of the CO ( $4 \rightarrow 3$ ) over the CO ( $2 \rightarrow 1$ ) line transition reached either a maximum, a minimum or a median value. The aim was to find out where the RADEX code works well and where it breaks down. Apart from the upper and lower boundaries mentioned here, he also found that the code breaks down for optical depths in excess of 100.

Combining these results with our own assumptions and boundary conditions, we first present the assumptions we used and then the added boundary conditions. The reason behind this is that a simple  $\chi^2$  minimisation between the theoretical and the observed flux was not sufficient to break the different degeneracies occurring between the physical quantities we mapped. The output maps exhibited sharp breaks and discontinuities in the maps of the various parameters. For example the  $T_{\text{kin}}$  reached higher values on the edge of the galaxy than in the nucleus. The opposite happened for the  $n_{\text{H}_2}$ . Therefore we implemented the following physical assumptions in order to break those degeneracies:

- $\chi^2 < \sum_{i=1}^k 5^2$ .

We decided to reject  $\chi^2$  solutions that exceeded  $5\sigma$ . The reduced  $\chi^2$  minimisation we use is of the form

$$\chi^2 = \sum_{i=1}^k \frac{(O_i - E_i)^2}{\sigma^2}, \quad (3.10)$$

---

<sup>3</sup>The noise is calculated by computing the standard deviation of all pixels.

where  $O_i$  is the theoretical flux and  $E_i$  the experimental flux for each pixel, while  $\sigma$  is the experimental error. As previously mentioned, we run a minimisation for the flux of each spatial pixel compared to the theoretical flux put out by RADEX. Consequently, a  $\chi^2$  of  $5\sigma$  would be  $O_i = E_i \pm 5\sigma$ , leading to  $\chi_{5\sigma}^2 = \sum_{i=1}^k 5^2$ .

- $\frac{\max(n_{\text{H}_2}^{i,j-1}, n_{\text{H}_2}^{i,j})}{\min(n_{\text{H}_2}^{i,j-1}, n_{\text{H}_2}^{i,j})} < 3$ , where  $i, j$  refer to the pixel indices.

In order to avoid gradients over an order of magnitude between neighbouring pixels, we assumed that the maximum value of the  $n_{\text{H}_2}$  of the two neighbouring pixels cannot exceed 3.3 (rounded to 3) times the value of the minimum pixel. For each map we also studied the  $n_{\text{H}_2}$  histograms (see sec. 3.4) to check if this ratio was realistic.

- $n_{\text{H}_2} \leq n_{\text{H}_2}^{\text{central}}$ .

During the initial run for maps we assumed that the  $n_{\text{H}_2}$  falls off as we move towards the outer regions. However, this does not hold true for all galaxies and we therefore did not use this assumption in all of the maps. Since Python reads an array by line, starting at (0,0), we needed to implement a new way for the code to loop over such an array. We decided to use a clockwise spiral, starting from the centre. Thus, we associated spatially neighbouring pixels to each other, therefore enabling us to perform the desired constraints.

- $\frac{\text{flux}-1\sigma}{\text{flux}_{\text{central}}} < \frac{N_{\text{CO}}}{N_{\text{CO}}^{\text{central}}} < \frac{\text{flux}+1\sigma}{\text{flux}_{\text{central}}}$ .

A sound physical assumption is to presume that the  $N_{\text{CO}}$  is distributed the same way the CO (1  $\rightarrow$  0) flux is distributed, within  $1\sigma$ . This means comparing the ratio of the  $N_{\text{CO}}$  over the  $N_{\text{CO}}$  of a reference pixel to ratio of the CO (1  $\rightarrow$  0) of each pixel over the CO (1  $\rightarrow$  0) of the same reference pixel. The three reference pixels we tried out were the central, the median flux pixel and the minimum flux pixel, both for the CO (1  $\rightarrow$  0) line transition. The resulting maps indicated that the right choice would be the central pixel, which we adopted.

Moving on the boundary conditions:

- $0 < \tau < 100$ .

Apart from the code breaking down at values over 100 for the optical depth, we excluded solutions with a negative optical depth.  $\tau < 0$  corresponds to maser emission (induced emission), which is not present in the systems we are focusing on.

- $T_{\text{R}} > T_{\text{R}_{\text{obs}}}$ .

For the  $T_{\text{R}}$  we can establish this lower boundary of acceptable temperatures, as they are given by the RADEX code. To do this, we start from the RJ equation<sup>4</sup>:

<sup>4</sup>Although the RJ equation does not always hold in the sub-mm wavelengths, it is assumed by the RADEX code.

$$B_\nu = \frac{dE}{d\Omega dt d\nu dA} \stackrel{\text{RJ: } \frac{h\nu}{k_B T_{\text{ex}}} \gg 1}{\Leftrightarrow} \frac{2 k_B T_{\text{R}} \nu^2}{c^2}.$$

By substituting the constants we get:

$$B_\nu = 3.07 \times 10^4 T_{\text{R}} \nu^2 \left[ \frac{\text{Jy}}{\text{sr}} \right],$$

and if we integrate over the frequencies

$$B = \int B_\nu d\nu = 3.07 \times 10^4 \int T_{\text{R}} \nu^2 d\nu \left[ \frac{\text{Jy}}{\text{sr}} \right] \stackrel{\frac{\Delta v}{\nu} \approx \frac{c}{\nu}}{\Leftrightarrow} \\ B = 1.02 \times 10^8 T_{\text{R}} \nu^3 \Delta v \left[ \frac{\text{Jy Hz}}{\text{sr}} \right]. \quad (3.11)$$

For the above result  $\nu$  is in GHz,  $T_{\text{R}}$  in Kelvin and  $\Delta v$  in  $\text{km s}^{-1}$ . Finally, we integrate over the entire solid angle to get the total flux

$$F = \int B d\Omega = 1.08 \times 10^8 T_{\text{R}} \nu^3 f \Delta v \pi \alpha^2 [\text{Jy Hz}] \stackrel{F = \frac{\text{flux} \nu \times 10^9}{c}}{\Leftrightarrow} \\ \frac{(\nu \times 10^9) \text{flux}}{c} = 1.08 \times 10^8 T_{\text{R}} \nu^3 f \Delta v \pi \alpha^2 [\text{Jy Hz}], \quad (3.12)$$

where  $f$  is the beam filling factor we added by hand and  $\pi \alpha^2$  is the emitting region size<sup>5</sup>. This correction is implemented by inserting  $f$ . In order to find the minimum plausible  $T_{\text{R}}$ , we use the maximum value for the beam filling factor, which is 1 and the flux of the minimum pixel. We then solve for the observed radiation temperature and get

$$T_{\text{R}_{\text{obs}}} = \frac{\text{flux}_{\text{min}} \times 10^9}{1.08 \times 10^8 \pi \alpha^2 \Delta v c \nu^2}, \quad (3.13)$$

and that is the minimum  $T_{\text{R}}$  that can be measured for each galaxy at the given line width.

- $T_{\text{ex}}^{\text{max}} > T_{\text{ex}}^{1 \rightarrow 0} > \frac{E_1}{k_B}$ .  
Although unusual, the CO emission can be optically thin under conditions such as highly turbulent gas motions or otherwise large velocity dispersions (for example stellar outflows and perhaps also galaxy winds) [Bolatto et al., 2013]. For an optically thin medium, under the assumption of LTE and  $T_{\text{ex}} \gg T_{\text{cmb}}$  we get from [Dasyra et al., 2016] that

$$\frac{F_{21}}{F_{10}} = \left( \frac{\nu_{21}}{\nu_{10}} \right)^4 e^{-2 \frac{h \nu_{10}}{k_B T_{\text{ex}}}}, \quad (3.14)$$

<sup>5</sup> $\alpha$  is in arcseconds.

where  $F_{10}$ ,  $\nu_{10}$  are the CO ( $1 \rightarrow 0$ ) line transition flux and frequency and  $F_{21}$ ,  $\nu_{21}$  are the CO ( $2 \rightarrow 1$ ) line transition flux and frequency respectively. Solving for  $T_{\text{ex}} \equiv \frac{E_1}{k_B}$ , we find it to be equal to  $\approx 5.53$  K, regardless of optical depth. A general proof of eq. 3.14 is laid out below. We start with the following equations:

- $E_J$  is the energy of level J (upper level used in this convention) and is described by eq. 3.15:

$$E_J = \frac{J(J+1)}{2} h\nu_{10}, \quad (3.15)$$

where  $\nu_{10}$  is the frequency of the CO ( $1 \rightarrow 0$ ) line transition in GHz.

- $W(\text{CO})$  is the integrated line intensity, given in traditional radio astronomy observational units of  $\text{K km s}^{-1}$  [Bolatto et al., 2013]:

$$W(\text{CO}) = T_J \Delta v = \frac{8\pi^3 \nu_J}{3k_B} \mu^2 \frac{J}{g_J} f_{\text{cmb}} N_J. \quad (3.16)$$

J is again the upper energy level,  $\nu_J$  the frequency for the transition to this energy level from the previous one,  $\mu$  is the chemical potential,  $g_J$  the statistical weight of the J energy level,  $N_J$  is the occupation number of the J energy level and  $f_{\text{cmb}} = 1 - \frac{\exp(\frac{h\nu}{kT_{\text{ex}}})^{-1}}{\exp(\frac{h\nu}{kT_{\text{cmb}}})^{-1}}$ , which is  $\sim 1$  for  $T_{\text{ex}} \gg T_{\text{cmb}}$ .

- $N(\text{H}_2)$  is the column density of the  $\text{H}_2$  molecule:

$$N(\text{H}_2) = \frac{1}{Z_{\text{CO}}} \frac{N_J z(T_{\text{ex}})}{g_J} \exp\left(\frac{E_J}{k_B T_{\text{ex}}}\right) \quad (3.17)$$

Here  $Z_{\text{CO}}$  is the abundance of the CO molecule and  $z$  is the partition function.

Solving eq. 3.17 for  $N_J$  and plugging it into eq. 3.16 yields:

$$W(\text{CO}) = T_J \Delta v = \frac{8\pi^3 \nu_J}{3k_B} \mu^2 \frac{J}{g_J} f_{\text{cmb}} \left[ \frac{Z_{\text{CO}} N(\text{H}_2) g_J}{z(T_{\text{ex}})} \exp\left(-\frac{E_J}{k_B T_{\text{ex}}}\right) \right]. \quad (3.18)$$

The flux of the energy level J (e.g. for the CO ( $1 \rightarrow 0$ ) line transition, J corresponds to 1, which is the upper energy level) is given by relation 3.19:

$$F_J = \nu_J^2 T_J \Delta v, \quad (3.19)$$

but since  $W(\text{CO}) = T_J \Delta v$  we can plug eq. 3.16 into eq. 3.19. If we then take the ratio of the flux of the J energy level, over the J-1 energy level, most terms cancel out and taking into account eq. 3.15, we end up with:

$$\frac{F_{J_2}}{F_{J_1}} = \frac{J_2}{J_1} \left( \frac{\nu_2}{\nu_1} \right)^3 \exp \left[ - \left( \frac{J_2(J_2 + 1)}{2} - \frac{J_1(J_1 + 1)}{2} \right) \frac{h\nu_{10}}{k_B T_{\text{ex}}} \right], \quad (3.20)$$

where we symbolized J with  $J_2$  and J-1 with  $J_1$ . For  $J=1$  this yields

$$\frac{F_{21}}{F_{10}} = 2 \left( \frac{\nu_{21}}{\nu_{10}} \right)^3 e^{-2 \frac{h\nu_{10}}{k_B T_{\text{ex}}}} \quad (3.21)$$

and since  $\left( \frac{\nu_{21}}{\nu_{10}} \right) = 2$ , we arrive at eq. 3.14. For an upper limit of the  $T_{\text{ex}}$  we plot the different flux ratios as a function of the  $T_{\text{ex}}$ . This is shown in figs. 3.1, 3.2 and 3.3. We can observe that all of them plateau at  $\sim 300$  K, which serves as an upper limit for the  $T_{\text{ex}}$ , which we take into account when examining the  $T_{\text{ex}}$  maps created later on.

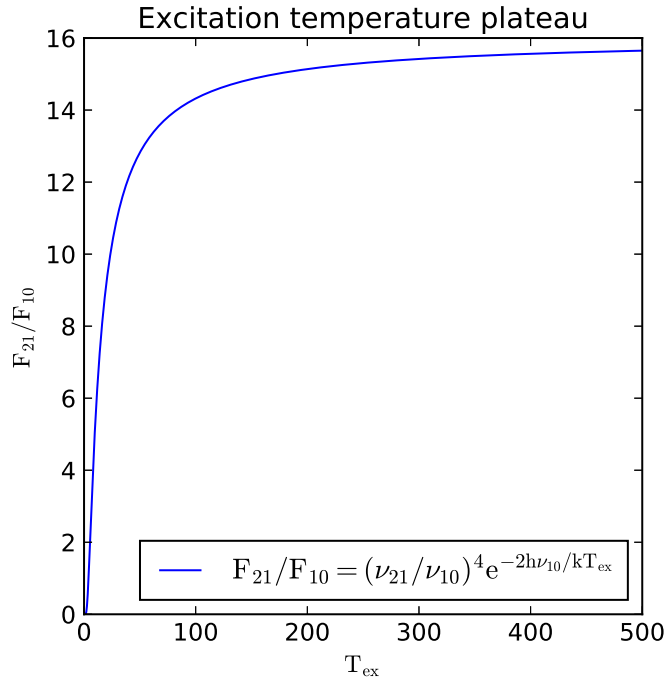


Figure 3.1: CO ( $2 \rightarrow 1$ ) over CO ( $1 \rightarrow 0$ ) transition line flux ratios.

For completion, we also describe below some of the trials and methods that we did not end up using. Instead of  $N_{\text{CO}}$  following the distribution of the CO ( $1 \rightarrow 0$ ) line transition, we tried to implement a similar restriction for spatially neighbouring pixels for  $N_{\text{CO}}$  as we did with  $n_{\text{H}_2}$ . But this led to flat maps and even failed maps, where no solution was found for a majority of the pixels. Another trial was to assign to the beam filling factor a map with the same distribution as the CO ( $1 \rightarrow 0$ ) line transition. The reasoning behind that was to allow the beam filling factor to "absorb" the flux variations, allowing the other parameters more freedom and breaking the degeneration between  $N_{\text{CO}}$  and the beam filling factor.

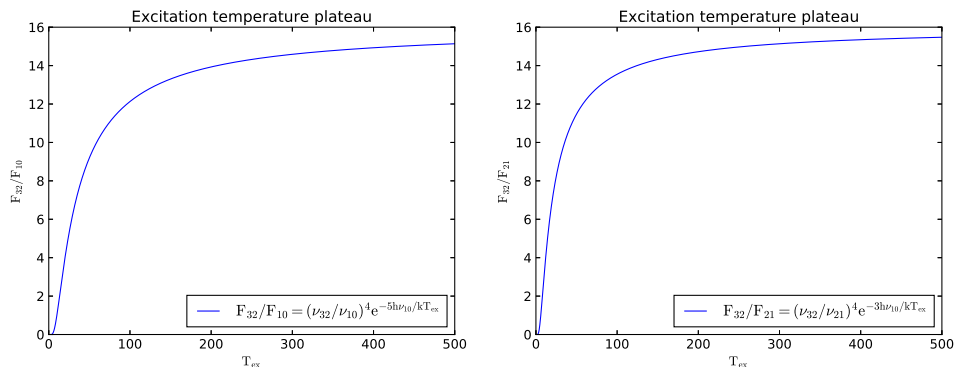


Figure 3.2: CO (3 → 2) over CO (1 → 0) and CO (2 → 1) transition line flux ratios.

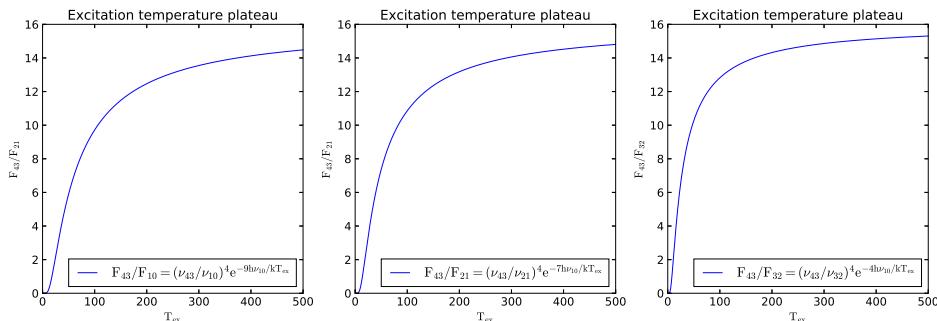


Figure 3.3: CO (4 → 3) over CO (1 → 0), CO (2 → 1) and CO (3 → 2) transition line flux ratios.

An additional attempt was to assign a different beam filling factor corresponding to each line transition. This resulted in flat maps and was therefore discarded. Hence we returned to constraining the  $N_{\text{CO}}$ .

Another method of minimisation we tried, was the Python package *lmfit*. It provides a high-level interface to non-linear optimization and curve fitting problems. The main objective was to try and better fit eq. 3.12. However, using a least squares method did not yield any result since there is always one extra unknown for each set of equation. As in, for  $n$  line transitions available, there are  $n$  equations to solve but  $n + 1$  unknowns. Thus we also tried the Nelder-Mead method, which does not require the unknowns to be as many as the equations. This yielded solutions to the equations but since they are so degenerate, they were very sensitive to even small changes in the beam filling factor and could therefore not be trusted.

### 3.4 Parameter selection

The final step was to define a procedure to select the parameter set used to create the maps of the galaxies. We started off with the grid mentioned above and let the beam filling factor loop over 4 orders of magnitude, namely beam filling factor  $\in [10^{-5}, 10^0]$ , with 10 steps for each order of magnitude. This gave us a general idea of the actual size of the grid needed for each galaxy. We did this to

save time, as maps created with larger grids with multiple beam filling factors as input take days to complete. Then we created a finer grid. This time the  $T_{\text{kin}} \in [5, 220]$  K, with a step of 1 K, the  $n_{\text{H}_2} \in [10^3, 10^7]$   $\text{cm}^{-3}$ , with 100 logarithmic number density points for each order of magnitude and  $N_{\text{CO}} \in [10^{13}, 10^{19}]$   $\text{cm}^{-2}$ , with 100 logarithmic column density points for each order of magnitude as well. Afterwards we created histograms for the maximum, median and minimum flux pixel for  $T_{\text{kin}}$ ,  $n_{\text{H}_2}$ ,  $N_{\text{CO}}$  and the beam filling factor (fig. 3.4), as well as the Spectral Line Energy Distributions (SLEDs), shown again in fig. 3.4. For each of the three pixels in question our minimisation script finds multiple solutions<sup>6</sup>, which are sorted in an ascending form for the  $\chi^2$  variable. The best fit for each pixel corresponds to the lowest  $\chi^2$ . The cutoff was  $5\sigma$ , as mentioned in sec. 3.3. Then we summed all solution parameter sets of  $T_{\text{kin}}$ ,  $n_{\text{H}_2}$ ,  $N_{\text{CO}}$  and beam filling factors to create the histograms and find the most frequent values.

We only considered beam filling factors that provided solutions for all 3 pixels, meaning that they produced solutions for the whole galaxy. For example in fig. 3.4, there are solutions for all pixels for a beam filling factor  $\in [5, 6, 7] \times 10^{-3}$ . This provided a general idea of the order of magnitude for the beam filling factor. Our final step was to create a histogram displaying the frequency of all beam filling factors. Having all of the above in mind we then used the nearest to half a magnitude beam filling factor, which in the case of our example is 0.01. The SLEDs, on the other hand, provide a good measure of how well the pixels are fitted. They also indicate if the grid has correct boundaries, or if it needs to be expanded or reduced.

A final step we implemented was to check if the scaling of the  $N_{\text{CO}}$  in relation to the beam filling factor was correct. Specifically, after having created the histograms for the  $N_{\text{CO}}$ , we binned the data for the maximum, median and minimum pixel and counted in which interval there were the most solutions. If the resulting  $N_{\text{CO}}$  interval was different from the one found in the initial map, we ran the maps again for the new  $N_{\text{CO}}$  interval, to check if the new interval was permissible. If it was, we kept the  $N_{\text{CO}}$  interval with the highest number of solutions for all 3 pixels. This was done to break potential degeneracies.

---

<sup>6</sup>We minimised eq. 3.12. The left hand side is the measured flux, the right hand side is the theoretical fit. By looping over the grid, we find the best solution for the  $T_{\text{RS}}$  for a given beam filling factor.



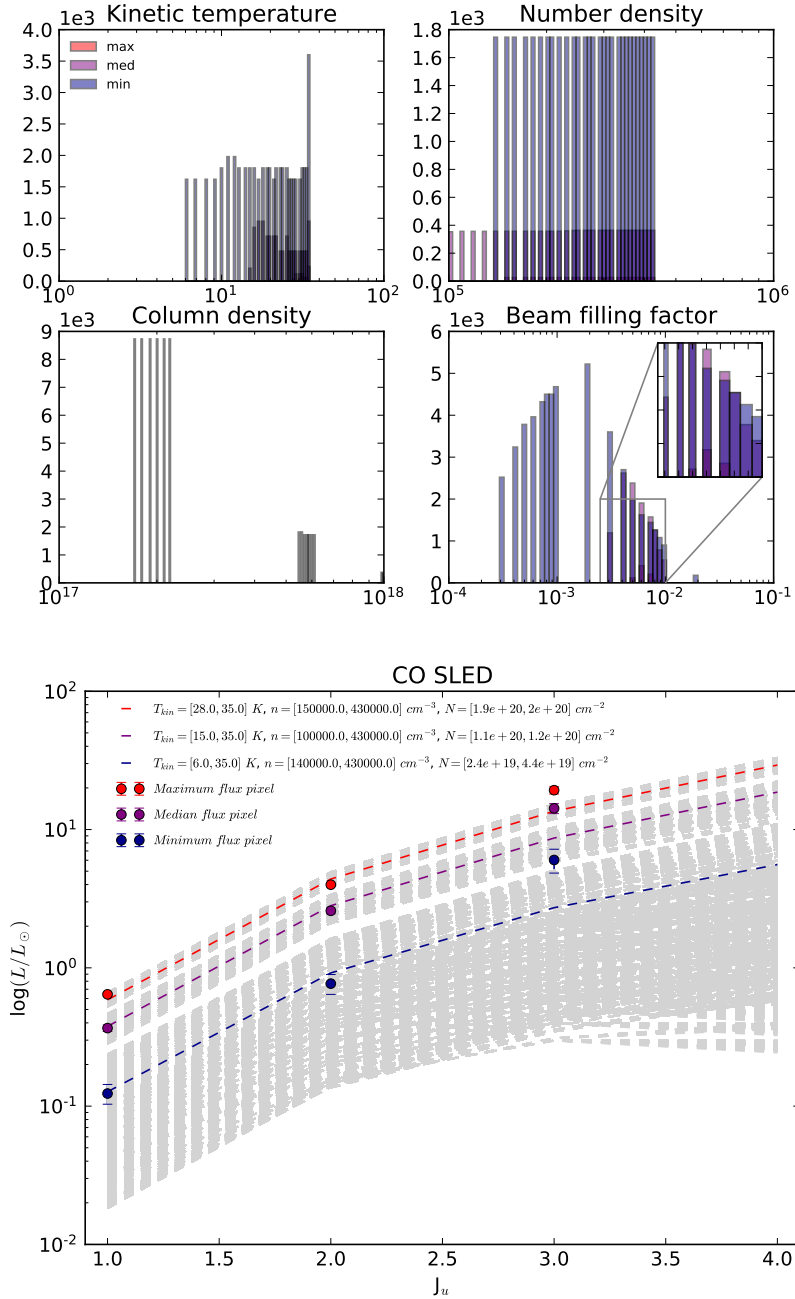


Figure 3.4: *Top:* Histograms for OQ 208. *Bottom:* SLEDs for OQ 208.

# Chapter 4

## Results

### 4.1 OQ 208

#### 4.1.1 Image creation / Code input

To create two dimensional images, we followed the procedure layed out in sec. 3.2. The interferometric data cubes we started with for OQ 208, were for CO (1  $\rightarrow$  0), CO (2  $\rightarrow$  1), and CO (3  $\rightarrow$  2) line transitions. We convolved the 3 data cubes into a common resolution, with a reference beam of the CO (3  $\rightarrow$  2) line transitions, since this line transition was observed by the SMA (largest beam size). We also regridded the images to the same spatial pixel size. A common test we performed to see if the procedure worked well, was to overlay the cubes with the continuum radiation and check if they are aligned.

In order to decide which velocity ranges to study, we looked at the data cubes using the MAPPING software. For OQ 208 specifically, we decided to use the whole extent of the galaxy, since we did not find any particular regions, with a clear-cut detection of a wind. Therefore, we used the following velocity ranges: 600 km s<sup>-1</sup> for CO (1  $\rightarrow$  0), 500 km s<sup>-1</sup> for CO (2  $\rightarrow$  1) and 600 km s<sup>-1</sup> for CO (3  $\rightarrow$  2) (fig. 4.1).

#### 4.1.2 Physical parameter maps

The first step for creating maps of the physical parameters was to find the beam filling factor, as described in sec. 3.4. Briefly stated, we started with a beam filling factor in the range [10<sup>-5</sup>, 10<sup>0</sup>] and created histograms for the physical parameters. We found a best fit for the beam filling factor of  $\sim 0.007$ , which we rounded to 0.01. The N<sub>CO</sub> interval check did not yield another possible solution, thus we kept the initial maps. In order to try and get a fit of 3  $\sigma$  for the  $\chi^2$  parameter, we compared the measured continua to the bibliography in NED. The comparison is shown in fig. 4.2. As can be seen, we found a difference of a factor of  $\sim 1.2$  between our measurement and the bibliography. Our next step was to check if the calibrator used, in our case a star, was variable in the relevant wavelengths. If it was not, then we could justify multiplying the CO (1  $\rightarrow$  0) line with the aforementioned factor<sup>1</sup>,

---

<sup>1</sup>The other 2 CO transition lines were close enough to the bibliographic ones, so there was no room for a correction.

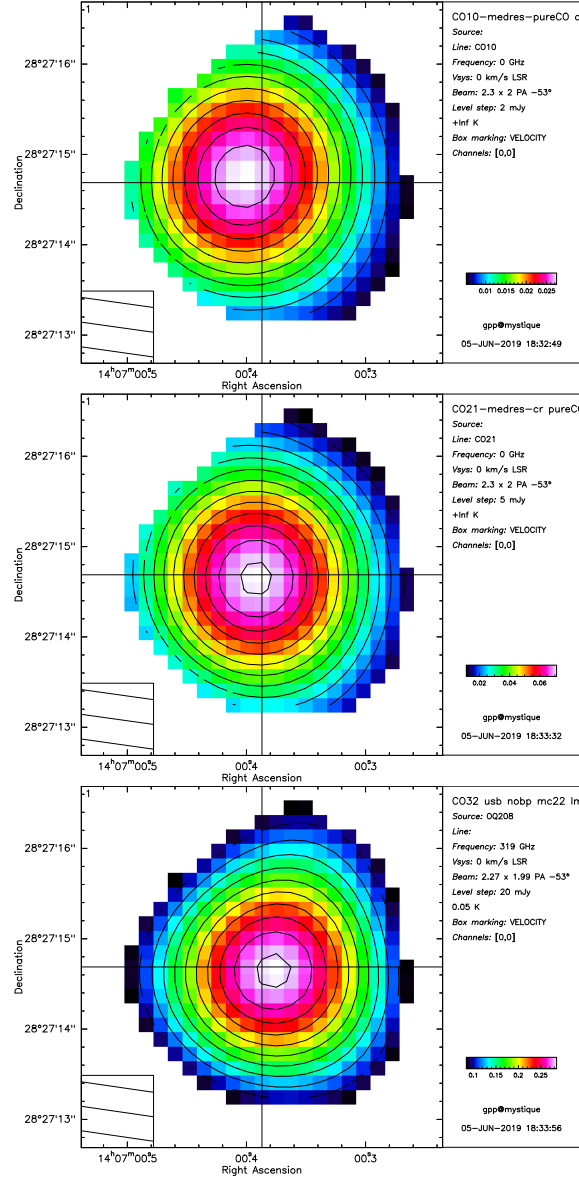


Figure 4.1: Velocity ranges for the 3 available CO transition lines for OQ 208.

to compensate for the loss in flux. The flux as a function of the frequency is shown in fig. 4.3. Indeed MWC 349 does not vary much in the mm and radio frequencies. We therefore tried creating maps with this fixed data cube for the CO (1  $\rightarrow$  0) line transition but we did not succeed in finding a common beam filling factor satisfying all pixels, no matter the tweaks and the grid limits. Thus we reverted back to the original data cubes and proceeded with the fitting process with a  $5\sigma$  error tolerance for the  $\chi^2$  parameter. The resulting maps are depicted in fig. 4.4.

Starting with the  $T_{\text{kin}}$ , we detect a maximum of  $\sim 20$  K at the nucleus. This is to be expected for a gas rich galaxy but not particularly indicative of jet activity. The  $n_{\text{H}_2}$  appears overall flat, at  $10^5 \text{ cm}^{-3}$ . The  $N_{\text{CO}}$  follows the flux distribution of the CO (1  $\rightarrow$  0) line transition as required, with a value of  $\sim 5 \times 10^{20} \text{ cm}^{-2}$  at the nucleus.

We can compare the  $T_{\text{kin}}$  graph to the  $T_{\text{ex}}$  graphs in fig. 4.5. Both reach a high

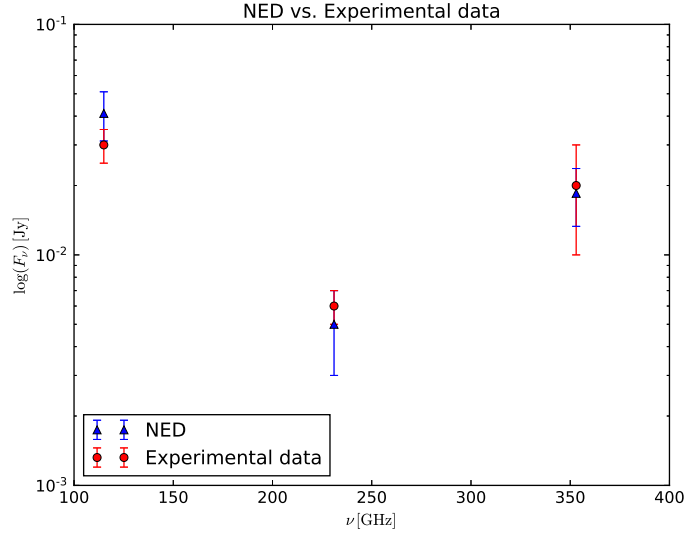


Figure 4.2: Continuum at the CO ( $1 \rightarrow 0$ ), CO ( $2 \rightarrow 1$ ) and CO ( $3 \rightarrow 2$ ) transition lines for OQ 208.

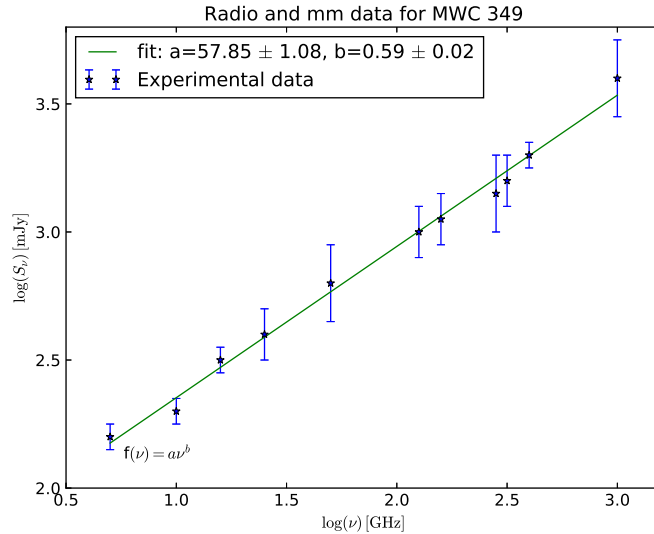


Figure 4.3: Fit for the primary calibrator MWC 349 used for OQ 208 for the CO ( $1 \rightarrow 0$ ) and CO ( $2 \rightarrow 1$ ) line transitions.

of  $\sim 20$  K at the nucleus, with a gradient of  $\sim 10$  K as we move towards the outside regions, which is rather typical for a spiral galaxy. Since all 4 graphs are similar, we can conclude that the system is overall in LTE.

Apart from these two dimensional maps, we wanted to additionally compare the excited gas of the central region, to that of the ambient ISM found in a spiral arm. We thus used the measurements for the integrated central region, which were presented in my Bachelor Thesis and refitted them, using the added conditions described before. The spiral arm in question, found in a velocity range of  $[0, 350]$   $\text{km s}^{-1}$  north of the nucleus, was also first presented in my Bachelor The-

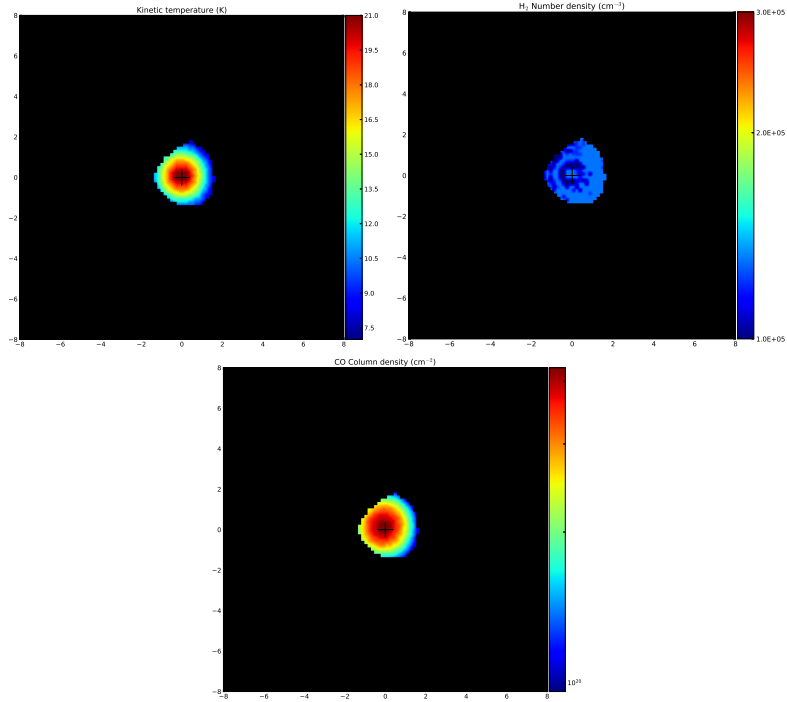


Figure 4.4: *Left to right*:  $T_{\text{kin}}$ ,  $n_{\text{H}_2}$  and  $N_{\text{CO}}$  graphs for OQ 208.

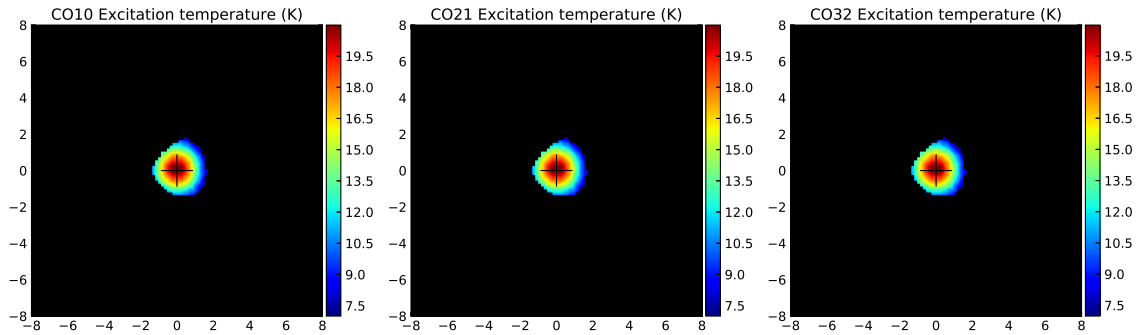


Figure 4.5: *Left to right*:  $T_{\text{ex}}$  graphs for the CO ( $1 \rightarrow 0$ ) through CO ( $3 \rightarrow 2$ ) line transitions.

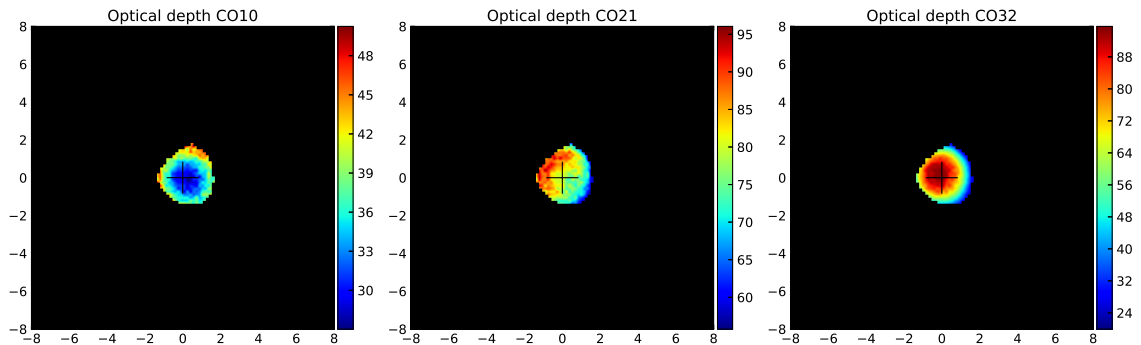


Figure 4.6: *Left to right*: Optical depth graphs for the CO ( $1 \rightarrow 0$ ) through CO ( $3 \rightarrow 2$ ) line transitions.

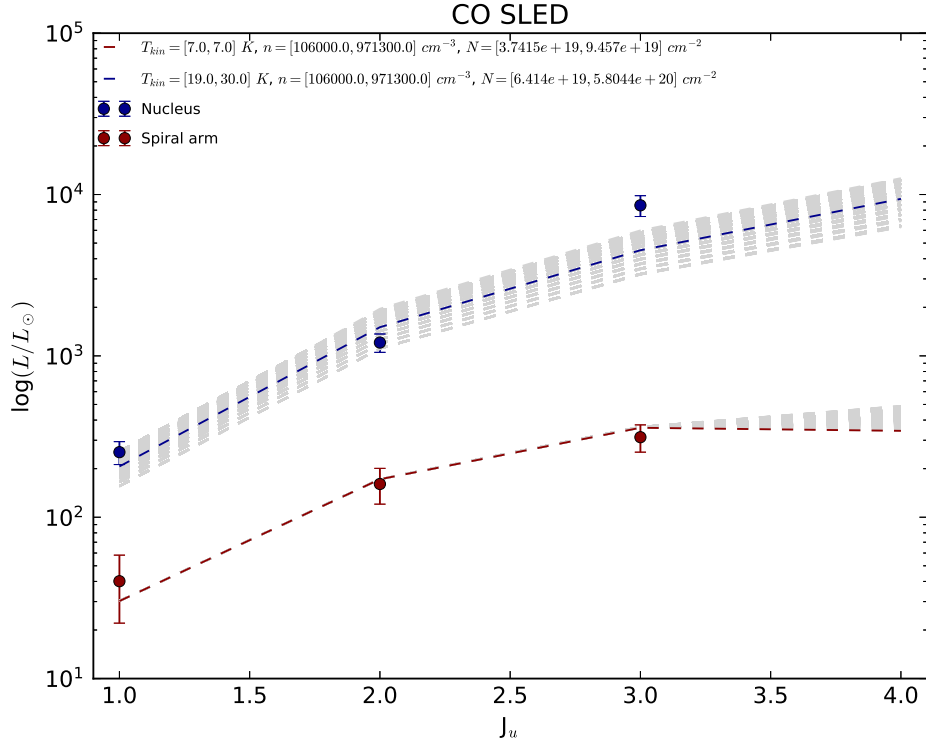


Figure 4.7: Comparison of the integrated SLEDs of the nucleus and spiral arm for galaxy OQ 208.

sis but was fitted only for the first two CO transition lines. We can see in fig. 4.7 that the excitation is higher in the central region, with a preferred  $T_{\text{kin}}$  of  $\approx 25$  K, whereas the kinetic temperature in the spiral arm reaches 7 K. This also affects the mass content, expressed through the  $\alpha_{\text{CO}}$  conversion factor, which will be explored later on. Based on the analysis by [Bolatto et al., 2013], as well as the proof presented in my Bachelor Thesis, we use the  $\alpha_{\text{CO}}$  conversion factor defined as  $2 \times 10^{-21} X_{\text{CO}} \left(\frac{\text{cm}}{\text{pc}}\right)^2 M_{\odot}$ , with  $X_{\text{CO}} \equiv \frac{N(\text{H}_2)}{W(\text{CO})}$ . A typical value for  $\alpha_{\text{CO}}$  is  $4.3 M_{\odot} (\text{K km s}^{-1} \text{ pc}^2)^{-1}$  for the disks of normal, solar metallicity galaxies [Bolatto et al., 2013]. For optically thick media  $X_{\text{CO}} \sim n_{\text{H}_2}^{0.5} (f T_{\text{kin}})^{-1.2}$ , while for optically thin media  $X_{\text{CO}} \approx 1.6 \times 10^{19} \frac{T_{\text{ex}}}{30\text{K}} e^{\frac{5.53\text{K}}{T_{\text{ex}}}} - 0.184 \text{ cm}^{-2} (\text{K km s}^{-1})^{-1}$  [Bolatto et al., 2013], [Bolatto, 2015], [Dickman et al., 1986].

## 4.2 4C 12.50

### 4.2.1 Image creation / Code input

For this galaxy we had the CO (1  $\rightarrow$  0), CO (3  $\rightarrow$  2) and CO (4  $\rightarrow$  3) line transition data cubes available. We chose to study the galaxy in 3 symmetrical velocity ranges, namely  $\Delta v \in [-300, -100] \text{ km s}^{-1}$ ,  $[-100, 100] \text{ km s}^{-1}$  and  $[100, 300] \text{ km s}^{-1}$ , as seen in figs. 4.8, 4.9 and 4.10.

<sup>2</sup> $f$  is the beam filling factor

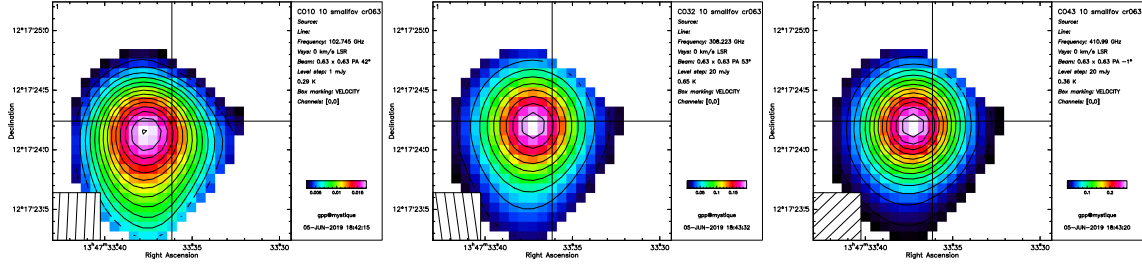


Figure 4.8:  $\Delta v \in [-300, -100] \text{ km s}^{-1}$  for 4C 12.50, for the CO ( $1 \rightarrow 0$ ), CO ( $2 \rightarrow 1$ ) and CO ( $4 \rightarrow 3$ ) line transitions.

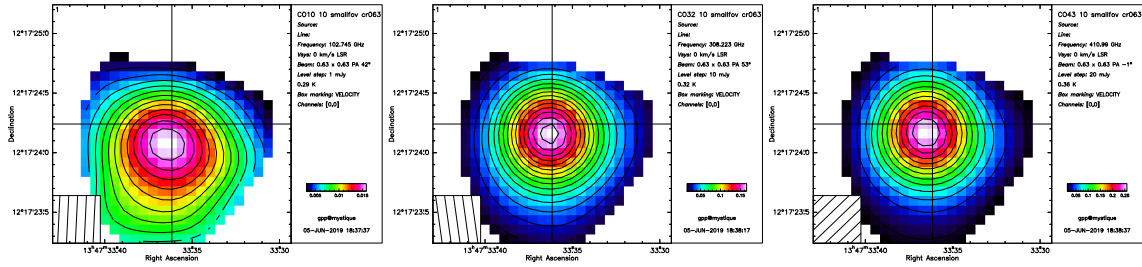


Figure 4.9:  $\Delta v \in [-100, 100] \text{ km s}^{-1}$  for 4C 12.50, for the CO ( $1 \rightarrow 0$ ), CO ( $2 \rightarrow 1$ ) and CO ( $4 \rightarrow 3$ ) line transitions.

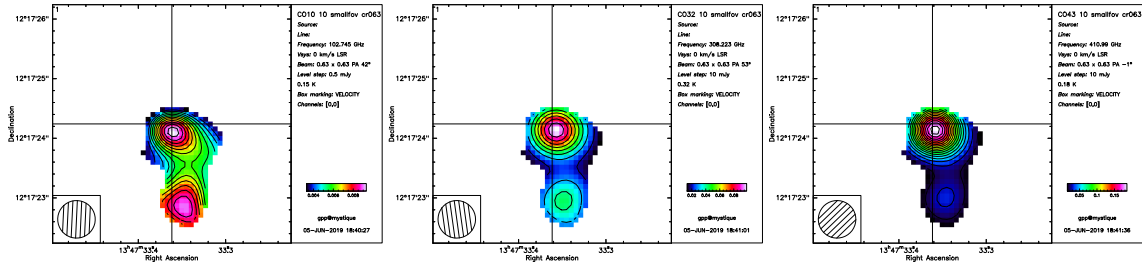


Figure 4.10:  $\Delta v \in [100, 300] \text{ km s}^{-1}$  for 4C 12.50, for the CO ( $1 \rightarrow 0$ ), CO ( $2 \rightarrow 1$ ) and CO ( $4 \rightarrow 3$ ) line transitions.

## 4.2.2 Physical parameter maps

The 3 symmetric velocity ranges correspond to the blueshifted side of the disk at a  $\Delta v$  of  $[-300, -100] \text{ km s}^{-1}$ , the central part of the disk representing the nucleus at a  $\Delta v$  of  $[-100, 100] \text{ km s}^{-1}$  and the redshifted side of the disk at a  $\Delta v$  of  $[100, 300] \text{ km s}^{-1}$ . Our aim was to compare the gas excitation in those regions. Following again the procedure mapped out in sec. 3.4 we created histograms for the beam filling factors in a range of  $[10^{-5}, 10^0]$  for each  $\Delta v$  and found that the most likely values for them would be either 0.01 or 0.05. For those values of the beam filling factor we created individual maps and found that in order to get a solution for all pixels, in all velocity ranges, the right beam filling factor would be 0.05. This time, our  $N_{\text{CO}}$  interval check did indeed indicate other possible  $N_{\text{CO}}$  intervals, for the  $[100, 300] \text{ km s}^{-1}$  velocity range. However, since we were studying velocity ranges of the same width, the beam filling factor needed to be the same for all 3. This added restriction of the beam filling factor being equal to 0.05 meant that we did not find another physically satisfactory solution for this velocity range other than the initial

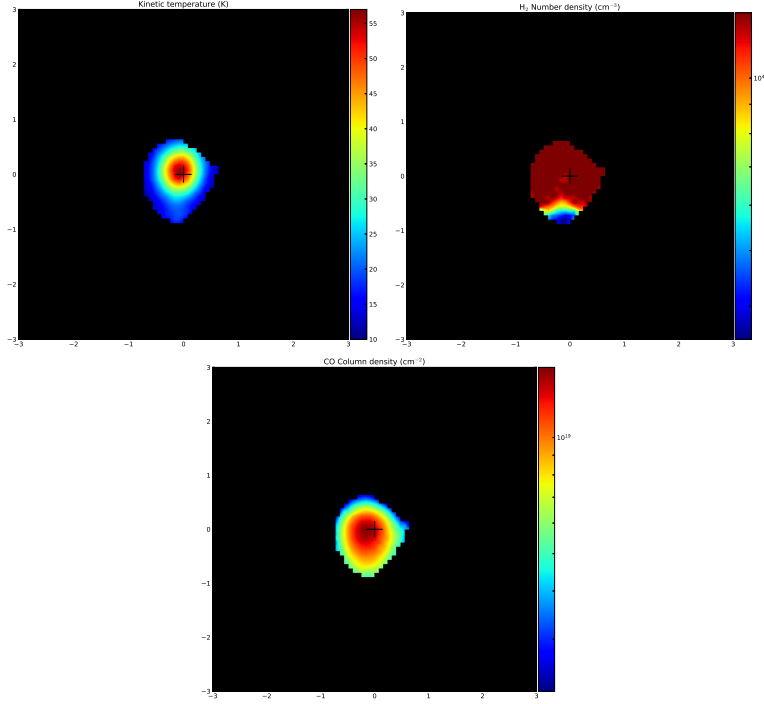


Figure 4.11: *Left to right*:  $T_{\text{kin}}$ ,  $n_{\text{H}_2}$  and  $N_{\text{CO}}$  graphs for  $\Delta v = [-300, -100]$  km s $^{-1}$ .

one. Thus we created the following maps:

#### $\Delta v$ of $[-300, -100]$ km s $^{-1}$

Looking at the blueshifted side of the nucleus, we created the 4 maps shown in fig. 4.11, which depict the  $T_{\text{kin}}$ ,  $n_{\text{H}_2}$  and  $N_{\text{CO}}$ . Starting at the  $T_{\text{kin}}$  graph, we detect a high of 55 K at the nucleus. The  $n_{\text{H}_2}$  appears rather flat, around  $10^4$  cm $^{-3}$ , except at the lower part, where it reaches values as low as  $5 \times 10^3$  cm $^{-3}$ . As previously mentioned, we required the  $N_{\text{CO}}$  to follow the flux distribution of the CO ( $1 \rightarrow 0$ ) line transition. It reaches a high of  $10^{19}$  cm $^{-2}$  at the nucleus and falls off towards the edges to around  $5 \times 10^{18}$  cm $^{-2}$ . Fig. 4.12 displays the SLEDs for our three reference pixels along with their histograms. All three pixels exhibit SLEDs that are highly excited.

An interesting observation regarding this velocity range is its optical depth. It is depicted in fig. 4.13. In the central region of the CO ( $1 \rightarrow 0$ ) line transition  $\tau < 1$ , making the gas optically thin. This alludes to the fact that there could potentially be an outflow due to possible jet activity in this region. This is corroborated by the high excitation temperature of  $\sim 70$  K in this region (fig. 4.14). While the CO ( $4 \rightarrow 3$ ) line transition also exhibits an optical depth below 1, the 14 pixels in question are only located around the edges of the image and is therefore most likely an artifact.

#### $\Delta v$ of $[-100, 100]$ km s $^{-1}$

Moving on to the central velocity range, as seen in fig. 4.15, we detect a  $T_{\text{kin}}$  with a maximum of 40 K, which is lower than the previous velocity range. The  $n_{\text{H}_2}$



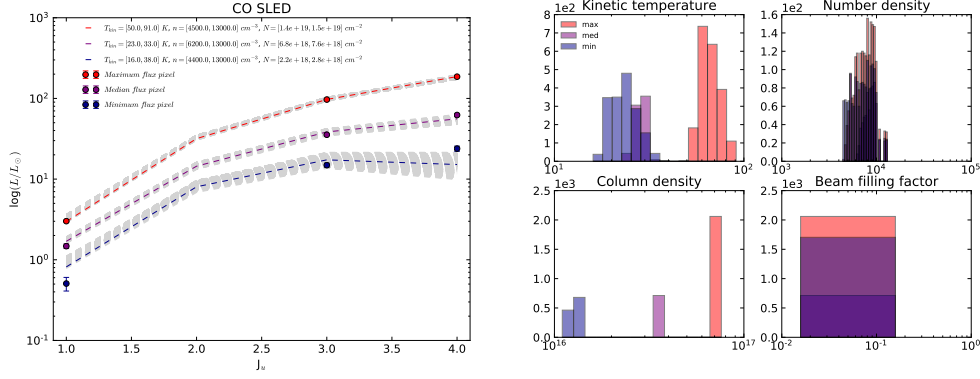


Figure 4.12: *Left to right*: SLEDs and histograms for  $\Delta v = [-300, -100]$  km s $^{-1}$  for the CO ( $1 \rightarrow 0$ ), CO ( $3 \rightarrow 2$ ) and CO ( $4 \rightarrow 3$ ) line transitions.

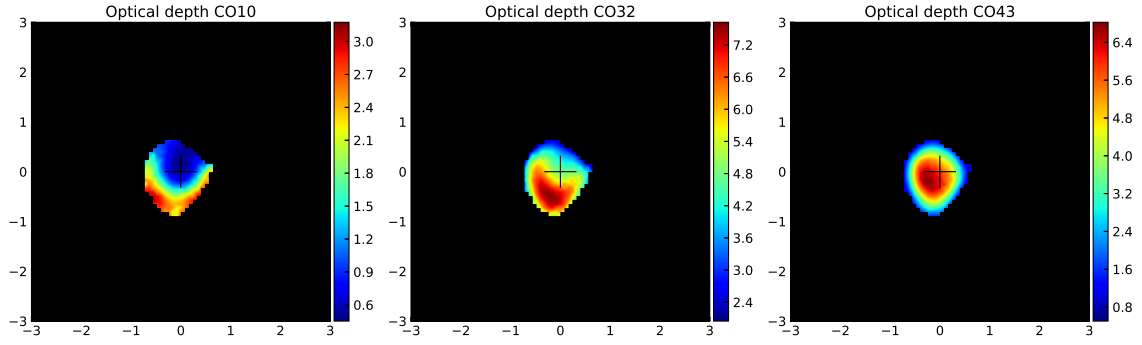


Figure 4.13: *Left to right*: Optical depth graphs for  $\Delta v = [-300, -100]$  km s $^{-1}$  for CO ( $1 \rightarrow 0$ ), CO ( $3 \rightarrow 2$ ) and CO ( $4 \rightarrow 3$ ) line transitions.

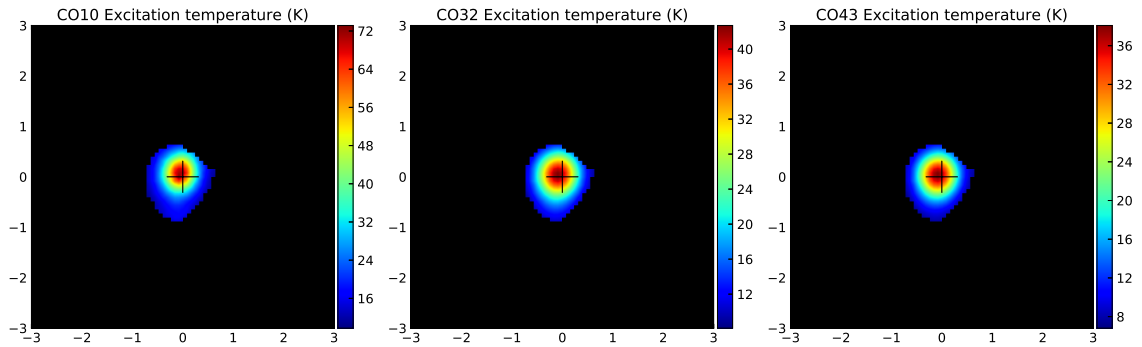


Figure 4.14: *Left to right*:  $T_{\text{ex}}$  graphs for  $\Delta v = [-300, -100]$  km s $^{-1}$  for the CO ( $1 \rightarrow 0$ ), CO ( $3 \rightarrow 2$ ) and CO ( $4 \rightarrow 3$ ) line transitions.

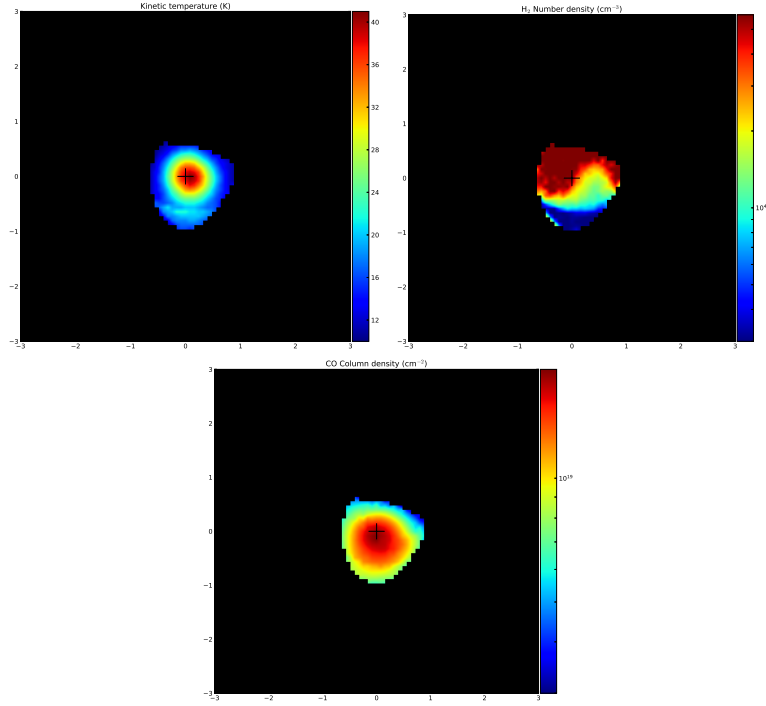


Figure 4.15: *Left to right:*  $T_{\text{kin}}$ ,  $n_{\text{H}_2}$  and  $N_{\text{CO}}$  graphs for  $\Delta v = [-100, 100] \text{ km s}^{-1}$ .

on the other hand rises to  $5 \times 10^4 \text{ cm}^{-3}$  and spans over a whole order of magnitude, as its low is  $5 \times 10^3 \text{ cm}^{-3}$ . This is in contrast with the  $[-300, -100] \text{ km s}^{-1}$  velocity range, where the  $n_{\text{H}_2}$  was rather constant. The  $N_{\text{CO}}$  exhibits the same behaviour, as in the aforementioned velocity range. This region also appears to be in LTE, at least for the first CO line transition, as shown in fig. 4.16. Finally, by examining the optical depth in fig. 4.17, we can detect that it gets low, to around 1.5 around the central region, but does not fall beneath the threshold of 1. The SLEDs in fig. 4.18 indicate higher excitation for the maximum temperature pixels, whereas the lower temperature pixel appears sub-excited.

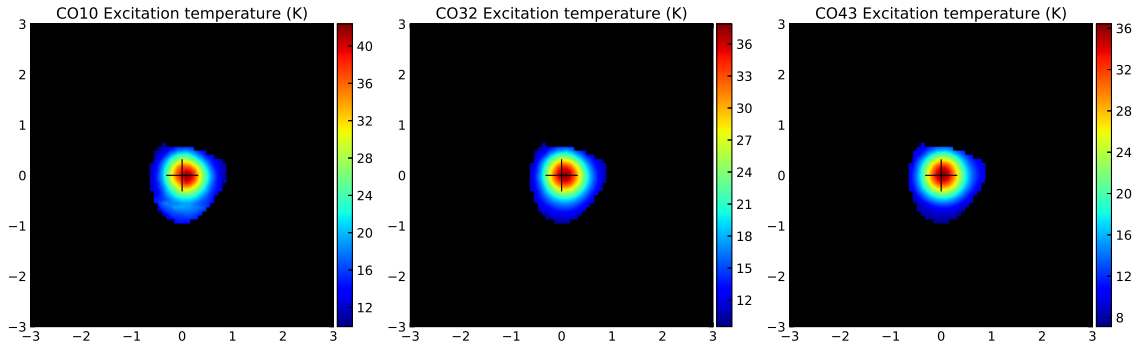


Figure 4.16: *Left to right:*  $T_{\text{ex}}$  graphs for  $\Delta v = [-100, 100] \text{ km s}^{-1}$  for the CO ( $1 \rightarrow 0$ ), CO ( $3 \rightarrow 2$ ) and CO ( $4 \rightarrow 3$ ) line transitions.

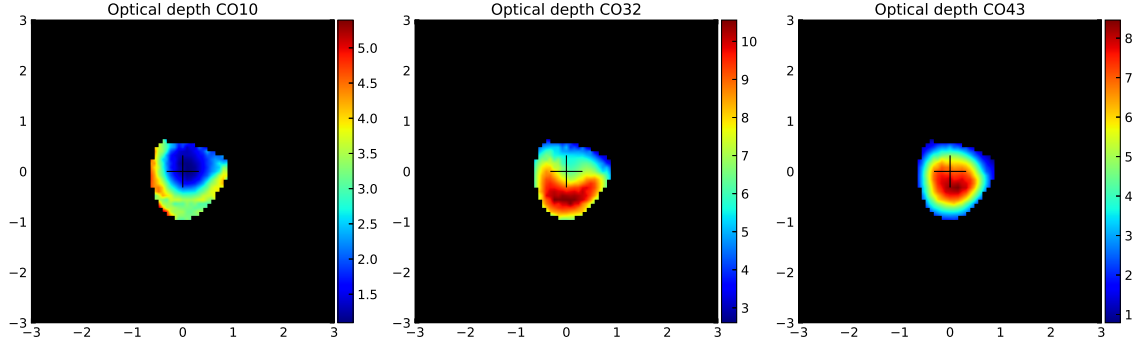


Figure 4.17: *Left to right*: Optical depth graphs for  $\Delta v = [-100, 100]$  km s $^{-1}$  for the CO (1  $\rightarrow$  0), CO (3  $\rightarrow$  2) and CO (4  $\rightarrow$  3) line transitions.

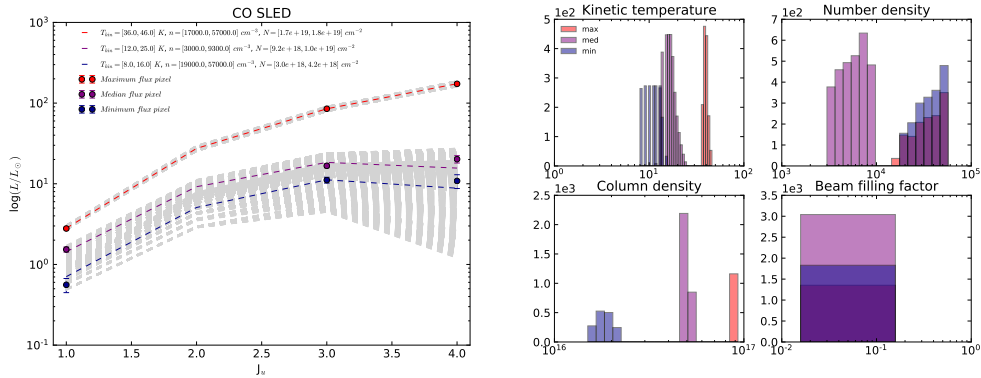


Figure 4.18: *Left to right*: SLEDs and histograms for  $\Delta v = [-100, 100]$  km s $^{-1}$ .

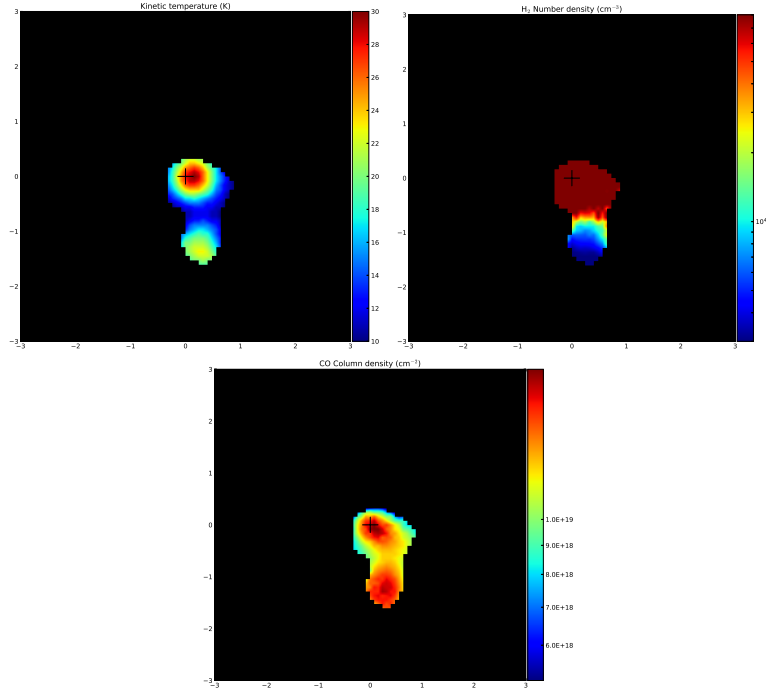


Figure 4.19: *Left to right*:  $T_{\text{kin}}$ ,  $n_{\text{H}_2}$  and  $N_{\text{CO}}$  graphs for  $\Delta v = [100, 300] \text{ km s}^{-1}$ .

### $\Delta v$ of $[100, 300] \text{ km s}^{-1}$

The redshifted side of the galaxy's disk, shown in fig. 4.19 is asymmetric compared to the other 2 velocity ranges. Its  $T_{\text{kin}}$  is also the lowest, at a high of  $\sim 30 \text{ K}$ . Thus we conclude that in the  $[-300, -100] \text{ km s}^{-1}$  velocity range, the gas is the most excited. Here the  $n_{\text{H}_2}$  spans over two orders of magnitude. The northern, dense part reaches  $\sim 8 \times 10^4 \text{ cm}^{-3}$ , exhibiting the highest density out of all the regions. The southern, less dense part reaches values as low as  $\sim 5 \times 10^3 \text{ cm}^{-3}$ . The  $N_{\text{CO}}$  again does not change over an order of magnitude. As with the central region, we detect the redshifted side to be in LTE, however, here for all 3 line transitions (fig. 4.20). The optical depth (fig. 4.21) falls to 1 in the high temperature regions for the CO ( $1 \rightarrow 0$ ) map, indicating that there could be some turbulence there, but it does not get quite as low as in the  $[-300, -100] \text{ km s}^{-1}$  velocity range. For completion, we also display the SLEDs and histograms in fig. 4.22.

Finally, we display the integrated SLEDs for all three velocity ranges in fig. 4.23.  $\Delta v = [-300, -100] \text{ km s}^{-1}$  is best fitted for  $T_{\text{kin}} \approx 60 \text{ K}$  ( $T_{\text{ex}}^{1 \rightarrow 0} \approx 60 \text{ K}$ ),  $\Delta v = [-100, 100] \text{ km s}^{-1}$  corresponds to  $T_{\text{kin}} \approx 45 \text{ K}$  ( $T_{\text{ex}}^{1 \rightarrow 0} \approx 40 \text{ K}$ ) and  $\Delta v = [100, 300] \text{ km s}^{-1}$  to  $T_{\text{kin}} \approx 30 \text{ K}$  ( $T_{\text{ex}}^{1 \rightarrow 0} \approx 29 \text{ K}$ ). We can deduce from this plot that  $[-300, -100] \text{ km s}^{-1}$  corresponds to the highest flux, while the  $[100, 300] \text{ km s}^{-1}$  velocity range is the most excited. There appears to be a degeneration between those 2 quantities but we can safely conclude that both solutions are acceptable.

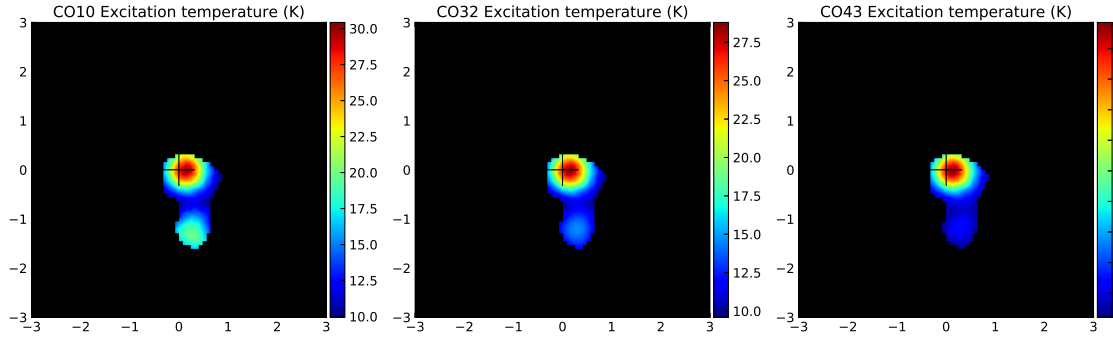


Figure 4.20: *Left to right*:  $T_{\text{ex}}$  graphs for  $\Delta v = [100, 300]$  km s $^{-1}$  for CO (1  $\rightarrow$  0), CO (3  $\rightarrow$  2) and CO (4  $\rightarrow$  3) line transitions.

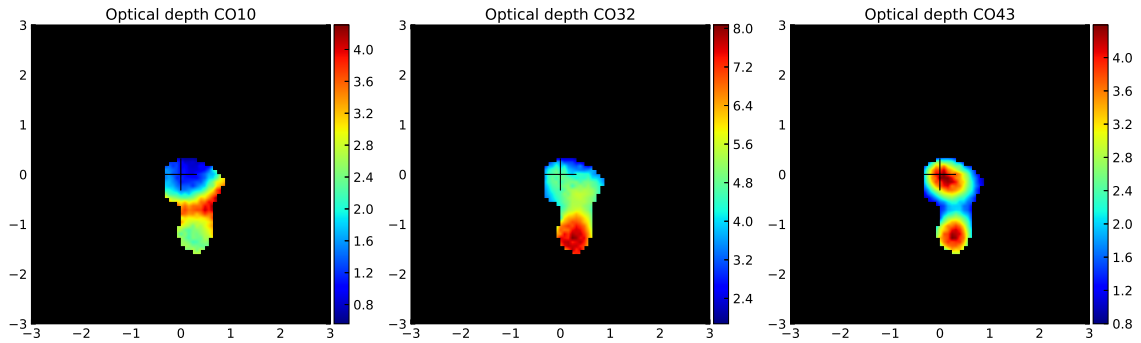


Figure 4.21: *Left to right*: Optical depth graphs for  $\Delta v = [100, 300]$  km s $^{-1}$  for the CO (1  $\rightarrow$  0), CO (3  $\rightarrow$  2) and CO (4  $\rightarrow$  3) line transitions.

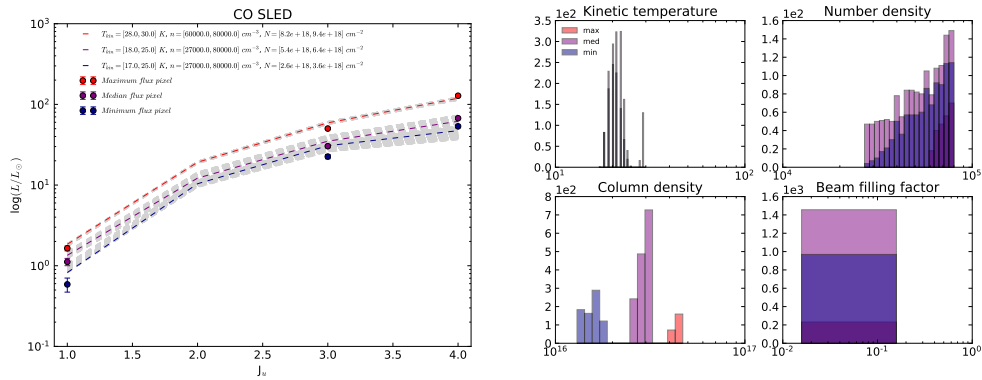


Figure 4.22: *Left to right*: SLEDs and histograms for  $\Delta v = [100, 300]$  km s $^{-1}$ .

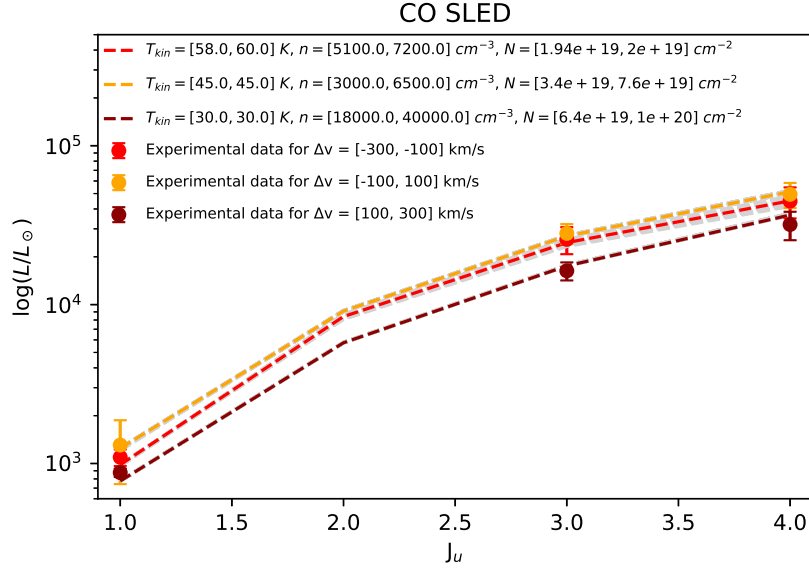


Figure 4.23: Comparison of the integrated SLEDs of the three velocity ranges for galaxy 4C 12.50.

## 4.3 IC 5063

### 4.3.1 Image creation / Code input

As with 4C 12.50, the data we had for IC 5063 were from ALMA. This time we had all the first 4 CO line transitions available as data cubes. We convolved again everything into a common resolution and regridded the data to obtain collapsed images of the same size. The velocity range we used was a  $\Delta v$  of  $[-200, 200]$  km s $^{-1}$ . This is shown in fig. 4.24. Apart from the main nucleus at the centre, two lobes to the northwest and southeast are also clearly visible. This refers to the whole of the galaxy.

Apart from the common mask applied to the four line transitions, we created a common spectroscopic mask for the first three and not for the fourth one. The reasoning behind this is that we did not detect gas for the CO (4  $\rightarrow$  3) line transition in the spiral arm extended to the northwest, which is detectable in the first three line transitions. Thus we applied this mask to the CO (4  $\rightarrow$  3) line transition as well, and filled out the gap that was formed with the one sigma flux of the collapsed data cube without the primary beam correction. This provides an upper limit for our maps and could also be used as a check for the map behaviour. They are depicted in fig. 4.25. The region outside the  $1\sigma$  contour of the CO (4  $\rightarrow$  3) line transition corresponds to the applied mask. For this galaxy we did not create one dimensional integrated fluxes SLEDs, since we studied the spiral arm in a two dimensional manner as well.

### 4.3.2 Physical parameter maps

For this galaxy we initially studied it using a velocity range of  $[-200, 200]$  km s $^{-1}$  as was layed out in sec. 3.4. This velocity range corresponds to the disk, which

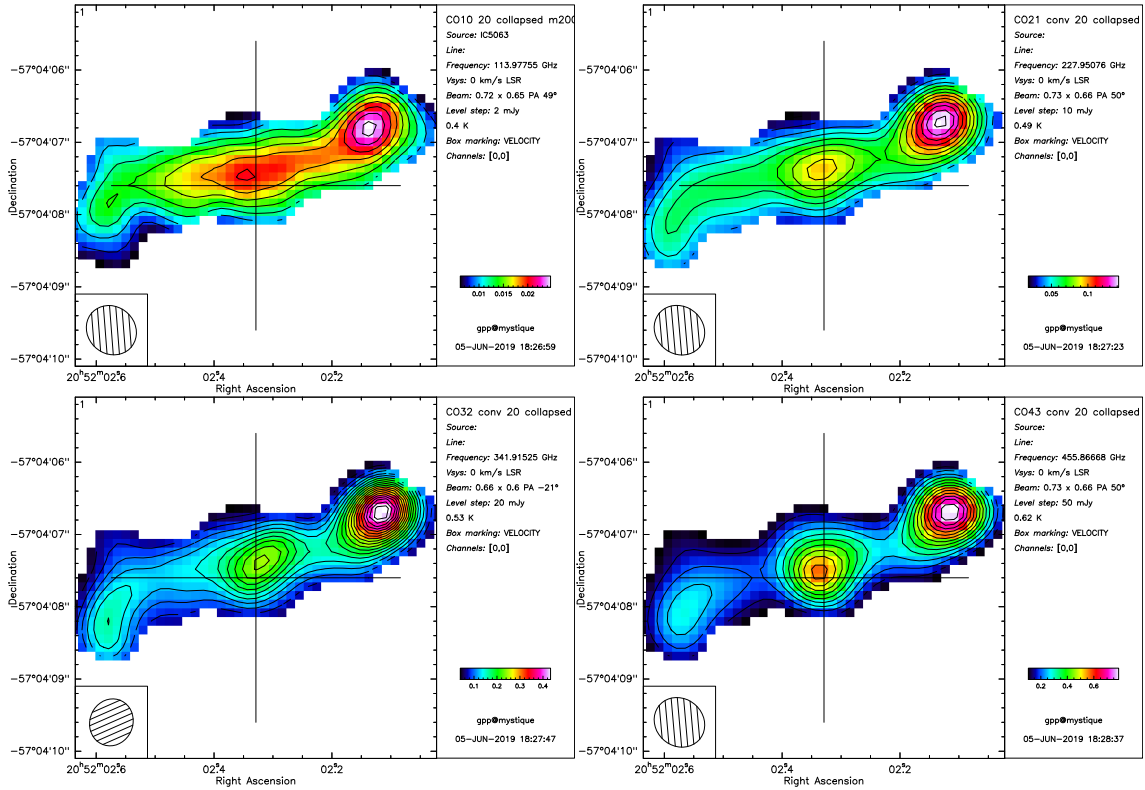


Figure 4.24:  $\Delta v \in [-200, 200] \text{ km s}^{-1}$  for IC 5063, for the CO ( $1 \rightarrow 0$ ), CO ( $2 \rightarrow 1$ ), CO ( $3 \rightarrow 2$ ) and CO ( $4 \rightarrow 3$ ) line transitions.

we aimed to study, along with the galactic wind that flows through it. We constrained the  $n_{\text{H}_2}$  of two neighbouring pixels to differ up to 10, instead of the usual 3. Additionally, for this galaxy we did not assume that the highest value for the  $n_{\text{H}_2}$  was in the nucleus, since we expected equally high values in the two radio lobes. By creating maps for unconstrained beam filling factors, we found that for values of 0.01 and 0.005, we could successfully fit all pixels<sup>3</sup>. Hence we needed to decide which of the two was the most likely one. We used the aforementioned method of checking if the  $N_{\text{CO}}$  is correctly scaled by studying the histograms of the maximum, median and minimum pixels. We found that most solutions lie within a range of  $[4, 10] \times 10^{16} \text{ cm}^{-2}$  for the  $N_{\text{CO}}$ . This corresponded to a beam filling factor of 0.01, as shown in fig. 4.26.

The maps we created are shown in fig. 4.27. Starting with the  $T_{\text{kin}}$  graph, one can immediately observe that the temperature reaches a high of over 150 K at the northwest lobe. This part of the galaxy is impacted by the jet. It is remarkable that the temperature is a whole order of magnitude higher than in the ambient ISM, where  $T_{\text{kin}} \approx 20 \text{ K}$ .

Moving on to the  $n_{\text{H}_2}$  graph we clearly see that it is the highest at the nucleus of the galaxy and in the southeast lobe ( $n_{\text{H}_2} \sim 5 \times 10^5 \text{ cm}^{-3}$ ). In the jet impacted northwest lobe however it is  $\sim 4$  times lower than its surrounding regions. This is

<sup>3</sup>Instead of the usual  $5\sigma$  upper limit for the  $\chi^2$  minimisation, we resorted to implementing a  $6\sigma$  upper limit for this galaxy. The reason for this were 6 pixels, for which the given restrictions only produced fitting curves for  $\chi^2$  values a little over 100.

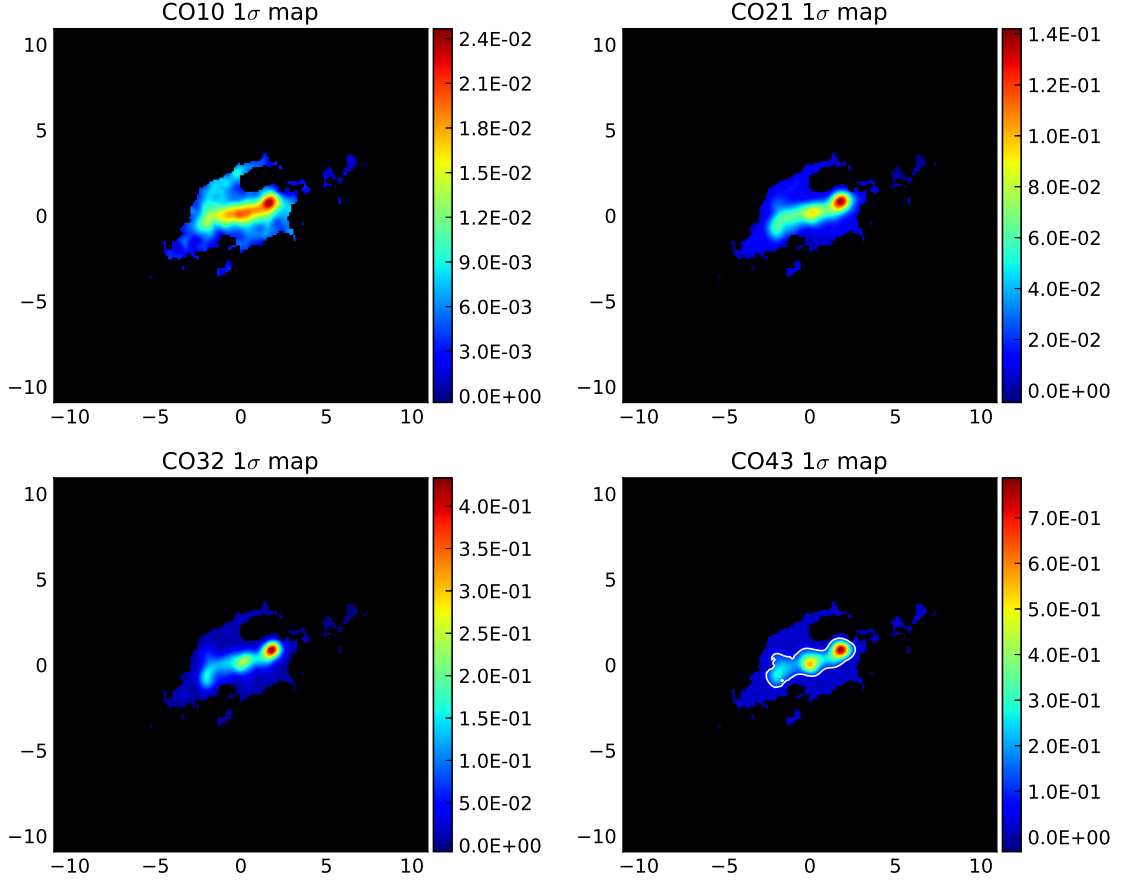


Figure 4.25: Spectrographic mask of  $\Delta v \in [-200, 200] \text{ km s}^{-1}$  for IC 5063, for the CO ( $1 \rightarrow 0$ ), CO ( $2 \rightarrow 1$ ), CO ( $3 \rightarrow 2$ ) and CO ( $4 \rightarrow 3$ ) line transitions. The part outside of the  $1\sigma$  contour in the CO ( $4 \rightarrow 3$ ) transition line map corresponds to the region where the CO ( $1 \rightarrow 0$ ), CO ( $2 \rightarrow 1$ ) and CO ( $3 \rightarrow 2$ ) line transitions exhibited detection, while the CO ( $4 \rightarrow 3$ ) did not. This is due to the fact that the temperature might not be enough to excite the CO gas high enough. Thus the this added region represents an upper bound for the possible presence of excited enough CO gas.

most likely due to the wind outflow. Since the jet passes through that region, it forces the density down, as it pushed the clouds to the "side". This means that the outer regions surrounding the lobe will indeed be of higher density. The whole system there resembles an expanding cocoon. Lastly, the  $N_{\text{CO}}$  follows the distribution of the CO ( $1 \rightarrow 0$ ) line transition, as in the previous galaxies.

Fig. 4.28 displays  $T_{\text{kin}}$ ,  $n_{\text{H}_2}$  and  $N_{\text{CO}}$  for the images created with the spectrographic mask. For the  $T_{\text{kin}}$  and  $n_{\text{H}_2}$  we overplotted contours from  $1\sigma$  up to  $5\sigma$  to differentiate between the regions present in all CO transition lines and the regions which serve as an upper limit for the available flux for the CO ( $4 \rightarrow 3$ ) transition line, shown in dark blue, that correspond to an extending spiral arm structure. Our aim was to check whether there is a "step" between the region of the galaxy and the upper limit region or a smooth transition towards the spiral arm. Indeed, studying the  $T_{\text{kin}}$  graph yields the conclusion that the transition is fairly smooth, with



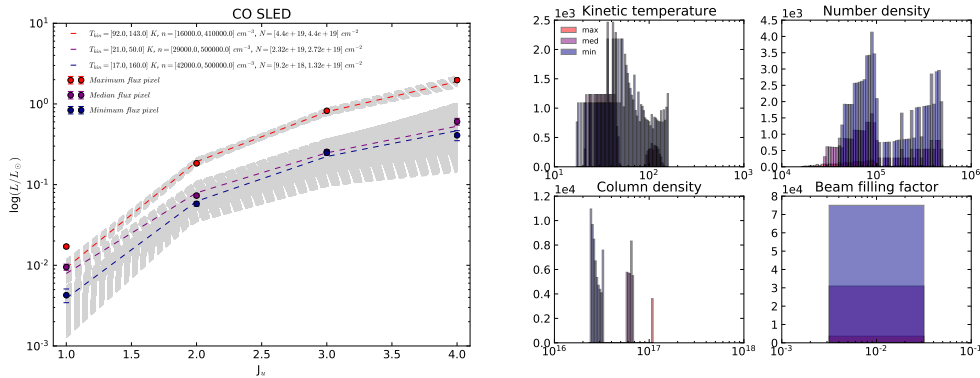


Figure 4.26: *Left to right*: SLEDs and histograms for  $\Delta v = [-200, 200] \text{ km s}^{-1}$ .

a gradient between the two regions of around 5 K. The same procedure was also carried out for a beam filling factor equal to 0.005. There the transition was more step-wise, further cementing our conclusion that the correct choice for the beam filling factor for this galaxy was 0.01. Since we created a two dimensional map for this galaxy’s spiral arm, we need not study it in an integrated manner, as we did with the previous two galaxies.

Another interesting physical quantity regarding this galaxy is the optical depth, shown in fig. 4.29. We expect the gas to be optically thin in the jet impacted regions, due to the turbulence being created. Indeed, we confirm for the CO ( $1 \rightarrow 0$ ) line transition, and even the CO ( $2 \rightarrow 1$ ) line transition that the gas is optically thin in the jet impacted northwest lobe, with values as low as 0.3. We also observe that  $\tau < 1$  in the nucleus and southeast lobe, although somewhat higher than in the northwest lobe.

Finally, shown in fig. 4.30 is the  $T_{\text{ex}}$ . For the CO ( $1 \rightarrow 0$ ) line transitions  $T_{\text{ex}}^{1 \rightarrow 0} \gg 200 \text{ K}$ , while the other three line transitions reach a high of 180 K. This leads to the conclusion that this part of the system is in fact not in LTE. For completion we also included the  $T_{\text{ex}}$  and optical depth maps for the spectrographically masked maps, shown in figs. 4.31, 4.32. The results are quantitatively the same as the  $5\sigma$  maps.

Returning to the results by [Dasyra et al., 2015], we can indeed confirm that the temperature is the highest in the northwest lobe due to the impact by the jet, a whole order of magnitude higher than the ambient ISM. Since RADEX is a non-LTE radiative transfer code, we confirm that we find the same qualitative results by assuming non-LTE, as [Dasyra et al., 2015] did assuming LTE.

### 4.3.3 Residuals

For this galaxy we also intended to study the wind alone. We therefore used a one component gaussian profile for each pixel to fit the flux of the disk and then removed it. The velocity range we assumed for the disk was  $[-250, 250] \text{ km s}^{-1}$ . This meant that the maps were noisier, since the flux to noise ratio decreased. The velocity range we chose here to study the wind is  $\Delta v = [-600, -400] \text{ km s}^{-1}$ , which corresponds to the lower limit used by [Dasyra et al., 2016]. The  $T_{\text{kin}}$ ,  $n_{\text{H}_2}$  and  $N_{\text{CO}}$  are displayed in fig. 4.33, the  $T_{\text{ex}}$  in fig. 4.34 and 4.35.

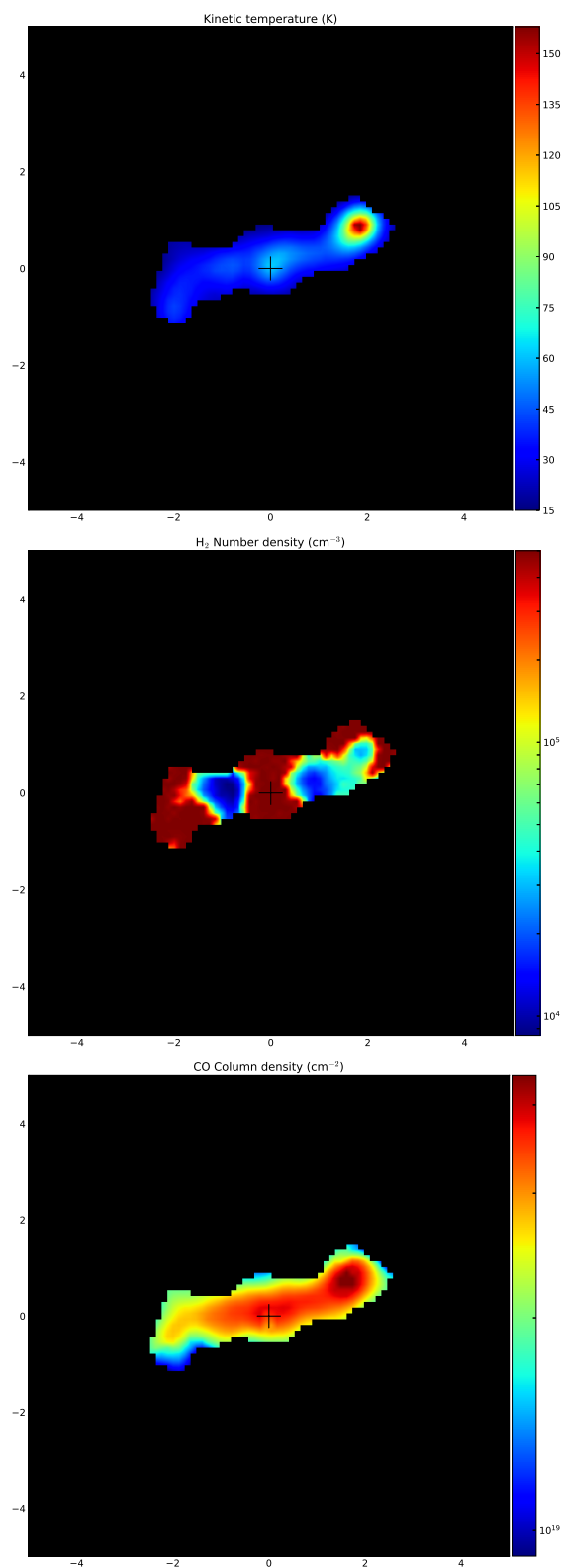


Figure 4.27: *Left to right:*  $T_{\text{kin}}$ ,  $n_{\text{H}_2}$  and  $N_{\text{CO}}$  graphs for  $\Delta v = [-200, 200]$  km s<sup>-1</sup>.

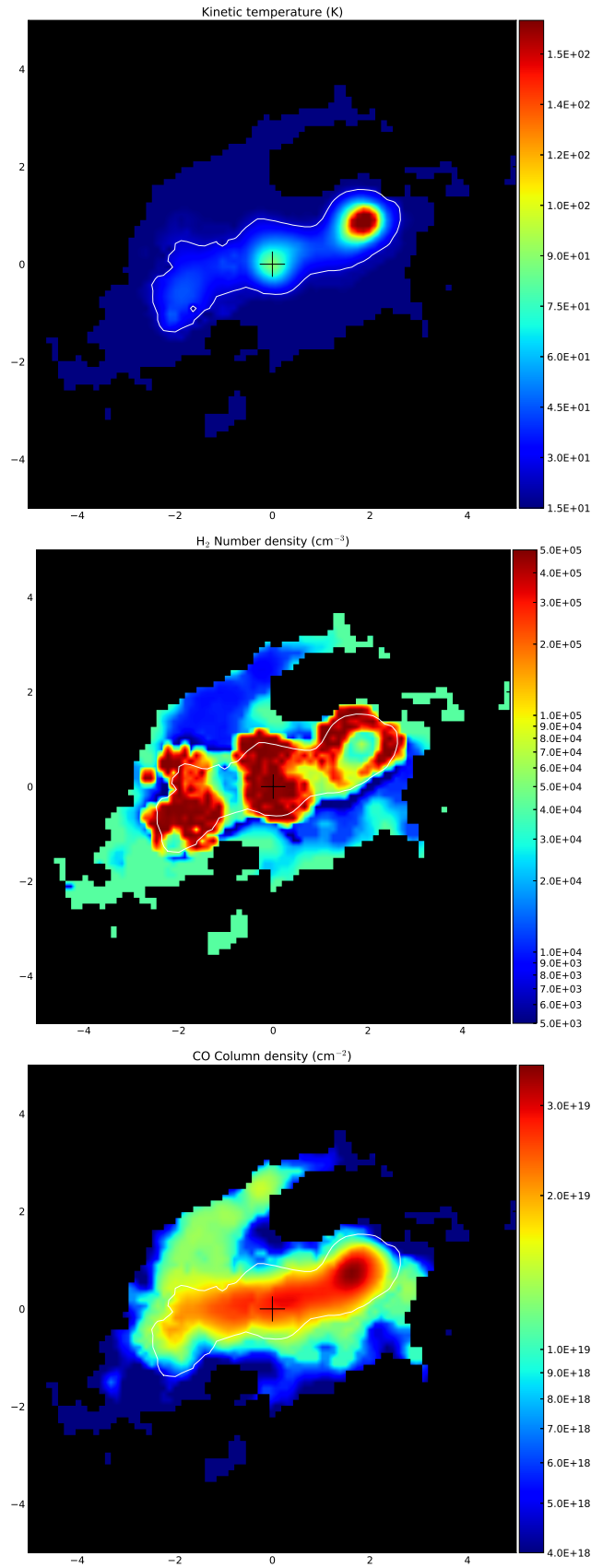


Figure 4.28: *Left to right*:  $T_{\text{kin}}$ ,  $n_{\text{H}_2}$  and  $N_{\text{CO}}$  graphs for  $\Delta v = [-200, 200]$  km s<sup>-1</sup>, corresponding to the input images shown in fig 4.25.

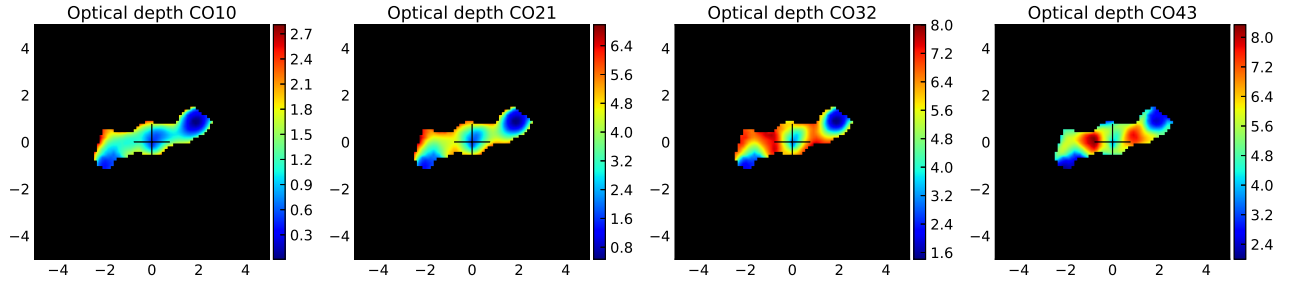


Figure 4.29: *Left to right*: Optical depth graphs for the CO ( $1 \rightarrow 0$ ) through CO ( $4 \rightarrow 3$ ) line transitions.

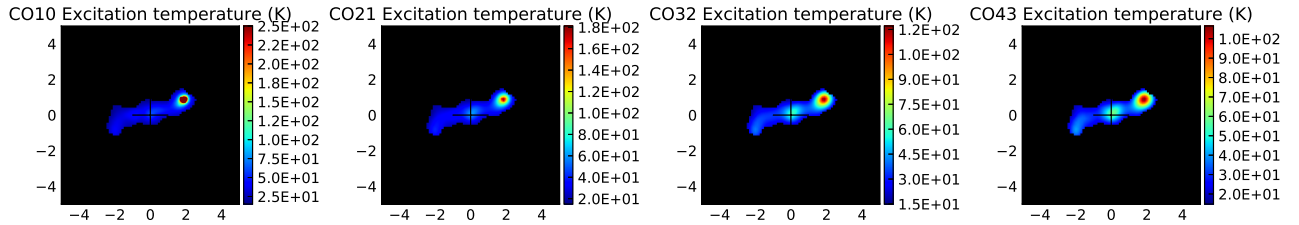


Figure 4.30: *Left to right*:  $T_{\text{ex}}$  graphs for the CO ( $1 \rightarrow 0$ ) through CO ( $4 \rightarrow 3$ ) line transitions.

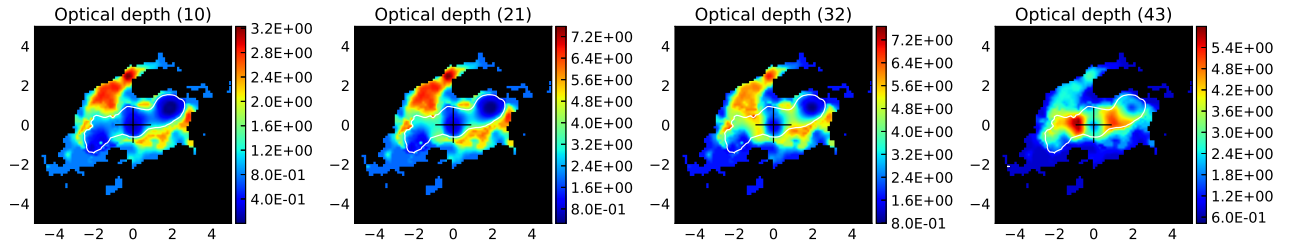


Figure 4.31: *Left to right*: Optical depth graphs for the CO ( $1 \rightarrow 0$ ) through CO ( $4 \rightarrow 3$ ) line transitions for  $\Delta v = [-200, 200] \text{ km s}^{-1}$ , corresponding to the input images shown in fig 4.25.

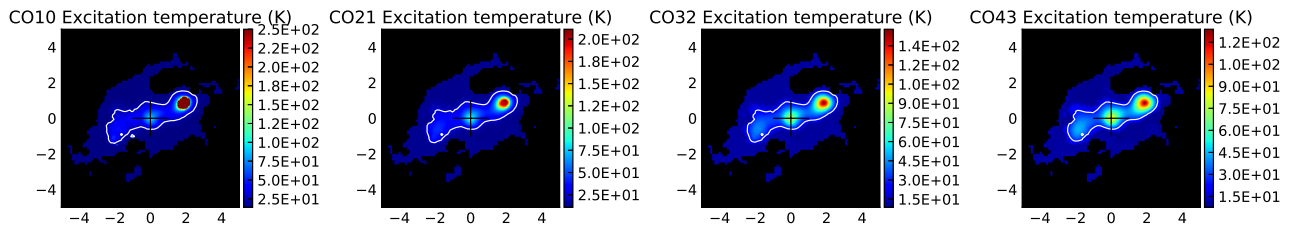


Figure 4.32: *Left to right*:  $T_{\text{ex}}$  graphs for the CO ( $1 \rightarrow 0$ ) through CO ( $4 \rightarrow 3$ ) line transitions for  $\Delta v = [-200, 200] \text{ km s}^{-1}$ , corresponding to the input images shown in fig 4.25.

We only take into consideration the northwestern lobe as in the other regions we did not achieve a satisfactory fit of the disk. The reason for this is that each line had different regions with detection, and only the northwestern lobe exhibited significant detection for all 4 CO line transitions. Furthermore, in this case, we neither implemented the assumption that the  $N_{\text{CO}}$  must follow the distribution of the CO ( $1 \rightarrow 0$ ) line flux, nor a restriction for the  $n_{\text{H}_2}$  in neighbouring regions.

Starting with the  $T_{\text{kin}}$ , we observe a high of 150 K in the northwestern lobe, which as we previously saw corresponds to the jet impacted region. Regarding the  $n_{\text{H}_2}$ , it also is quantitatively the same as in the previous maps that included the disk in the impact region; the  $N_{\text{CO}}$  is  $\sim 3$  times higher in the same region.

We do again confirm that the region is not in LTE, since the  $T_{\text{ex}}$  reaches temperatures over 200 K. The gas again appears to be optically thin in the impact region.

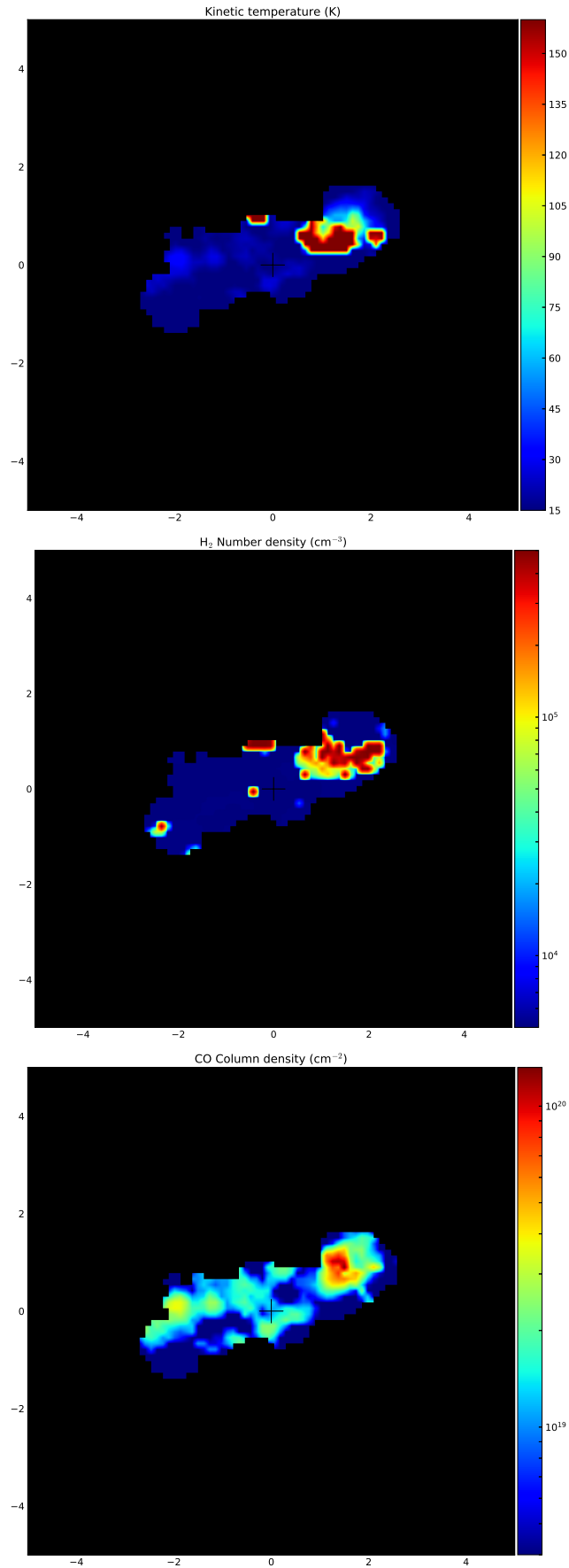


Figure 4.33: *Left to right*: Residual map of the  $T_{\text{kin}}$ ,  $n_{\text{H}_2}$  and  $N_{\text{CO}}$  graphs for  $\Delta v = [-600, -400] \text{ km s}^{-1}$ .

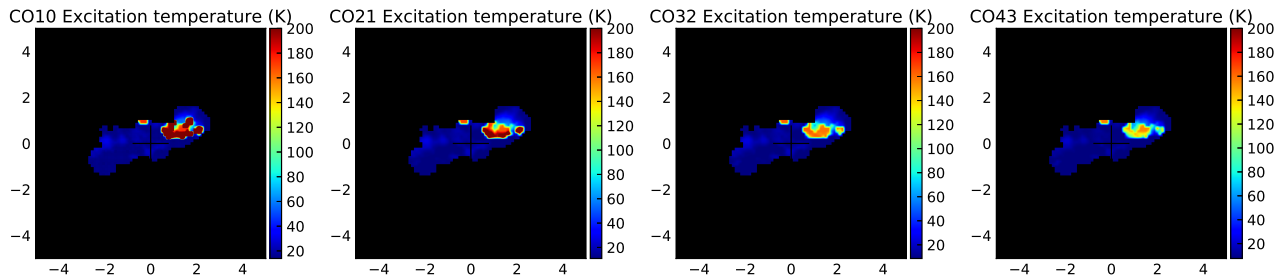


Figure 4.34: *Left to right*: Residual  $T_{\text{ex}}$  graphs for the CO ( $1 \rightarrow 0$ ) through CO ( $4 \rightarrow 3$ ) line transitions for  $\Delta v = [-600, -400]$   $\text{km s}^{-1}$ .

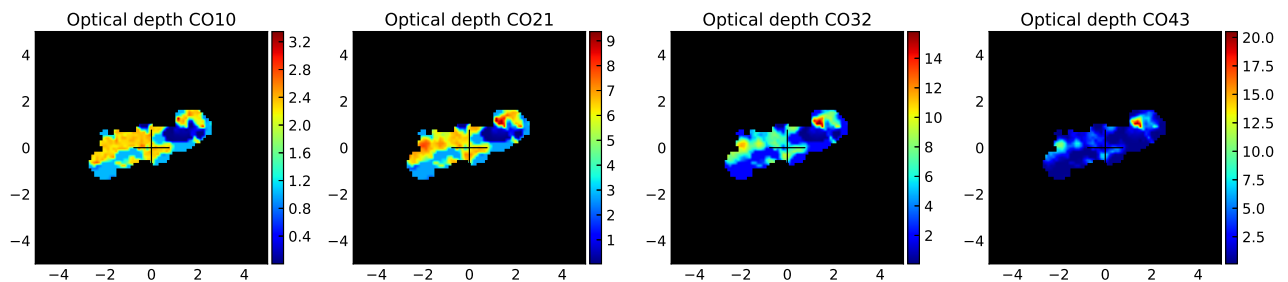


Figure 4.35: *Left to right*: Residual optical depth graphs for the CO ( $1 \rightarrow 0$ ) through CO ( $4 \rightarrow 3$ ) line transitions for  $\Delta v = [-600, -400]$   $\text{km s}^{-1}$ .

## 4.4 Combined excitation study using SLEDs

To comprehensively study the excitation of the molecular gas, we studied the CO SLEDs of the 3 galaxies from our aforementioned sample and added bibliographic data for Mrk 231 [Cicone et al., 2012], [Feruglio et al., 2010], [Rupke and Veilleux, 2011] and NGC 1377 [Aalto et al., 2012], [Aalto et al., 2016], [Aalto et al., 2017]. Specifically, for Mrk 231 we studied the disk and its blueshifted and redshifted wings for the first three CO line transitions, while for NGC 1377 we studied the jet and the galaxy as a whole, having subtracted the jet. Here the CO ( $2 \rightarrow 1$ ), CO ( $3 \rightarrow 2$ ) and CO ( $6 \rightarrow 5$ ) line transitions were available.

They are displayed in fig. 4.36. Each galaxy corresponds to a different marker and line style. They are colour-coded to denote the different regions. Regions shown in blue correspond to outflows, regions in red to disturbed nuclei and regions in green to the quiescent medium. We have normalised each SLED to its CO ( $1 \rightarrow 0$ ) line transition.

One conclusion that can be drawn is that the disturbed nuclei harbour the most excited gas. Additionally, the quiescent medium appears less excited, with the pure outflows displaying intermediate values. Overall we can conclude that the CO excitation is usually higher in pure outflows or nuclei containing winds but with high dispersion in its properties. This falls in line with our aforementioned results, as in that the mass carried by the wind and in disturbed regions decreases, since the  $\alpha_{\text{CO}}$  conversion factor changes.

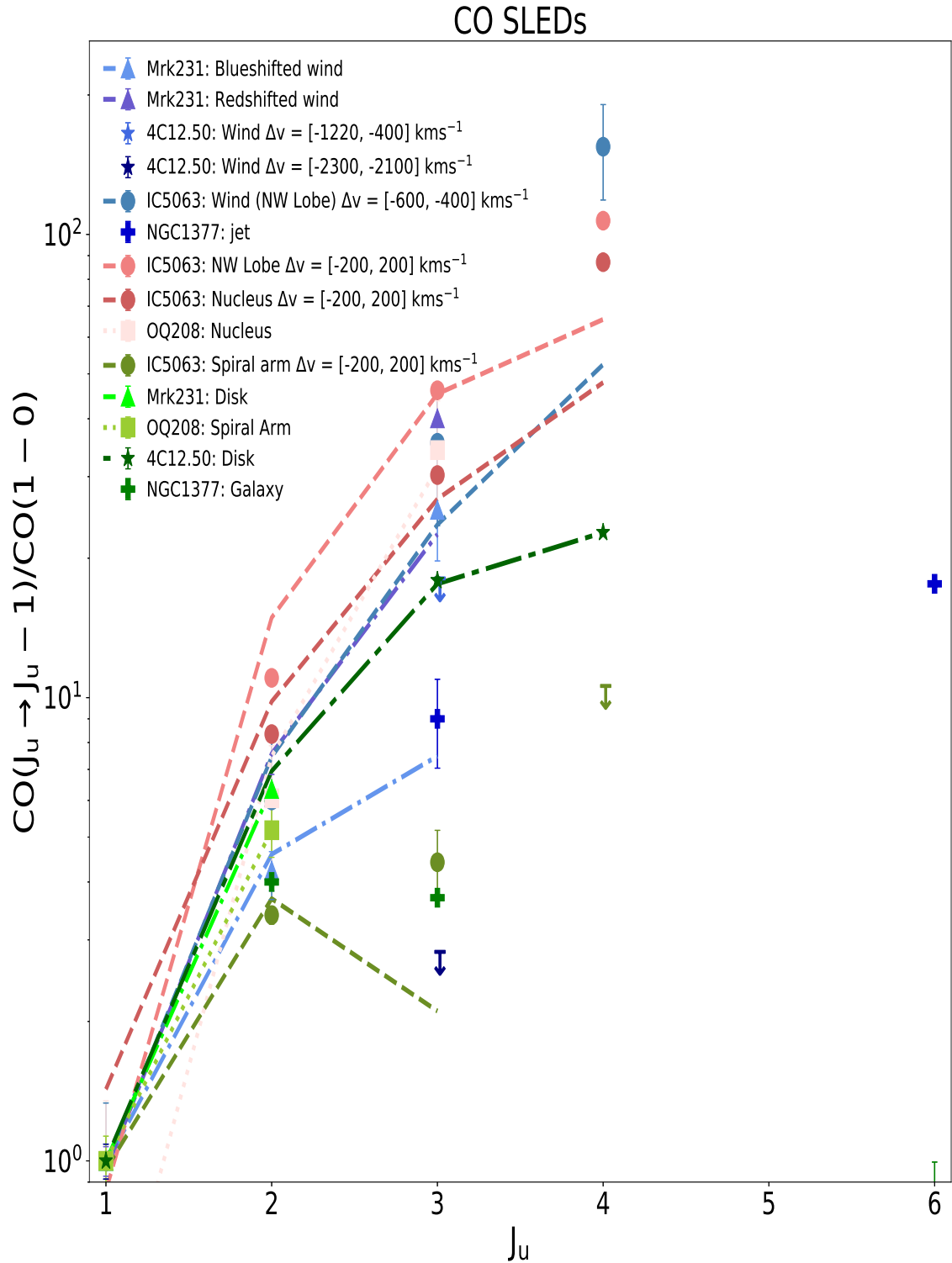


Figure 4.36: Normalised CO SLEDs for OQ208, 4C 12.50 and IC 5063 using our own group’s data and bibliographic data for galaxies Mrk 231 and NGC 1377. The lines and markers distinguish between the different galaxies, whereas the colours symbolise the regions. Blue for outflows, red for disturbed nuclei and green for the quiescent ISM.



# Chapter 5

## Discussion

High pressure regions could cause the gas to flow to lower pressure regions (if they can overcome gravity), and therefore by studying pressure graphs we could detect where the gas flows to. Since

$$P = n_{\text{H}_2} k_{\text{B}} T_{\text{kin}}, \quad (5.1)$$

we can use the product of the  $n_{\text{H}_2}$  and the  $T_{\text{kin}}$  to create such maps in units of  $\text{K cm}^{-3}$ .

Motivated by the work of [Fabian et al., 2005], who studied in X-rays the bubble structures inside the Centaurus cluster, which are produced by the jet's pressurized cocoon, we present in fig. 5.1 the pressure graphs for galaxy IC 5063. We find that it peaks in the nucleus and the 2 lobes. In the northwest lobe it is 2 orders of magnitude higher compared to the ambient medium, and it reaches a high of  $2 \times 10^7 \text{ K cm}^{-3}$ . [Oosterloo et al., 2017] find a pressure of  $10^{6.0} - 10^{7.5} \text{ K cm}^{-3}$ , which is thus confirmed by our models. This indicates high pressure, since typical values would be  $\sim 10^5 \text{ K cm}^{-3}$  [Blitz and Rosolowsky, 2004]. Furthermore it is possible that a cocoon like structure is driving the outflow, due to the likely dominant role of the radio jet in driving the outflow [Oosterloo et al., 2017]. This was also suggested by ionised gas observations by [Morganti et al., 2007] and [Dasyra et al., 2015]. Compared to the spiral arm, the pressure is also clearly higher in the nucleus and lobes, almost 2 orders of magnitude.

High pressure regions are also visible in the disk of galaxy 4C 12.50. Specifically, in fig. 5.2 for the  $\Delta v = [100, 300] \text{ km s}^{-1}$  the pressure changes over 2 orders of magnitude, between the nucleus and the surrounding regions. This again could cause the gas to flow from the central, turbulent region to the outskirts unless it is self-gravitating. Jet activity is known in this nucleus listed in [Lister et al., 2003] and a wind has been detected previously [Fotopoulou et al., 2018]. Other velocity ranges are also displayed for completion, which nonetheless show a lower excitation and pressure gradient, which enables us to conclude that the wind can be described by a variety of conditions.

For galaxy OQ 208, since we found a relatively flat  $n_{\text{H}_2}$  and the pressure is proportional to  $n_{\text{H}_2} \cdot T_{\text{kin}}$  the pressure graph follows the distribution of the  $T_{\text{kin}}$  and does therefore not provide additional information for this galaxy. This is due to the fact that our measurements were not of sufficient quality. It is depicted in fig. 5.3.

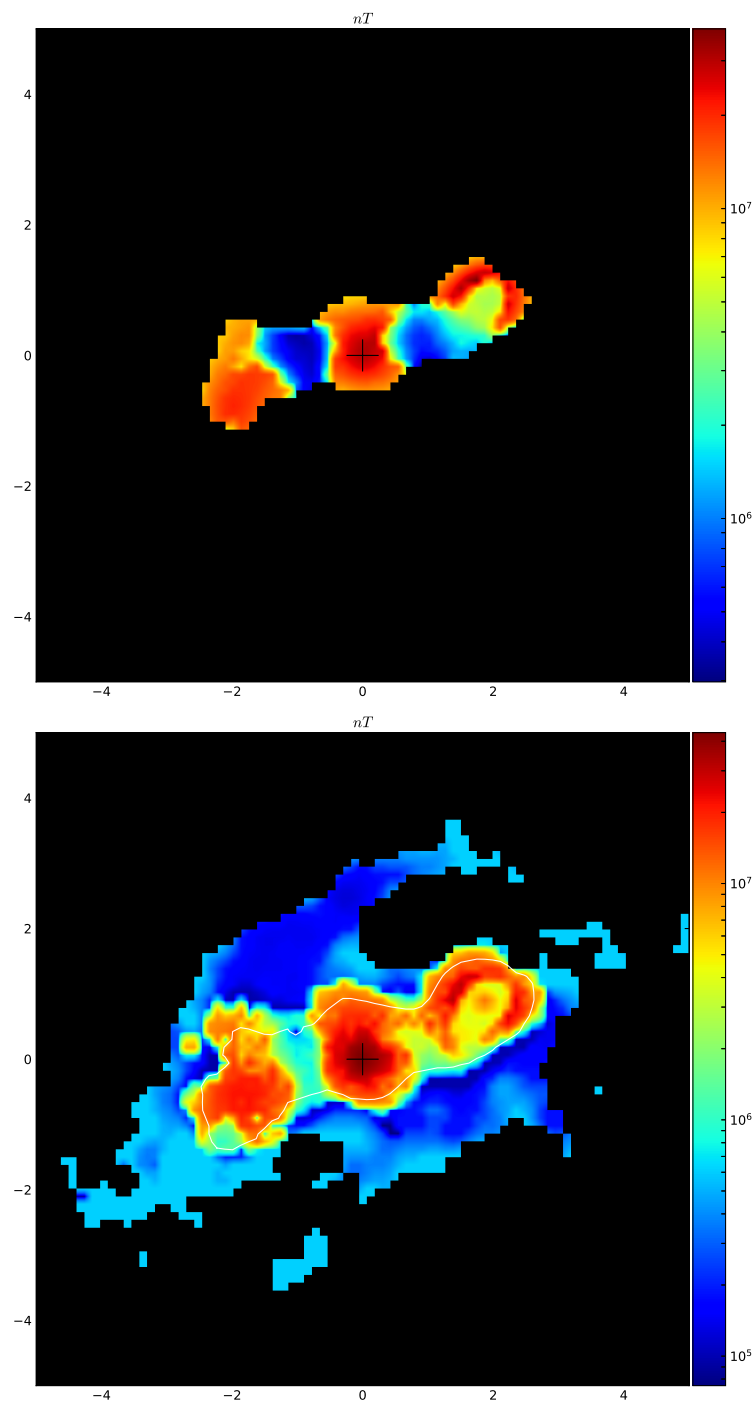


Figure 5.1: Pressure graphs for galaxy IC 5063. *Left*: IC 5063 with a common mask applied to all CO line transitions. *Right*: IC 5063 with a spectral mask consisting of the combination of the first three CO line transitions, as explained in sec. 4.3.1.

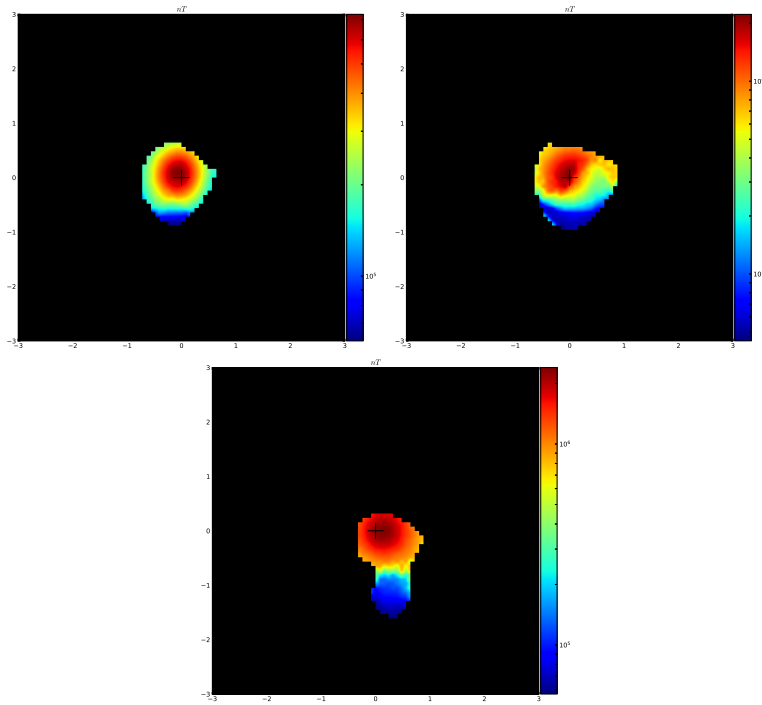


Figure 5.2: Pressure graph for galaxy 4C 12.50. *First 3 maps:*  $\Delta v = [-300, -100] \text{ km s}^{-1}$ ,  $\Delta v = [-100, 100] \text{ km s}^{-1}$  and  $\Delta v = [100, 300] \text{ km s}^{-1}$ .

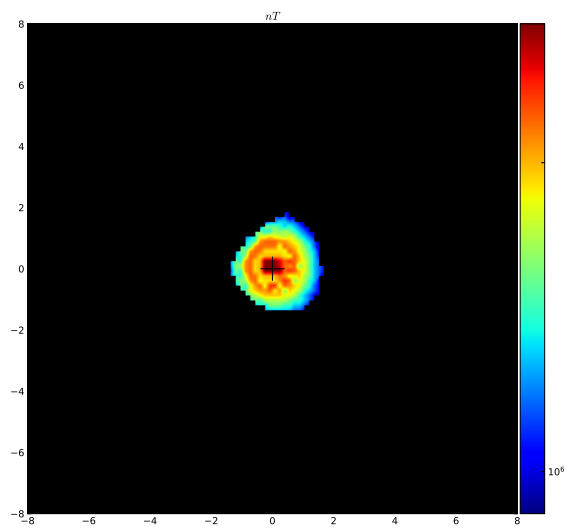


Figure 5.3: Pressure graph for galaxy OQ 208.

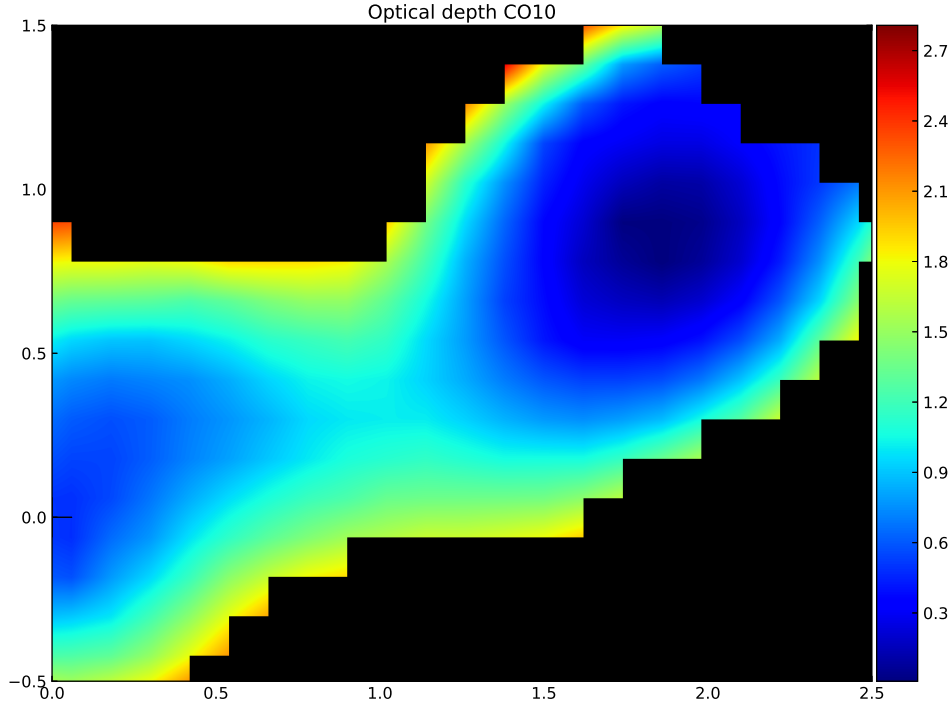


Figure 5.4: Magnification of fig. 4.30. It depicts a trail of optically thin gas connecting the northwest lobe with the central region, corresponding to the jet trail.

The aforementioned analysis indicates that the pressure could be a well suited tracer for outflows originating from jet activity.

When such outflows are created, as the pressure increases and gas gets displaced, the gas in some regions ends up less dense and is characterised by turbulence. This can lower the gas' optical depth. Jet impacted regions can therefore also be characterized by optically thin gas ([Dasyra et al., 2016], [Oosterloo et al., 2017]), which is important for galactic evolution, because in optically thin gas the  $\alpha_{\text{CO}}$  conversion factor differs [Bolatto et al., 2013] and thus the wind mass could be overestimated by up to a factor of 6 [Richings and Faucher-Giguère, 2017].

For galaxy IC 5063, the gas is optically thin in the jet-impacted northwest lobe for both the CO ( $1 \rightarrow 0$ ) and CO ( $2 \rightarrow 1$ ) line transitions. Additionally,  $\tau < 1$  in the nucleus and southeast lobe, but higher than in the northwest lobe. Thus we can tentatively conclude that the optical depth can be used as a tracer for outflows as well. This also corroborated by fig. 5.4, which is a zoomed in version of fig. 4.30. We can see a trail of optically thin gas, along the jet trail, connecting the origin of the jet in the nucleus with the impact site in the northwestern lobe. Likewise for 4C 12.50, for the velocity range of  $\Delta v = [-300, -100] \text{ km s}^{-1}$  we found that the optical depth map of the CO ( $1 \rightarrow 0$ ) line transition shows a region to the north where  $\tau < 1$ , that corresponds to a high  $T_{\text{kin}}$ , higher than the  $T_{\text{kin}}$  at the nucleus. This could be attributed to the jet activity in that region.

# Chapter 6

## Conclusions

We obtained sub-mm data from the PdB and SMA for OQ 208 and ALMA data for 4C 12.50 and IC 5063 to study the effects of jet interactions with the ambient ISM. To achieve this we created maps for the  $T_{\text{kin}}$ ,  $n_{\text{H}_2}$ ,  $N_{\text{CO}}$ ,  $T_{\text{ex}}$ , as well as the optical depth and pressure. We found that OQ 208 exhibits a  $T_{\text{kin}}$  of  $\sim 20$  K at its nucleus, which is typical for a galaxy rich in gas. The almost entirely flat  $n_{\text{H}_2}$  results in the pressure following the distribution of the kinetic temperature, with a maximum of  $3 \times 10^6 \text{ K cm}^{-3}$ . The  $T_{\text{ex}}$  graph reaches a high of 20 K at the nucleus, with a gradient of  $\sim 10$  K between the outer and inner regions. This is expected for a spiral galaxy. All three  $T_{\text{ex}}$  graphs follow the same distribution as the  $T_{\text{kin}}$  leading to the conclusion that the system is in LTE.

Galaxy 4C 12.50 was studied in three symmetrical velocity ranges. The blueshifted side of the galaxy's disk corresponds to a  $\Delta v$  of  $[-300, -100] \text{ km s}^{-1}$ . The  $T_{\text{kin}}$  reaches a high of 55 K in the central region, which is still lower than the excitation temperature of the CO ( $1 \rightarrow 0$ ) line transition in that region. Specifically,  $T_{\text{ex}}^{1 \rightarrow 0} \approx 70$  K at the center, which suggests that the system is not in LTE. This is corroborated by the fact that for this velocity range the optical depth at the central region is below 1, making the gas optically thin. Thus the gas could be excited in this region due to a wind originating from a stellar jet.  $\Delta v$  of  $[-100, 100] \text{ km s}^{-1}$  depicts the galaxy's nucleus. For this velocity range we can observe that the  $n_{\text{H}_2}$  varies over an order of magnitude. Accordingly, the pressure changes over an order of magnitude as well. The  $T_{\text{kin}}$  on the other hand is highest at the central region, at 40 K. The redshifted side of the galaxy's disk is observed in  $\Delta v$  of  $[100, 300] \text{ km s}^{-1}$  velocity range. It is more asymmetric, compared to the previous 2 velocity ranges and the  $T_{\text{kin}}$  is also the lowest, at 30 K. The northern region is characterised by a high number density and pressure, while the southern region exhibits the opposite traits, mainly low pressure and low density.

Moving on to IC 5063 we saw that the  $T_{\text{kin}}$ ,  $N_{\text{CO}}$  and  $T_{\text{ex}}$  reach their highest values in the lobes and the nucleus. However, the  $n_{\text{H}_2}$  and pressure only reach high values in the nucleus and southeast lobe. In the northwest lobe they fall considerably exactly at the core, something that can be attributed to the jet. Further out they reach their highest values, creating a cocoon structure in the outermost parts of the northwestern lobe. The optical depth is below 1, meaning that the gas is optically thin in the northwestern lobe, which is consistent with the suspected

gas activity, that causes turbulence in that region. Excited gas is observed along the jet trail, which means that the radiation stemming from the gas is dominated by gas that has interacted with the jet. The structure appears to be out of thermal equilibrium, as the  $T_{\text{ex}}$  of the CO ( $1 \rightarrow 0$ ) line transition reaches values  $\gg 200$  K, in stark contrast to the three other line transitions where the  $T_{\text{ex}}$  stays under 180 K. The pressure fluctuates over two orders of magnitude, which most likely corresponds to the interaction of the gas with the jet.

To calculate the mass content expressed by the  $\alpha_{\text{CO}}$  conversion factor, we use the  $T_{\text{ex}}$  obtained from the integrated SLEDs for the optically thin case, and the  $T_{\text{kin}}$  for the optically thick cases. For OQ 208 we find that the  $\alpha_{\text{CO}}$  conversion factor of the whole extent of the galaxy is 1.3 times higher than  $\alpha_{\text{CO}}$  of the spiral arm. This leads to the conclusion that higher temperature regions are associated with higher  $\alpha_{\text{CO}}$  conversion factors, leading to more mass accumulation in those regions. In 4C 12.50's case we find  $\alpha_{\text{CO}}$ s of  $0.71 M_{\odot} (\text{K km s}^{-1} \text{pc}^2)^{-1}$  for the  $[-300, -100] \text{ km s}^{-1}$  range, which is optically thin. For the other two velocity ranges we found  $\alpha_{\text{CO}}$  conversion factors of 10.2 and  $35.7 M_{\odot} (\text{K km s}^{-1} \text{pc}^2)^{-1}$  respectively.

Summing up, we studied the properties of the ISM in jet impacted regions. We found that the  $T_{\text{kin}}$  rises up to an order of magnitude in the jet impacted regions, compared to the ambient ISM. The  $T_{\text{ex}}$  is higher than the  $T_{\text{kin}}$  in these regions. If we combine this with the optical depth maps, which show that the gas is optically thin in those regions, we can conclude that the gas is highly excited and not in LTE. The pressure maps also trace the expansion of the gas, particularly in IC 5063, where a cocoon structure is visible in the northwestern lobe.

# Bibliography

- [Aalto et al., 2016] Aalto, S., Costagliola, F., Muller, S., et al. (2016). A precessing molecular jet signaling an obscured, growing supermassive black hole in NGC1377? *A&A*, 590(A73).
- [Aalto et al., 2017] Aalto, S., Muller, S., Costagliola, F., et al. (2017). Luminous, pc-scale CO 6–5 emission in the obscured nucleus of NGC 1377. *A&A*.
- [Aalto et al., 2012] Aalto, S., Muller, S., Sakamoto, K., et al. (2012). Winds of change - a molecular outflow in NGC 1377? *A&A*.
- [Baryshev et al., 2015] Baryshev, A. M., Hesper, R., Mena, F. P., et al. (2015). The ALMA Band 9 receiver. *A&A*, A29(577).
- [Blitz and Rosolowsky, 2004] Blitz, L. and Rosolowsky, E. (2004). The role of pressure in giant molecular cloud formation. *ApJ*, 612(L29).
- [Bolatto, 2015] Bolatto, A. D. (2015). Using CO to measure molecular masses. *Proceedings for invited presentation to the 6th Zermatt Symposium*.
- [Bolatto et al., 2013] Bolatto, A. D., Wolfire, M., and Leroy, A. K. (2013). The CO-to-H<sub>2</sub> conversion factor. *ARAA*.
- [Cicone et al., 2012] Cicone, C., Feruglio, C., Maiolino, R., et al. (2012). The physics and the structure of the quasar-driven outflow in Mrk 231. *A&A*, 543(A99).
- [Dasyra et al., 2015] Dasyra, K. M., Bostrom, A. C., Combes, F., et al. (2015). A radio jet drives a molecular and atomic gas outflow in multiple regions within one square kiloparsec of the nucleus of the nearby galaxy IC 5063. *ApJ*, 815(34).
- [Dasyra and Combes, 2012] Dasyra, K. M. and Combes, F. (2012). Cold and warm molecular gas in the outflow of 4C12.50. *A&A*.
- [Dasyra et al., 2014] Dasyra, K. M., Combes, F., Novak, G. S., et al. (2014). Heating of the molecular gas in the massive outflow of the local ultraluminous-infrared and radio-loud galaxy 4C12.50. *A&A*.
- [Dasyra et al., 2016] Dasyra, K. M., Combes, F., Oosterloo, T., et al. (2016). ALMA reveals optically thin, highly excited CO gas in the jet-driven winds of the galaxy IC5063. *A&A*.

- [Dickman et al., 1986] Dickman, R. L., Snell, R. L., Schloerb, F. P., et al. (1986). ALMA reveals optically thin, highly excited CO gas in the jet-driven winds of the galaxy IC5063. *ApJ*, 309:326–330.
- [Emonts et al., 2005] Emonts, B. H. C., Morganti, R., Tadhunter, C. N., et al. (2005). A jet-induced outflow of warm gas in 3C293. *MNRAS*, 362(3):931–944.
- [Fabian et al., 2005] Fabian, A. C., Sanders, J. S., Taylor, G. B., et al. (2005). A deep Chandra observation of the Centaurus cluster: bubbles, filaments and edges. *MNRAS*.
- [Fendt, 2006] Fendt, C. (2006). Quasar feedback revealed by giant molecular outflows. *ApJ*, 651:272–287.
- [Feruglio et al., 2010] Feruglio, C., Maiolino, R., Piconcelli, E., et al. (2010). Quasar feedback revealed by giant molecular outflows. *A&A*, 518.
- [Fotopoulou et al., 2018] Fotopoulou, C. M., Dasyra, K. M., Combes, F., et al. (2018). CO emission from the wind of the radio galaxy 4C12.50 seen by ALMA. *A&A*.
- [Holt et al., 2009] Holt, J., Tadhunter, C. N., and Morganti, R. (2009). The ionization of the emission-line gas in young radio galaxies. *MNRAS*, 400:589–602.
- [Lanz et al., 2016] Lanz, L., Ogle, P., Alatalo, K., et al. (2016). Star formation suppression due to jet feedback in radio galaxies with shocked warm molecular gas. *ApJ*.
- [Lister et al., 2003] Lister, M. L., Kellermann, K. I., Vermeulen, R. C., et al. (2003). 4C12.50: A superluminal precessing jet in the recent merger system IRAS 13451+1232. *ApJ*, 584(1).
- [Lü, 1972] Lü, P. K. (1972). Optical Monitoring of Quasistellar Objects. I. *ApJ*, 77:829.
- [Massaro et al., 2009] Massaro, E., Giommi, P., Leto, C., et al. (2009). Roma-BZCAT: A multifrequency catalogue of Blazars. *A&A*.
- [Morganti et al., 2007] Morganti, R., Holt, J., Saripalli, L., et al. (2007). IC 5063: AGN driven outflow of warm and cold gas. *A&A*, 476(2):735–743.
- [Morganti et al., 2015] Morganti, R., Oosterloo, T., Oonk, J. B. R., et al. (2015). The fast molecular outflow in the Seyfert galaxy IC 5063 as seen by ALMA. *A&A*, 580(A1).
- [Morganti et al., 1998] Morganti, R., Oosterloo, T., Tsvetanov, Z., et al. (1998). A radio study of the Seyfert galaxy IC 5063: Evidence for fast gas outflow. *AJ*, 115(915).
- [Oosterloo et al., 2000] Oosterloo, T., Morganti, R., Tzioumis, A., et al. (2000). A strong jet/cloud interaction in the Seyfert galaxy IC 5063: VLBI observations. *AJ*, 19(2085).



- [Oosterloo et al., 2017] Oosterloo, T., Oonk, J. B. R., Morganti, R., et al. (2017). Properties of the molecular gas in the fast outflow in the Seyfert galaxy IC 5063. *A&A*, 608(A38).
- [Osterbrock and Ferland, 2006] Osterbrock, D. E. and Ferland, G. J. (2006). Astrophysics of gaseous nebulae and active galactic nuclei. *Astrophysics of gaseous nebulae and active galactic nuclei, 2nd. ed. by D.E. Osterbrock and G.J. Ferland. Sausalito, CA: University Science Books, 2006.*
- [Richings and Faucher-Giguère, 2017] Richings, A. J. and Faucher-Giguère, C.-A. (2017). The origin of fast molecular outflows in quasars: molecule formation in AGN-driven galactic winds. *MNRAS*.
- [Rupke and Veilleux, 2011] Rupke, D. S. N. and Veilleux, S. (2011). Integral field spectroscopy of massive, kiloparsec-scale outflows in the infrared-luminous qso Mrk 231. *ApJL*, 729(2).
- [Tadhunter et al., 2014] Tadhunter, C., Morganti, R., Rose, M., et al. (2014). Jet acceleration of the fast molecular outflows in the Seyfert galaxy IC 5063. *Nature*, 511:440–443.
- [Tetarenko et al., 2017] Tetarenko, A. J., Freeman, P., Rosolowsky, E., et al. (2017). Mapping jet-ISM interactions in X-ray binaries with alma: A GRS 1915+105 case study. *MNRAS*.
- [van Breugel et al., 1985] van Breugel, W., Filippenko, A. V., Heckman, T., et al. (1985). Minkowski’s object - A starburst triggered by a radio jet. *ApJ*, 293:83–93.
- [van der Tak et al., 2007] van der Tak, F. F. S., Black, J. H., Schöier, F. L., et al. (2007). A computer program for fast non-LTE analysis of interstellar line spectra. *A&A*, 468(2):627–635.
- [Véron-Cetty and Véron, 1993] Véron-Cetty, M.-P. and Véron, P. (1993). A Catalogue of quasars and active nuclei. *ESO Sci. Rep. 13*.

# Appendix A

## Python code

### A.1 Grid

The code below is used to create a grid of the parameters put out by RADEX. It loops over a different input vector of the  $T_{\text{kin}}$ ,  $n_{\text{H}_2}$  and  $N_{\text{CO}}$  and it puts out the  $T_{\text{ex}}$ , optical depth and flux. RADEX is written in Fortran, which is inconsistent with its scientific notation. Therefore we implemented a function that checks if each number is readable by python and if it is not, it converts it to a suitable form.

```
1 execfile('fits_handling.py')
2 from itertools import chain
3 import re
4 ##----- Fix Fortran -----##
5 def fortran_fix(str2num):
6     try:
7         return float(str2num)
8     except:
9         return float(re.findall('[+-]?\d+?[.]\d+',str2num)[0]+'E'+re.
10 findall('[+-]?\d+$',str2num)[0])
11 ##-----##
12 ##----- Create Radex output -----##
13 def read_radex(outfile):
14     line = outfile.readline()
15     words = line.split()
16     while (words[1] != "T(kin)"):
17         line = outfile.readline()
18         words = line.split()
19     temp = float(words[-1])
20     line = outfile.readline()
21     words = line.split()
22     dens = float(words[-1])
23     while (words[1] != "Column"):
24         line = outfile.readline()
25         words = line.split()
26     column = float(words[-1])
27     while (words[-1] != "FLUX"):
28         line = outfile.readline()
29         words = line.split()
30     line = outfile.readline()
```

```

31 freq=[0]; flux=[0]; T_R=[0]; Tex=[0]; TAU=[0]; ftmp = 0.; i=0.
32 while (ftmp+freq[0] < 500.):
33     line = outfile.readline()
34     words = line.split()
35     ftmp = float(words[4])
36     i+=1
37     if (i == 1):
38         freq[0] = fortran_fix(words[4])
39         flux[0] = fortran_fix(words[-1])
40         T_R[0] = fortran_fix(words[-5])
41         Tex[0] = fortran_fix(words[-7])
42         TAU[0] = fortran_fix(words[-6])
43
44     else:
45         flux.append(fortran_fix(words[-1]))
46         freq.append(fortran_fix(ftmp))
47         T_R.append(fortran_fix(words[-5]))
48         Tex.append(fortran_fix(words[-7]))
49         TAU.append(fortran_fix(words[-6]))
50
51 result=[]; result.extend([[temp],[dens],[column],freq,flux, Tex,T_R,
TAU])
52 return result
53 ##-----##
54
55
56 ##----- Grid creation -----##
57 def radex_grid(temper,densities,columns,tbg=2.73,dv=1.):
58     chunk=int(np.array(temper).shape[0]*np.array(densities).shape[0]*np
.array(columns).shape[0]/10.)
59     if chunk==0:
60         raise Exception('Looks like chunk=0.')
61     results=[];times=0
62     for temp in(temper):
63         for dens in(densities):
64             for ncol,col in enumerate(columns):
65                 infile = open('/mnt/disk1/models/Radex/data/input.rdx','w')
66                 infile.write('50 500 '+str(int(temp))+ ' '+str(int(
dens))+ ' 2.73 '+str(col)+ ' '+str(int(dv))+ '\n')
67                 infile.write('\n')
68                 infile.close()
69                 os.system('/mnt/disk1/models/Radex/src/radex')
70                 outfile = open('output.rdx')
71                 results.append(list(chain.from_iterable(read_radex(
outfile))))
72                 times+=1
73                 if times%chunk==0:
74                     np.savez(str(int(times/chunk))+'_gr',results)
75                     del results[:]
76                 if times==np.array(temper).shape[0]*np.array(densities).shape[0]*np
.array(columns).shape[0]:
77                     np.savez(str(int(times/chunk)+1)+'_gr',results)
78                     del results[:]
79                 file_list=sorted([filename for filename in os.listdir('.') if
filename.endswith('_gr.npz')], key=lambda s: list(map(int,re.
findall("\d+",s))))

```

```

80     arr=[np.load(file_name) ['arr.0'] for file_name in file_list]
81     if len(arr[-1])==0: arr=arr[:-1] #It can happen that one extra
      empty file is created at the end, so that line removes it.
82     np.savez('final',np.vstack(arr))
83     for filename in os.listdir('.'):
84     if filename.endswith('_gr.npz'): os.remove(filename)
85     return 'Done'
86     ##-----##
87
88
89     ##----- Input parametres -----##
90     temper=np.arange(3,220,1)
91     dens=np.hstack(np.arange(1,10.5,0.5)*i for i in np.logspace(3,7,5))
92     col=np.hstack(np.arange(1,10.5,0.5)*i for i in np.logspace(13,19,8))
93     radex_grid(temper,dens,col)
94     ##-----##

```

Since we do not use the whole extent of the grid for each run, we select the upper and lower limits for each subgrid, using the code below.

```

1 nohup=False
2 if nohup: answer = False
3 else: answer=bool(raw_input('Steps: input, no steps: no input '))
4
5 if nohup: t_min, t_max, n_min, n_max, c_min, c_max = 5, 130, 1e3, 1e5,
      1e16, 5e17
6 else: t_min, t_max, n_min, n_max, c_min, c_max = map(float, raw_input('
      t_min, t_max, n_min, n_max, c_min, c_max: ').split())
7
8 TextFileReader = pd.read_csv('/mnt/disk1/models/Fixed.rdx', header=None
      , chunksize=1024)
9 dfs=[(chunk_df.loc[(chunk_df[0] >= t_min) & (chunk_df[0] <= t_max) & (
      chunk_df[1] >= n_min) & (chunk_df[1] <= n_max) & (chunk_df[2] >=
      c_min) & (chunk_df[2] <= c_max)]) for chunk_df in TextFileReader]
10 df = pd.concat(dfs, sort=False)
11
12 if answer:
13     step, number_of_times = raw_input('step, number_of_times: ').split(
      ' ')
14     for i in range(int(number_of_times)):
15         df=df.drop(df.iloc[:,int(step)].index, 0)
16
17 df.to_csv('/mnt/disk1/models/GRID_updated_IC_fat_new.rdx', header=None,
      index=None, sep=',', mode='w')

```

## A.2 Maps

This section of the code loops over the grid created above and uses a reduced  $\chi^2$  minimisation to find the best fit for each pixel. Then it puts out the maps. More detailed explanations are found in the commentary below.

```

1  '''
2      This script takes as input PrimaryHDU objects (first element of the
3      fits container files) and a grid produced with the RADEX code. The
4      "factor" variable is the beam filling factor and "N" is the number
5      of input files.
6
7      The loop_radex_solution function handles the imported objects and
8      replaces the None values with copies of the imported ones. The
9      filenames variable refers to the input list of collapsed images for
10     the line transitions in question.
11     An explanation of each variable follows:
12     -dictionary_init: If filename !=None this dictionary imports the
13     file.
14     -dictionary_v: The velocities corresponding to each file that has
15     not been imported are set to nan.
16     -Fits: In order to replace the None values with copies of files ,
17     Fits is initialized as a copy of the first element of
18     dictionary_init. The header is kept as is, the data counterpart is
19     set to 0
20     -dictionary_upd: The files that have not been imported are set
21     equal to a copy of the first file that has been imported, by using
22     the variable Fits.
23     -dictionary: Contains the imported files and the copies of the
24     first imported file for the None values, in the correct order.
25     -dictionary_upd_v: The (observed) velocities corresponding to the
26     imported files are set equal to the difference of velocities stated
27     in the header.
28     -dictionary_v: This dictionary is now set in the right order, as in
29     "v1"=0, "v2"=200 etc.
30     -v_obs: A list containing only the values of the velocities.
31     -dictionary_data: A list of arrays containing the .data
32     counterparts of the imported images. For example the first entry is
33     im1.data. dummy1 loops over the indices and dummy2 takes the
34     values as arguments. The "from_spiral" function is called in order
35     to read the elements in a clockwise manner starting from the centre
36     and moving out.
37
38     Brief explanation of the 'Spiral' section of the code. It
39     consists of 4 functions. Only 'to_spiral' and 'from_spiral' are
40     ever called from the code itself. 'spiral_cw' (clockwise) creates
41     an array with the elements in a clockwise pattern, starting from
42     the centre, for a given array and 'base_spiral' reads them in a
43     reverse order. 'from_spiral' creates the spiralled array on which
44     we perform the various minimisations, while 'to_spiral' returns the
45     array to its initial form for the graphic output.
46     The flag spiral_check, checks whether the the array is to be
47     read in a spiral or not.
48     -flux_central: Flux of the central pixel (CO10). Depends if we use
49     a spiral or not as to which are the coordinates (for spiral: 0,0).
50     -max_pixel: Coordinates of maximum flux pixel (max of CO10 array).

```

```

20  -min_pixel: Coordinates of minimum of CO10 array.
21  -med_pixel: Coordinates of closest value to median flux of CO10
    array.
22  -max_r_pixel: Coordinates of the pixel with the highest CO43/CO10
    ratio.
23  -min_r_pixel: Coordinates of the pixel with the lowest CO43/CO10
    ratio.
24  -fl_med: Median flux of CO10 array.
25  *if CO10 is not available, then it's always the lowest transition
    available, so probably CO21*
26  -ratio: Ratio of 2 lines. Could be more generalised by using a user
    input.
27
28      Finally the physical quantities in question are initialized as
    zero arrays.
29
30      Next the script loops over each element of the .data part of each
    PrimaryHDU object. If any one of those elements is nan, all the
    physical quantities are set to nan as well. Else the errors are set
    equal to the standard deviation obtained from the header or nan,
    if there was no input file. Finally, results_radex is called and
    its output is appended to the physical quantities, which are then
    returned by the loop_radex_solution function.
31      Specifically:
32      -err_obs: Creates a dictionary containing the standard deviations
    for each error to impliment chi^2, from the header. It is then
    brought into the correct order.
33
34      Update: 1) 3 ifs were added. They check if the i,j pixel is one of
    the max, med or min and if that is the case, they are mapped to a
    color corresponding to the intensity chromatically (e.g., max=red).
    The 'all' module from numpy checks if an array consists entirely
    of True values. Then the color (or lack of it) is passed to the
    radex solution function.
35      2) An if-else clause to check if the [i,j]==[0,0] is added. If that
    is the case and radex_solution is called for the first time, no
    arguments are added. If it is not the case, the central number
    density, central column density, central flux, median flux, n_{k-1}
    and N_{k-1} are passed as well. They are used as constraints in
    the chi^2 minimisation inside radex_solution.
36      3) The variable ratio contains an array where each pixel represents
    the ratio of the last available CO line transition over the first
    available CO line transition.
37      The radex_solution function takes as inputs the observed fluxes and
    errors, the beam filling factor (all numpy arrays) and the
    emitting region size (in arcseconds). The integration constant is
    derived by integrating the RJ law over the line width, while 206265
    is the number of seconds of arc in a radian. The flux is obtained
    in Jy*Hz/kms in order for the N_CO to be in cm^-2/kms. Then, the
    N_CO is multiplied by each line width (in the graphs section).
38
39      The grid which is passed as an argument defines the physical
    quantities:
40      -T_R: Radiation temperature
41      -T: Kinetic temperature
42      -n: Number density

```

```

43 -N: Column density
44 -Tex: Excitation temperature of the CO:1→0 transition
45 -TAU: Optical depth
46 The variable sigma constrains the maximum value of the chi2
variable. E.g. for 5 times the error: sigma= $\sum_0^k(\text{error})^2$ . For
47 4 line transitions k=4 and thus sigma=52*4=100.
48 Nlines is the number of available CO lines.
The array chi2 is initialized as an array with its elements set to
infinity, with the size of the input file and the beam filling
factor. Then they are replaced by the output of the chisqfunc
function, unless the optical depth exceeds 100. Radex does not work
correctly in this region and the chisqfunc function is not called.
Instead chi2 retains the infinite value in this position and gets
not considered in the search for the minimum value.
49 The minimum of chi2 has 2 coordinates, the first one corresponding
to the file index, the second one to the beam filling factor and is
found by the best_fit variable. It keeps the unique solutions, so
that one can look through the different solutions. The first index
corresponds to the (N+1)th best fit. The second index commands
which solution of the unique ones to keep, i.e. if 2 solutions
put out the same chi2, one can decide which of those 2 to display.
(If the solutions do not need to be unique: np.argwhere(chi2 == np
.min(chi2)).)
50
51 Constraints:
52 i) 0<tau<100
53 ii) Tex(CO10)<5.53K ( $E_J / k_B \approx 5.53 J (J + 1)/2$  for J
=1)
54 iii) bff=1 (maximum value) used to estimate a lower value for
TR in the RJ limit
55 Not for first run:
56 iv) The relative difference between nk and n{k-1} cannot be
over a certain value depending on each galaxy.
57 v) The column density must follow the distribution of the flux
+ 1sigma.
58 vi) The chi2 variable must be lower than certain number of
sigma
59 The 'counter' counts how many times a solution that satisfies all
constraints is found. It is needed to reject all lines of 'chi2'
that contain only inf.
60 -best_fit: Finds the coordinates of the first minimum chi2.
61 -best_fit_full: 2D array. Coordinate 0: the line of the grid for
each solution in decreasing order (from best to worst fit).
Coordinate 1: for each solution the corresponding bff. Here '
counter' comes into play, as it excludes all the lines of the grid
that did not contain a solution.
62
63 The chisqfunc function implements a least squares reduction by
summing the difference of the theoretical flux and the observed
flux, squaring it and then dividing by the error (standard
deviation). Therefore it's a weighted least squares method with the
errors as weight.
64
65 If the pixel in question is one the max, med, min, max_r, min_r,
sled and hist functions are called.

```

```

66     sled: Depending on the flag 'check' it creates a sled for all
        the temperatures or only the unique ones.
67     hist: Creates histograms for the kinetic temperature, number
        density, column density and bff.
68
69     In the Graphs section we import the first non None file of the
        image_list list. This is appointed to the variable "im". It is
        needed later on, for the header.
70     The graphs function is used for graph plotting. Depending on the
        truth value of the "check" input, the colorbar is either in
        logarithmic scale or in linear scale. The "box_scale" variable
        defines the x and y axis length, while vmin and vmax the minimum
        and maximum values of the colorbar.
71
72     For the histograms we cannot just use 'auto' for the bins as it
        does not work properly for logarithmic data. Therefore we turn them
        into non-log data, calculate the bins and turn them back again.
        This is achieved in 'full_hist_arr' and 'bins'. Specifically, in '
        full_hist_arr' we combine the values of all transitions for each
        quantity to get the best possible display.
73
74     For the sleds we use a different color for the best fit. The reason
        the code is written like this is because the grey lines are
        plotted over the initial best fit and it is not visible afterwards.
        Another way of writing it is to reverse the order in which the
        sleds are printed. This also does not work because if the
        restriction of how many sigmas are allowed is lenient enough, some
        sleds from the other transition can happen to reach the transition
        in question and overplot it.
        '''
75
76 execfile('/mnt/disk1/models/fits_handling.py')
77 ###----- Spiral -----###
78 def spiral_cw(A):
79     A = np.array(A)
80     out = []
81     while(A.size):
82         out.append(A[0][::-1]) # first row reversed
83         A = A[1:][::-1].T # cut off first row and rotate
        clockwise
84     return np.concatenate(out)
85
86 def base_spiral(nrow, ncol):
87     return spiral_cw(np.arange(nrow*ncol).reshape(nrow, ncol))[:, -1]
88
89 def to_spiral(A):
90     A = np.array(A)
91     B = np.empty_like(A)
92     B.flat[base_spiral(*A.shape)] = A.flat
93     return B
94
95 def from_spiral(A):
96     A = np.array(A)
97     return A.flat[base_spiral(*A.shape)].reshape(A.shape)
98 ###-----###
99
100 ###----- Histogram -----###

```



```

101 def hist(x,integ_const , beam_filling_factor , frequencies , rdx):
102     best_fit=rdx[0]; chi2=rdx[1]
103     N_lines=len(frequencies)
104     lower=int(3+2*N_lines)
105     T=np.array(x[:,0:1]); n=np.array(x[:,1:2]); N=np.array(x[:,2:3]);
T_ex=np.array(x[:,lower:int(lower+N_lines)]); T_R = np.array(x[:,
int(lower+N_lines):int(lower+2*N_lines)]); TAU=np.array(x[:,int(
lower+2*N_lines):int(lower+3*N_lines)])

106
107     Temp_sol=[T[int(val)][0] for i, val in enumerate(best_fit.T[0]) if
not all(i==np.inf for i in chi2[int(val)])]
108     T_r_sol=[T_R[int(val),:][0] for i, val in enumerate(best_fit.T[0])
if not all(i==np.inf for i in chi2[int(val)])]
109     n_sol=[n[int(val)][0] for i, val in enumerate(best_fit.T[0]) if not
all(i==np.inf for i in chi2[int(val)])]
110     N_sol=[N[int(val)][0] for i, val in enumerate(best_fit.T[0]) if not
all(i==np.inf for i in chi2[int(val)])]
111     bff_sol=[beam_filling_factor[int(best_fit[i][1])] for i, val in
enumerate(best_fit.T[0]) if not all(i==np.inf for i in chi2[int(val
)])]
112     return [Temp_sol, n_sol, N_sol, bff_sol]
113 ##-----##
114
115 ##----- Sled -----##
116 def sled(x,rdx,integ_const , beam_filling_factor , _color_ , frequencies ,
velocities , check):
117     best_fit=rdx[0]; chi2=rdx[1]; flux=rdx[2]; err=rdx[3]
118     N_lines=len(flux)
119     lower=int(3+2*N_lines)
120     T=np.array(x[:,0:1]); n=np.array(x[:,1:2]); N=np.array(x[:,2:3]);
T_ex=np.array(x[:,lower:int(lower+N_lines)]); T_R = np.array(x[:,
int(lower+N_lines):int(lower+2*N_lines)]); TAU=np.array(x[:,int(
lower+2*N_lines):int(lower+3*N_lines)])
121     if check:
122         Tfound=T[best_fit[0][0]]; flux_theoretical=[]; T_kinetic=[];
number_density=[]; column_density=[]
123         for i, val in enumerate(best_fit.T[0]):
124             if all(i==np.inf for i in chi2[int(val)]): continue
125             if i==0:
126                 Tfound=np.append(Tfound,T[int(val)])
127             else:
128                 if T[int(val)] in Tfound: continue
129                 Tfound=np.append(Tfound,T[int(val)])
130                 flux_sol=np.array(T_R[int(val),0:4])*frequencies**3*
integ_const*beam_filling_factor[int(best_fit[i][1])]
131                 flux_theoretical.append(flux_sol); T_kinetic.append(T[int(
val)][0]); number_density.append(n[int(val)]; column_density.
append(N[int(val)])
132             else:
133                 flux_theoretical=[np.array(T_R[int(val),0:4])*frequencies**3*
integ_const*beam_filling_factor[int(best_fit[i][1])] for i, val in
enumerate(best_fit.T[0]) if not all(i==np.inf for i in chi2[int(val
)])]
134                 T_kinetic=[T[int(val)][0] for i, val in enumerate(best_fit.T
[0]) if not all(i==np.inf for i in chi2[int(val)])]

```

```

135     number_density=[n[int(val)][0] for i, val in enumerate(best_fit
136     .T[0]) if not all(i==np.inf for i in chi2[int(val)])]
137
138     column_density=[N[int(val)][0] for i, val in enumerate(best_fit
139     .T[0]) if not all(i==np.inf for i in chi2[int(val)])]
140
141     try:
142         label=r"$T_{kin} = [%s, $" %min(T_kinetic)+ "$%s] $" %max(
143         T_kinetic) + "$K$, " + "$n = [%s, $" %round(min(number_density)) + "
144         $%s] $" %round(max(number_density)) + " $cm^{-3}$, " + "$N = [%s, $"
145         %round(min(column_density)*velocities[0]) + "$%s] $" %round(max(
146         column_density)*velocities[0]) + " $cm^{-2}$"
147     except:
148         label=r"No solution"
149     return [flux_theoretical, flux, err, label]
150
151 ##-----
152 ##----- Weighted least squares, with the error as weight -----##
153 def chisqfunc(flux, theoretical_flux, err):
154     return np.nansum(((flux-theoretical_flux)**2)/(err**2))
155
156 ##-----
157 ##----- Opens the grid and finds the best fit (chi^2) -----##
158
159 def radex_solution(x, flux_obs, err_obs, v_obs, emitting_region_size,
160     beam_filling_factor, n_old, N_old, flux_central, N_central, n_central,
161     pixel, fl_min, first):
162
163     N_lines=int(len(flux_obs))
164     frequencies=np.array([115.27120180, 230.53800000, 345.79598990,
165     461.04076820, 576.26793050, 691.47307630, 806.65180600,
166     921.79970000, 1036.91239300, 1151.98545200])
167     frequencies=frequencies[:N_lines]
168     integ_const=1.02*10**8*emitting_region_size/(206265.)*2
169     c=2.9979*10**5
170     flux=flux_obs*frequencies*10**9/c/v_obs
171     err=err_obs*frequencies*10**9/c/v_obs
172     flux_central *= frequencies[0]*10**9/c/v_obs[0]
173     T_R_obs=fl_min*1e9/v_obs/c/integ_const/frequencies**2
174     sigma=(5.**2)*len([i for i in flux if np.isnan(i)==False])
175
176     if first:
177         if nohup: print('sigma: ', sigma)
178         else: logging.info('sigma: ', sigma)
179
180     chi2=np.ones((x.shape[0], beam_filling_factor.shape[0]))*np.inf
181     counter=0; bff_count=[]; lower=int(3+2*N_lines)
182     T=np.array(x[:,0:1]); n=np.array(x[:,1:2]); N=np.array(x[:,2:3]);
183     T_ex=np.array(x[:,lower:int(lower+N_lines)]); T_R = np.array(x[:,
184     int(lower+N_lines):int(lower+2*N_lines)]); TAU=np.array(x[:,int(
185     lower+2*N_lines):int(lower+3*N_lines)])
186     for i in range(x.shape[0]):
187         if any(tau>=100 or tau<0 for tau in TAU[i]): continue
188         if T_ex[i][0]<5.53: continue
189         if any(dummy1<dummy2 for dummy1, dummy2 in zip(T_R[i],
190         T_R_obs)): continue
191         for f in range(beam_filling_factor.shape[0]):

```

```

176         if first:
177             theoretical_flux=T_R[i,:]*frequencies**3*integ_const*
beam_filling_factor[f]
178         else:
179             if max(n[i][0],n_old)/min(n[i][0],n_old)>3.: continue
180             if n[i][0]>n_central: continue
181             theoretical_flux=T_R[i,:]*frequencies**3*integ_const*
beam_filling_factor[f]
182             if N[i][0]/N_central>(flux[0]+1.*err[0])/flux_central
or N[i][0]/N_central<(flux[0]-1.*err[0])/flux_central: continue
183             if chisqfunc(flux,theoretical_flux,err)>sigma: continue
184             counter+=1
185             bff_count.append(beam_filling_factor[f])
186             chi2[i][f]=chisqfunc(flux,theoretical_flux,err)
187
188             best_fit=np.where(chi2 == np.min(chi2))
189             best_fit_full=np.vstack((np.unravel_index(chi2.argsort(axis=None,
kind='mergesort'),chi2.shape)).T[0:counter]
190             SLED=[]; histogram=[]
191
192             hits=Counter(bff_count)
193             total = sum(hits.itervalues(), 0.0)
194             hits = {k: v for k, v in hits.iteritems()}
195
196
197             ##----- SLEDs and Histograms -----##
198             if pixel in ['red', 'purple', 'darkblue', 'green', 'yellow']:
199                 SLED.append(sled(x,[best_fit_full,chi2,flux,err],integ_const,
beam_filling_factor,pixel,frequencies,v_obs,check=False))
200                 histogram.append(hist(x,integ_const,beam_filling_factor,
frequencies,[best_fit_full,chi2]))
201             ##-----##
202
203             file_index=best_fit[0][0]
204             bff_index=best_fit[1][0]
205
206             T_R=T_R[file_index]
207             T_excit=T_ex[file_index]
208             T_kin=T[file_index][0]
209             num_dens=n[file_index][0]
210             col_dens=N[file_index][0]
211             opt_depth=TAU[file_index]
212             bff=beam_filling_factor[bff_index]
213             if np.min(chi2)==inf:
214                 T_R*=nan; T_excit*=nan; T_kin*=nan; num_dens*=nan; col_dens*=
nan; opt_depth*=nan; bff*=nan
215             return (T_kin,num_dens,col_dens,bff,T_R, T_excit,opt_depth,
histogram,SLED,total,hits)
216         ##-----##
217
218         ##----- Loops over the radex_solution function -----##
219         def loop_radex_solution(filenamees,beam_filling_factor,grid,spiral_check
=True):
220             dictionary_init={'im'+str(dummy): import_file_astro(filename) for
dummy, filename in enumerate(filenamees, start=1) if filename is not
None}

```

```

221     dictionary_v={ 'v'+str(dummy):nan for dummy in range(1,N+1) if 'im'+
str(dummy) not in dictionary_init }
222
223     Fits=dictionary_init.values()[0].copy()
224     Fits.data=dictionary_init.values()[0].copy().data-dictionary_init.
values()[0].copy().data
225
226     dictionary_upd={ 'im'+str(dummy):Fits for dummy in range(1,N+1) if '
im'+str(dummy) not in dictionary_init }
227     dictionary=dict(dictionary_init, **dictionary_upd)
228     dictionary=collections.OrderedDict(sorted(dictionary.items()))
229     dictionary_upd_v={ 'v'+str(i+1):abs(dictionary.values()[i].header[ '
VELRNG1' ]-dictionary.values()[i].header[ 'VELRNG2' ]) for i in
range(N) if 'v'+str(i+1) not in dictionary_v }
230     dictionary_v=dict(dictionary_v, **dictionary_upd_v)
231     v_obs=list(dictionary_v.values())
232
233     if spiral_check:
234         dictionary_data=[from_spiral(dummy2.data) for dummy1, dummy2 in
sorted(dictionary.items())]
235         flux_central=dictionary_data[0][0][0]
236     else:
237         dictionary_data=[dummy2.data for dummy1, dummy2 in sorted(
dictionary.items())]
238         flux_central=dictionary_data[0][int(round(dictionary_data[0].
shape[0]/2.))][int(round(dictionary_data[0].shape[1]/2.))]
239
240     max_pixel=np.argwhere(dictionary_data[0]==np.nanmax(dictionary_data
[0]))
241     min_pixel=np.argwhere(dictionary_data[0]==np.nanmin(dictionary_data
[0]))
242     med_pixel= np.argwhere( np.abs(dictionary_data[0]-np.nanmean(
dictionary_data[0], keepdims=True)) == np.nanmin(np.abs(
dictionary_data[0]-np.nanmean(dictionary_data[0], keepdims=True)))
)
243     fl_min=np.array([dictionary_data[dummy][min_pixel[0][0]][min_pixel
[0][1]] for dummy in range(N)])
244
245     if spiral_check: ratio=np.divide(from_spiral(dictionary_init.values
()[ -1].copy().data),from_spiral(dictionary_init.values()[0].copy().
data))
246     else: ratio=np.divide(dictionary_init.values()[ -1].copy().data ,
dictionary_init.values()[0].copy().data)
247     max_r_pixel=np.argwhere(ratio==np.nanmax(ratio))
248     min_r_pixel=np.argwhere(ratio==np.nanmin(ratio))
249
250     T_k, num_dens, col_dens, bff = [np.zeros((dictionary_data[0].shape
)) for dummy in range(4)]
251     T_ex_list=[np.zeros((dictionary_data[0].shape)) for i in range(N)]
252     TAU_list=[np.zeros((dictionary_data[0].shape)) for i in range(N)]
253
254     histogram={}; SLED={}; hits=Counter({dummy:0. for dummy in factor})
; hits_pix=[]; local_counter=0.
255
256     max_value=int(len(dictionary_data[0].flatten()[np.isnan(
dictionary_data[0].flatten())==False]))

```

```

257     bar_count=0; first_check=0
258     with progressbar.ProgressBar(max_value=max_value) as bar:
259     for i in range(dictionary_data[0].shape[0]):
260         for j in range(dictionary_data[0].shape[1]):
261             flux_obs=[dictionary_data[dummy][i][j] for dummy in range(N)]
262             if np.all([i,j]==max_pixel): pixel='red'
263             elif np.all([i,j]==med_pixel): pixel='purple'
264             elif np.all([i,j]==min_pixel): pixel='darkblue'
265             elif np.all([i,j]==max_r_pixel): pixel='green'
266             elif np.all([i,j]==min_r_pixel): pixel='yellow'
267             else: pixel=nan
268             if any(np.isnan(f_obs)==True for f_obs in flux_obs):
269                 T_k[i][j], num_dens[i][j], col_dens[i][j], bff[i][j] = [nan for
dummy in range(4)]
270                 for dummy_index in range(N):
271                     T_ex_list[dummy_index][i][j]=nan
272                     TAU_list[dummy_index][i][j]=nan
273                 else:
274                     err_obs={'err'+str(var+1):dictionary.values()[var].header["STDEV"
] for var in range(N)}
275                 for dummy in range(N):
276                     if dictionary_data[dummy][i][j]==0: err_obs['err'+str(dummy
+1)]=nan
277                     err_obs=collections.OrderedDict(sorted(err_obs.items()))
278                     if [i,j]==[0,0] or first_check==0:
279                         results=radex_solution(grid,np.array(flux_obs),np.array(
err_obs.values()),np.array(v_obs),(dictionary.values()[0].header['
CDEL1']*3600)**2,np.array(beam_filling_factor),nan,nan,nan,nan,nan
,pixel,fl_min,first=True)
280                         N_central=results[2]
281                         n_central=results[1]
282                     else:
283                         bar_count+=1
284                         results=radex_solution(grid,np.array(flux_obs),np.array(
err_obs.values()),np.array(v_obs),(dictionary.values()[0].header['
CDEL1']*3600)**2,np.array(beam_filling_factor),results[1],results
[2],flux_central,N_central,n_central,pixel,fl_min,first=False)
285                         T_k[i][j]=results[0]; num_dens[i][j]=results[1]; col_dens[i][j]=
results[2]; bff[i][j]=results[3]
286                         for dummy_index in range(N):
287                             T_ex_list[dummy_index][i][j]=results[5][dummy_index]
288                             TAU_list[dummy_index][i][j]=results[6][
dummy_index]
289                         if len(results[7])>0: histogram.update( {pixel : results[7]} )
290                         if len(results[8])>0: SLED.update( {pixel : results[8]} )
291                         local_counter+=results[9]
292                         hits.update(results[10])
293                         if pixel in ['red', 'purple', 'darkblue', 'green', 'yellow']:
294                             hits_pix.append(results[10])
295                         first_check=1
296                         bar.update(bar_count)
297                         histogram=[histogram['red'], histogram['purple'], histogram['darkblue
'], histogram['green'], histogram['yellow']]
298                         SLED=[SLED['red'], SLED['purple'], SLED['darkblue'], SLED['green'],
SLED['yellow']]
299                         if local_counter==0:

```

```

300     print 'No solutions whatsoever'
301     quit()
302     hits={k: round(v / local_counter * 100., 2) for k, v in dict(hits).
iteritems()}
303     hits_pix = set.intersection(*map(set, hits_pix))
304     if spiral_check:
305         T_ex_final=[to_spiral(element) for element in T_ex_list]
306         TAU_final=[to_spiral(element) for element in TAU_list]
307         return (to_spiral(T_k), to_spiral(num_dens), to_spiral(col_dens),
to_spiral(bff), T_ex_final, TAU_final, v_obs, ratio, histogram, SLED, hits
, hits_pix)
308     else:
309         T_ex_final=[element for element in T_ex_list]
310         TAU_final=[element for element in TAU_list]
311         return (T_k, num_dens, col_dens, bff, T_ex_final, TAU_final, v_obs,
ratio, histogram, SLED, hits, hits_pix)
312 ##-----##
313
314 ##----- Input parametres -----##
315 nohup=True
316 if nohup:
317     #galaxy='OQ208'
318     galaxy='4C12.50'
319     #galaxy='IC5063'
320     print galaxy
321 else:
322     galaxy = raw_input('Galaxy name: ')
323     logging.basicConfig(filename=galaxy+'.log', level=logging.INFO)
324     logging.info('galaxy: ', galaxy)
325
326 if nohup:
327     factor=np.hstack(np.arange(1,11,1)*i for i in np.logspace(-4,-1,4))
328     print('bff: ', factor)
329 else:
330     answer=bool(raw_input('Beam filling factor: Single value=input,
logspace=no input '))
331     if answer: factor=[float(raw_input('Beam filling factor: '))]
332     else:
333         low, high, steps=raw_input('Lower limit Upper limit steps: ').
split(' ')
334         factor=np.hstack(np.linspace(1,9,9)*i for i in np.logspace(
float(low), float(high), float(steps)))
335         logging.info('bff: %s' %factor)
336
337 name = galaxy+'_maps_bff_'+str(factor[0])
338 try:
339     os.mkdir(name)
340 except:
341     name=name+'_'+datetime.datetime.fromtimestamp(time.time()).strftime
('%Y-%m-%d_%H:%M:%S')
342     os.mkdir(name)
343 os.chdir(name)
344
345 if nohup: print('Directory name: '+name)
346 else: logging.info('Directory name: '+name)
347

```

```

348 grid_name='/mnt/disk1/models/GRID_updated_IC_large.rdx'
349 if grid_name.endswith('.npz'):
350     grid=np.load(grid_name)['arr_0']
351 else:
352     grid=np.loadtxt(grid_name, delimiter=',')
353
354 image_list=['/mnt/disk1/models/IC_Maps/CO10_20_collapsed_m200_200_stdev
', '/mnt/disk1/models/IC_Maps/CO21_conv_20_collapsed_m200_200_stdev'
', '/mnt/disk1/models/IC_Maps/CO32_conv_20_collapsed_m200_200_stdev' ,
', '/mnt/disk1/models/IC_Maps/CO43_conv_20_collapsed_m200_200_stdev']
355
356 if nohup:
357     print('grid_name: ', grid_name)
358     print('image_list: ', image_list)
359 else:
360     logging.info('grid_name: ', grid_name)
361     logging.info('image_list: ', image_list)
362
363 N=len(image_list)
364 im=import_file_astro(image_list [[ image_list.index(Index) for Index in
image_list if Index!=None][0]])
365 res=loop_radex_solution(image_list, factor, grid)
366 np.savez('results', *[i for i in res])
367 ##-----##
368
369 ##----- Graphs -----##
370 def graphs(arr, sub, fig, _str, check):
371     cm=plt.cm.jet
372     P2A=abs(im.header['CDELTA1'])*3600
373     box_size=round(100*P2A/2.-0.5)
374     if check: image=sub.imshow(arr, origin='low', cmap=cm, norm=colors.
LogNorm(), vmin=np.nanmin(arr), vmax=np.nanmax(arr), extent=[-im.
header['NAXIS1']*P2A/2., im.header['NAXIS1']*P2A/2., -im.header['
NAXIS2']*P2A/2., im.header['NAXIS2']*P2A/2.])
375     else: image=sub.imshow(arr, origin='low', cmap=cm, vmin=np.nanmin(arr)
, vmax=np.nanmax(arr), extent=[-im.header['NAXIS1']*P2A/2., im.header[
'NAXIS1']*P2A/2., -im.header['NAXIS2']*P2A/2., im.header['NAXIS2']*
P2A/2.])
376     sub.axis([-box_size, box_size, -box_size, box_size])
377     divider = make_axes_locatable(sub)
378     fig.colorbar(image, cax=divider.append_axes("right", size="5%", pad
=0.05), format='%.1E')
379     sub.set_title(_str)
380     plt.tight_layout(h_pad=1)
381
382 plt.ioff()
383 ext='.eps'
384 dpi=300
385
386 ##----- Tk, n_dens, c_dens -----##
387 fig1, (a1, a2, a3) = plt.subplots(ncols=3, figsize=(15,15))
388 im1=graphs(res[0], a1, fig1, r'Kinetic temperature (K)', False)
389 a1.plot(0,0, '+', mew=1, ms=30, c='k')
390 im2=graphs(res[1], a2, fig1, r'H$_{2}$ Number density (cm$^{-3}$)', True)
391 a2.plot(0,0, '+', mew=1, ms=30, c='k')
392 im3=graphs(res[2], a3, fig1, r'CO Column density (cm$^{-2}$)', True)

```

```

393 a3.plot(0,0,'+',mew=1, ms=30, c='k')
394 plt.savefig('Ndens-temp-cdens-bff'+str(factor[0])+ext, bbox_inches='
    tight', dpi=dpi)
395 ##-----##
396
397 ##----- Beam filling factor -----##
398 fig2, (a1) = plt.subplots(ncols=1, figsize=(5,5))
399 im1=graphs(res[3], a1, fig2, r'$bff$', False)
400 a1.plot(0,0,'+',mew=1, ms=30, c='k')
401 plt.savefig('bff-map-bff'+str(factor[0])+ext, bbox_inches='tight', dpi=
    dpi)
402 ##-----##
403
404 ##----- Excitation Temperature -----##
405 subplot_obj3=plt.subplots(ncols=N, figsize=(15,15))
406 subplot_list3=sorted(list({'im'+str(dummy+1) for dummy in range(N)}))
407 for i in range(N):
408     if np.isnan(res[6][i])==False: subplot_list3[i]=graphs(res[4][i],
        subplot_obj3[1][i], subplot_obj3[0], r'CO'+str(i+1)+str(i)+'
        Excitation temperature (K)', False)
409     else: subplot_list3[i]=graphs(np.ones(res[2].shape), subplot_obj3
        [1][i], subplot_obj3[0], r'NaN', True)
410     subplot_obj3[1][i].plot(0,0,'+',mew=1, ms=30, c='k')
411 plt.savefig('T_excit-bff'+str(factor[0])+ext, bbox_inches='tight', dpi=
    dpi)
412 ##-----##
413
414 ##----- Optical Depth -----##
415 subplot_obj4=plt.subplots(ncols=N, figsize=(15,15))
416 subplot_list4=sorted(list({'im'+str(dummy+1) for dummy in range(N)}))
417 for i in range(N):
418     if np.isnan(res[6][i])==False: subplot_list4[i]=graphs(res[5][i],
        subplot_obj4[1][i], subplot_obj4[0], r'Optical depth ('+str(i+1)+str(
        i)+')', True)
419     else: subplot_list4[i]=graphs(np.ones(res[2].shape), subplot_obj4
        [1][i], subplot_obj4[0], r'NaN', True)
420     subplot_obj4[1][i].plot(0,0,'+',mew=1, ms=30, c='k')
421 plt.savefig('Optical-depths-bff'+str(factor[0])+ext, bbox_inches='tight'
    , dpi=dpi)
422 ##-----##
423
424 ##----- Pressure -----##
425 fig5, (a1) = plt.subplots(ncols=1, figsize=(5,5))
426 im1=graphs(res[0]*res[1], a1, fig5, r'$nT$', True)
427 a1.plot(0,0,'+',mew=1, ms=30, c='k')
428 plt.savefig('Pressure-bff'+str(factor[0])+ext, bbox_inches='tight', dpi=
    dpi)
429 ##-----##
430
431 ##----- Column Densities -----##
432 subplot_obj6=plt.subplots(ncols=N, figsize=(15,15))
433 subplot_list6=sorted(list({'im'+str(dummy+1) for dummy in range(N)}))
434 for i in range(N):
435     if np.isnan(res[6][i])==False: subplot_list6[i]=graphs(res[2]*res
        [6][i], subplot_obj6[1][i], subplot_obj6[0], r'CO Column density ('+
        str(i+1)+str(i)+' (cm$^{-2}$)', True)

```



```

436     else: subplot_list6[i]=graphs(np.ones(res[2].shape),subplot_obj6
437     [1][i],subplot_obj6[0],r'NaN',True)
437     subplot_obj6[1][i].plot(0,0,'+',mew=1,ms=30,c='k')
438 plt.savefig('Col_densities'+str(factor[0])+ext,bbox_inches='tight',dpi=
439 dpi)
439 ##-----##
440
441 ##----- Ratio -----##
442 fig7,(a1)=plt.subplots(ncols=1,figsize=(5,5))
443 im1=graphs(res[7],a1,fig7,r'Ratio',False)
444 a1.plot(0,0,'+',mew=1,ms=30,c='k')
445 plt.savefig('Ratio'+str(factor[0])+ext,bbox_inches='tight',dpi=dpi)
446 ##-----##
447
448 ##----- Histograms -----##
449 col=np.array(['red','purple','darkblue','green','yellow'])
450 lab=['max','med','min','max ratio','min ratio']
451 flux_str=['Kinetic temperature','Number density','Column density','Beam
452           filling factor']
452 J=list(np.arange(1,N+1,1))
453
454 fig8=plt.figure()
455 with PdfPages('Histograms_overlap_single_page_combined.pdf') as pdf:
456     for i in range(len(flux_str)):
457         ax=fig8.add_subplot(2,2,i+1)
458         full_hist_arr=np.ndarray.flatten(np.hstack(res[8][k][0][i] for
459         k in range(len(lab))))
460         bins=10*np.histogram(np.log10(full_hist_arr),bins='auto')[1]
461         for j in range(len(lab)):
462             hist_arr=np.ndarray.flatten(np.array(res[8][j][0][i]))
463             ax.hist(hist_arr,color=col[j],bins=bins,label=lab[j],alpha
464             =0.5)
465         ax.set_xscale('log');ax.set_title(str(flux_str[i]))
466         ax.ticklabel_format(axis='y',style='sci',scilimits=(0,0))
467         if i==0:ax.legend(loc=2,frameon=False,prop={'size':8})
468     pdf.savefig();plt.close()
469 ##-----##
470 ##----- SLEDs -----##
471 if '4C' in galaxy.upper():
472     Mpc=542. #4C12.50
473 elif 'OQ' in galaxy.upper():
474     Mpc=342. #OQ208
475 elif 'IC' in galaxy.upper():
476     Mpc=48. #IC5063
477 RR=4*math.pi*(Mpc*10**6*3.086*10**16)**2
478 L0=3.828*10**26
479 Jy=10**-26
480 Sol=Jy*RR/L0
481 [max_th_flux,max_FLUX,max_ERR,max_LABEL]=[dummy for dummy in res
482 [9][0][0]]
483 [med_th_flux,med_FLUX,med_ERR,med_LABEL]=[dummy for dummy in res
484 [9][1][0]]
485 [min_th_flux,min_FLUX,min_ERR,min_LABEL]=[dummy for dummy in res
486 [9][2][0]]

```

```

484 [max_r_th_flux, max_r_FLUX, max_r_ERR, max_r_LABEL] = [dummy for dummy
      in res[9][3][0]]
485 [min_r_th_flux, min_r_FLUX, min_r_ERR, min_r_LABEL] = [dummy for dummy
      in res[9][4][0]]
486
487 with PdfPages('SLEDs.pdf') as pdf:
488     fig9, ax = plt.subplots()
489     for i in range(len(max_th_flux)):
490         ax.plot(J, max_th_flux[i]*Sol, '—', c='lightgrey')
491     for i in range(len(med_th_flux)):
492         ax.plot(J, med_th_flux[i]*Sol, '—', c='lightgrey')
493     for i in range(len(min_th_flux)):
494         ax.plot(J, min_th_flux[i]*Sol, '—', c='lightgrey')
495     for i in range(len(max_r_th_flux)):
496         ax.plot(J, max_r_th_flux[i]*Sol, '—', c='lightgrey')
497     for i in range(len(min_r_th_flux)):
498         ax.plot(J, min_r_th_flux[i]*Sol, '—', c='lightgrey')
499     try: ax.plot(J, max_th_flux[0]*Sol, '—', c=col[0], label=max_LABEL)
500     except: pass
501     try: ax.plot(J, med_th_flux[0]*Sol, '—', c=col[1], label=med_LABEL)
502     except: pass
503     try: ax.plot(J, min_th_flux[0]*Sol, '—', c=col[2], label=min_LABEL)
504     except: pass
505     try: ax.plot(J, max_r_th_flux[0]*Sol, '—', c=col[3], label=
max_r_LABEL)
506     except: pass
507     try: ax.plot(J, min_r_th_flux[0]*Sol, '—', c=col[4], label=
min_r_LABEL)
508     except: pass
509
510     plt.errorbar(J, max_FLUX*Sol, max_ERR*Sol, label=r"$Maximum\ flux\
pixel$", capsize=3, fmt='o', c=col[0])
511     plt.errorbar(J, med_FLUX*Sol, med_ERR*Sol, label=r"$Median\ flux\
pixel$", capsize=3, fmt='o', c=col[1])
512     plt.errorbar(J, min_FLUX*Sol, min_ERR*Sol, label=r"$Minimum\ flux\
pixel$", capsize=3, fmt='o', c=col[2])
513     plt.errorbar(J, max_r_FLUX*Sol, max_r_ERR*Sol, label=r"$Maximum\ ratio\
\ pixel$", capsize=3, fmt='o', c=col[3])
514     plt.errorbar(J, min_r_FLUX*Sol, min_r_ERR*Sol, label=r"$Minimum\ ratio\
\ pixel$", capsize=3, fmt='o', c=col[4])
515
516     plt.xlabel(r'$J_{u}$'); plt.ylabel(r'$\log(L/L_{\odot})$'); plt.title(
r"$CO SLED$")
517     plt.yscale('log')
518     plt.xlim(0.9, 4.1)
519     plt.legend(bbox_to_anchor=(0.75, 0.99), loc=1, borderaxespad=0.,
labelspace=1, frameon=False, prop={'size': 8})
520     pdf.savefig(bbox_inches='tight'); plt.close()
521 ###-----###
522
523 ###----- Beam filling factor % -----###
524 dic_bff = { dummy: res[10][dummy] for dummy in list(res[11]) }
525 fig10=plt.figure()
526 ax=fig10.gca()
527 ax.bar(res[10].keys(), res[10].values(), width = 100.*factor[0], color=
'g', alpha=0.5)

```

```
528 ax.bar(dic_bff.keys(), dic_bff.values(), width = 100.*factor[0] , color=  
    'k')  
529 ax.set_xlim(min([i for i, j in res[10].iteritems() if j>0]),max([i for  
    i, j in res[10].iteritems() if j>0]))  
530 ax.set_title('% of beam filling factors')  
531 ax.set_xscale('log')  
532 plt.savefig('Bff-percentage'+str(factor[0])+ext, bbox_inches='tight', dpi  
    =dpi)  
533 ##-----##  
534 plt.close('all')  
535 os.chdir('..')  
536 ##-----##
```